

AD-A097 899

AEROSPACE CORP EL SEGUNDO CA ELECTRONICS RESEARCH LAB F/8 20/5
PROGRESS TOWARD A MONOLITHICALLY INTEGRATED COHERENT DIODE LASE--ETC(U)
FEB 81 G A EVANS, E M GARMIRE, H M STOLL F04701-80-C-0081

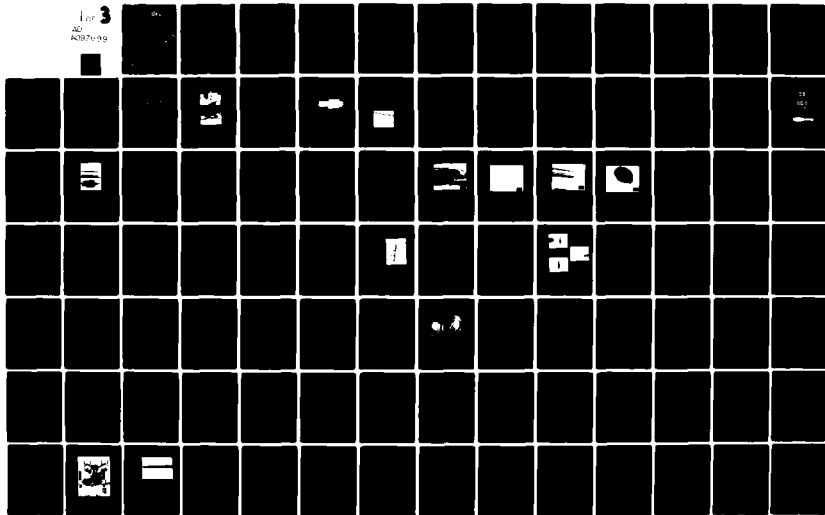
UNCLASSIFIED

TR-0081(6930-04)-2

SD-TR-81-7

NL

For 3
AD
A097899



LEVEL II

12

AD A007099

Progress Toward a Monolithically Integrated Coherent Diode Laser Array

G. A. EVANS, E. M. GARMIRE, H. M. STOLL, J. A. OSMER,
W. E. SOADY, A. B. LEE, and M. P. ZIEGLER
Electronics Research Laboratory
Laboratory Operations
The Aerospace Corporation
El Segundo, Calif. 90245

20 February 1981

Interim Report

APPROVED FOR PUBLIC RELEASE;
DISTRIBUTION UNLIMITED

Prepared for
SPACE DIVISION
AIR FORCE SYSTEMS COMMAND
Los Angeles Air Force Station
P.O. Box 92960, Worldway Postal Center
Los Angeles, Calif. 90009

DTIC
ELECTRONIC
APR 17 1981
C

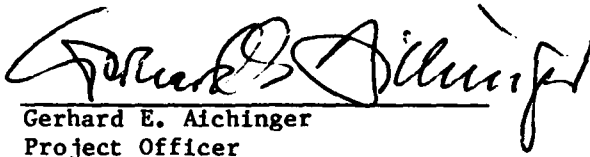
DTIC FILE COPY

81 4 17 021

This interim report was submitted by The Aerospace Corporation, El Segundo, CA 90245, under Contract No. F04701-80-C-0081 with the Space Division, Contracts Management Office, P.O. Box 92960, Worldway Postal Center, Los Angeles, CA 90009. It was reviewed and approved for The Aerospace Corporation by M. T. Weiss, Acting Director, Electronics Research Laboratory. Gerhard E. Aichinger was the project officer for Mission-Oriented Investigation and Experimentation (MOIE) Programs.

This report has been reviewed by the Public Affairs Office (PAS) and is releasable to the National Technical Information Service (NTIS). At NTIS, it will be available to the general public, including foreign nations.

This technical report has been reviewed and is approved for publication. Publication of this report does not constitute Air Force approval of the report's findings or conclusions. It is published only for the exchange and stimulation of ideas.


Gerhard E. Aichinger
Project Officer

FOR THE COMMANDER


Evan R. Brossman, Chief
Contracts Management Office

UNCLASSIFIED

SECURITY CLASSIFICATION OF THIS PAGE (When Data Entered)

REPORT DOCUMENTATION PAGE		READ INSTRUCTIONS BEFORE COMPLETING FORM
1. REPORT NUMBER SD-TR-81-7	2. GOVT ACCESSION NO. AD-A097899	3. RECIPIENT'S CATALOG NUMBER
4. TITLE (and Subtitle) PROGRESS TOWARD A MONOLITHICALLY INTEGRATED COHERENT DIODE LASER ARRAY		5. TYPE OF REPORT & PERIOD COVERED Interim
7. AUTHOR(s) Gary A. Evans, Elsa M. Garmire, Harold M. Stoll, Judith A. Osmer, William E. Soady, Allen B. Lee, and Myron P. Ziegler		6. PERFORMING ORG. REPORT NUMBER TR-0081(6938-04)-2
9. PERFORMING ORGANIZATION NAME AND ADDRESS The Aerospace Corp. El Segundo, Calif. 90245		8. CONTRACT OR GRANT NUMBER(s) F04701-80-C-0081
11. CONTROLLING OFFICE NAME AND ADDRESS Space Division Air Force Systems Command Los Angeles, Calif. 90009		10. PROGRAM ELEMENT, PROJECT, TASK AREA & WORK UNIT NUMBERS
14. MONITORING AGENCY NAME & ADDRESS (if different from Controlling Office)		12. REPORT DATE 20 February 1981
		13. NUMBER OF PAGES 204
		15. SECURITY CLASS. (of this report) Unclassified
		15a. DECLASSIFICATION/DOWNGRADING SCHEDULE
16. DISTRIBUTION STATEMENT (of this Report) Approved for public release; distribution unlimited		
17. DISTRIBUTION STATEMENT (of the abstract entered in Block 20, if different from Report)		
18. SUPPLEMENTARY NOTES		
19. KEY WORDS (Continue on reverse side if necessary and identify by block number) GaAlAs DBR lasers beam expanders device fabrication photoresist distributed beam deflectors material characterization monolithic laser array liquid phase epitaxy grating fabrication semiconductor lasers coupled lasers		
20. ABSTRACT (Continue on reverse side if necessary and identify by block number) Progress toward the design and fabrication of a GaAlAs semiconductor laser array capable of high average power levels (0.1 to 1.0 watt) and low (1 millirad) beam divergence is reported. A large optical cavity (LOC) configuration is grown by liquid phase epitaxy. The LOC structure is characterized by photoluminescence scans, ion microprobe mass analysis (IMMA), and optical waveguiding measurements. Fabry-Perot, active-passive, and DBR lasers are fabricated using chemical and ion beam etching. Gratings formed using holographic and ion beam		

DD FORM 1473
(IF ACQUISITION)UNCLASSIFIED
SECURITY CLASSIFICATION OF THIS PAGE (When Data Entered)

UNCLASSIFIED

SECURITY CLASSIFICATION OF THIS PAGE(When Data Entered)

19. KEY WORDS (Continued)

20. ABSTRACT (Continued)

etching techniques provide third order feedback for the DBR lasers, and are also used as distributed beam deflectors (DBDs) and output couplers. Comparisons of the results of experiments performed on DBR lasers, DBDs, and coupled lasers are made with theoretical models. Details of the material growth, material characterization, device fabrication, experiments, and theoretical models are presented in this report.

Accession For	
NTIS GRA&I	<input checked="checked" type="checkbox"/>
DTIC TAB	<input type="checkbox"/>
Unannounced	<input type="checkbox"/>
Justification	
By	
Distribution/	
Availability Codes	
Dist	Avail and/or Special
A	

UNCLASSIFIED

SECURITY CLASSIFICATION OF THIS PAGE(When Data Entered)

CONTENTS

1.	INTRODUCTION.....	1-1
2.	SUPPORTING MATERIALS TECHNOLOGY.....	2-1
2.1	Liquid Phase Epitaxy System.....	2-1
2.2	Metal Organic Chemical Vapor Deposition System.....	2-25
3.	MATERIAL CHARACTERIZATION.....	3-1
3.1	Layer Thickness and Composition.....	3-1
3.2	Waveguide Evaluation.....	3-4
3.3	Photoluminescence Measurements.....	3-7
3.4	Fabrication of Broad-Area Fabry-Perot Lasers.....	3-7
4.	FABRICATION TECHNIQUES AND EXPERIMENTAL RESULTS.....	4-1
4.1	DBR Lasers.....	4-1
4.2	Grating Fabrication By Holographic Exposure.....	4-27
4.3	Locking of Laser Stripe Arrays.....	4-35
4.4	Beam Deflection and Expansion.....	4-44
5.	CONCLUSIONS AND SUMMARY.....	5-1
APPENDIXES		
A.	LPE CRYSTAL GROWTH PROCEDURE.....	A-1
B.	OPTIMALLY COUPLED GaAs DBR LASERS.....	B-1
C.	DBR AND ACTIVE-PASSIVE LASER FABRICATION PROCEDURE.....	C-1
D.	ELECTROCHEMICAL DEPOSITION OF OHMIC CONTACTS FOR DIODE LASERS.....	D-1
E.	COUPLED LASER THEORY.....	E-1
F.	DBR: A MULTIFUNCTION INTEGRATED OPTICAL DEVICE.....	F-1

FIGURES

1-1.	High-Brightness GaAs Laser Source.....	1-1
1-2.	Comparison of Single-Stripe Geometry with Proposed Laser Array.....	1-3
2-1.	LPE Experimental Setup.....	2-2
2-2.	Photographs of LPE Apparatus.....	2-3
2-3.	Temperature Profile for Furnace Used in LPE.....	2-4
2-4.	Graphite Boat for LPE of DH Lasers.....	2-5
2-5.	DH Laser Structure.....	2-6
2-6.	Epilayer Structure, Integrating Laser, and Passive Waveguide on Same Substrate.....	2-8
2-7.	ALOC Laser Layer Structure.....	2-10
2-8.	DH Laser.....	2-11
2-9.	Six-Well Graphite Boat for LPE Growth of ALOC Laser.....	2-13
2-10.	Asymmetric LOC DH Laser.....	2-15
2-11.	Angle Lapped Section of Sample H3 with Epilayer Variation Shown.....	2-21
2-12.	Surface of Sample H3 with Surface Roughness Shown.....	2-22
2-13.	Angle Lapped Section of Sample LDL-102.....	2-23
2-14.	Surface of Sample LDL-102.....	2-24
2-15.	Block Diagram of MOCVD System with Associated Safety System.....	2-27
2-16.	Gas-Handling System for MOCVD.....	2-29
3-1.	SEM Photograph of Cleaved Edge of Sample H5.....	3-2
3-2.	IMMA Scan for Sample H5.....	3-3
3-3.	Passive Waveguiding.....	3-5

FIGURES (Continued)

3-4.	Passive Waveguide Structure Including GaAs Buffer Layer to Ensure Homogeneity.....	3-6
3-5.	Experimental Apparatus for Photoluminescence Measurements.....	3-8
3-6.	Photoluminescence Map of Sample LDL 186.....	3-9
3-7.	Photoluminescence Scan.....	3-10
3-8.	Flow Chart for Characterizing Material.....	3-11
4-1.	Cross Section Through Asymmetric LOC DBR Laser.....	4-2
4-2.	Sample Before Processing.....	4-3
4-3.	Sample After Processing, Ready To Be Cleaved Into Individual DBR Lasers.....	4-5
4-4.	DBR Laser.....	4-6
4-5.	Experimental Setup for Laser Spectrum Measurements.....	4-7
4-6.	Spectrum of Typical DBR Laser.....	4-9
4-7.	Spectrum of FP Laser.....	4-10
4-8.	Spectrum of DBR Laser That Supports Two Waveguide Modes and Has Two Oscillator Frequencies.....	4-11
4-9.	Two-Mode DBR Laser.....	4-12
4-10.	ω - β Diagram of Three Scattering Processes.....	4-13
4-11.	Oscillation Wavelengths of DBR Laser with Two Waveguide Modes.....	4-14
4-12.	DBR Laser Spectra.....	4-15
4-13.	Light-Current Characteristics for Diode G9.....	4-17
4-14.	Near-Field Profiles for DBR Laser with Diode G9 at Threshold.....	4-18
4-15.	In-Place Beam Width Versus Distance From Exit Face.....	4-19

FIGURES (Continued)

4-16.	Geometry for In-Plane Divergence of DBR Laser.....	4-21
4-17.	Near-Field Profiles for DBR Laser with Diode G5.....	4-22
4-18.	Third Harmonic Calculation for Square and Triangular Shaped Grating Teeth.....	4-25
4-19.	Laboratory Setup for Exposure of Three Gratings for High-Brightness Laser.....	4-28
4-20.	Cross Section through Ion-Milled DBR Reflector.....	4-29
4-21.	Three Primary Devices on Common Substrate.....	4-33
4-22.	Fabrication of Holographic Gratings.....	4-34
4-23.	Multiple-Grating Fabrication.....	4-36
4-24.	Laser Stripe Array.....	4-37
4-25.	Spectra for Optically Coupled Lasers.....	4-39
4-26.	Near Field Intensity Profiles for Laser Stripe Array.....	4-40
4-27.	Spectra for Locked Lasers.....	4-41
4-28.	Spectra for Unlocked Coupled Lasers.....	4-43
4-29.	DBD.....	4-45
4-30.	Perspective View of Bragg-Effect Polarizer-Analyzer.....	4-49
4-31.	Semilogarithmic Plot of Near-Field Bragg Scattered Beam Intensity Profile of 90-deg Deflector.....	4-50
4-32.	Plots of Throughput Power P_{Out} and Bragg-Scattered Power P_{TMS} as Functions of Input-Beam Polarization Angle θ	4-53
4-33.	Geometry for 45-deg Beam Expander along with Photographs of IR Television Monitor of Near-Field Image of Guide Beam.....	4-54
4-34.	Output Grating Coupler Used to Measure Waveguide Propagation Constant β	4-55

TABLES

2-1.	Experimental Results for Double Heterostructure Lasers.....	2-8
2-2.	ALOC Laser.....	2-10
2-3.	Layer Structure of Wafers.....	2-16
2-4.	Layer Structure for ALOC Wafers.....	2-17
2-5.	DBR Structure E-Series.....	2-18
2-6.	DBR Structure H-Series.....	2-20
2-7.	DBR Structure LDL Series.....	2-26
2-8.	Comparison of Capabilities of MOCVD and LPE Systems.....	2-26
2-9.	Comparison of Characteristics of Growth by MOCVD and LPE Systems.....	2-30
4-1.	Data Used to Determine Coupling Coefficient of Gratings in DBR Lasers.....	4-24

1. INTRODUCTION

The progress achieved in the design and fabrication of a GaAlAs semiconductor laser capable of high average power levels (0.1 to 1.0 W) and low (~ 1 mrad) beam divergence is reported. The program began in June 1977 with a three-month design phase. The design included (1) the development of a laser array concept, (2) an analysis of laser injection locking, (3) a thermal analysis of the suggested array, (4) the development of an integrated optical beam combining network, and (5) the development of an epitaxial structure design.

The results of the initial analyses phase suggested the use of several relatively low-powered GaAs lasers coherently locked together in an array to obtain the desired optical output, and the use of waveguide corrugations to perform optical beam forming. A detailed description of the design study is included in the first year final report.¹ The design concept is illustrated in Fig. 1-1. The lasing cavity is defined by the two distributed Bragg reflectors (DBR) at right angles to each other. The distributed Bragg deflector (DBD) cascade aids in locking the laser array and expands the beam in the vertical direction. The distributed output coupler provides beam expansion in the horizontal direction, and the resultant laser output aperture has an area of several millimeters compared to a few microns for conventional Fabry-Perot semiconductor lasers (Fig. 1-2). It is the large increase in output aperture of the high-brightness laser that will result in low beam divergence.

The high-brightness laser project has been an ambitious undertaking. Multilayer GaAlAs material had to be grown to micron and submicron dimensions over centimeter square areas, evaluated, and fabricated into complex devices.

The high-brightness laser shown in Figs. 1-1 and 1-2 is actually many devices integrated onto a single crystal: DBR lasers, a DBD cascade, and an

¹H.M. Stoll, High Brightness GaAs Laser Source, Contract No. 77G-101820-000, The Aerospace Corporation (30 June 1978).

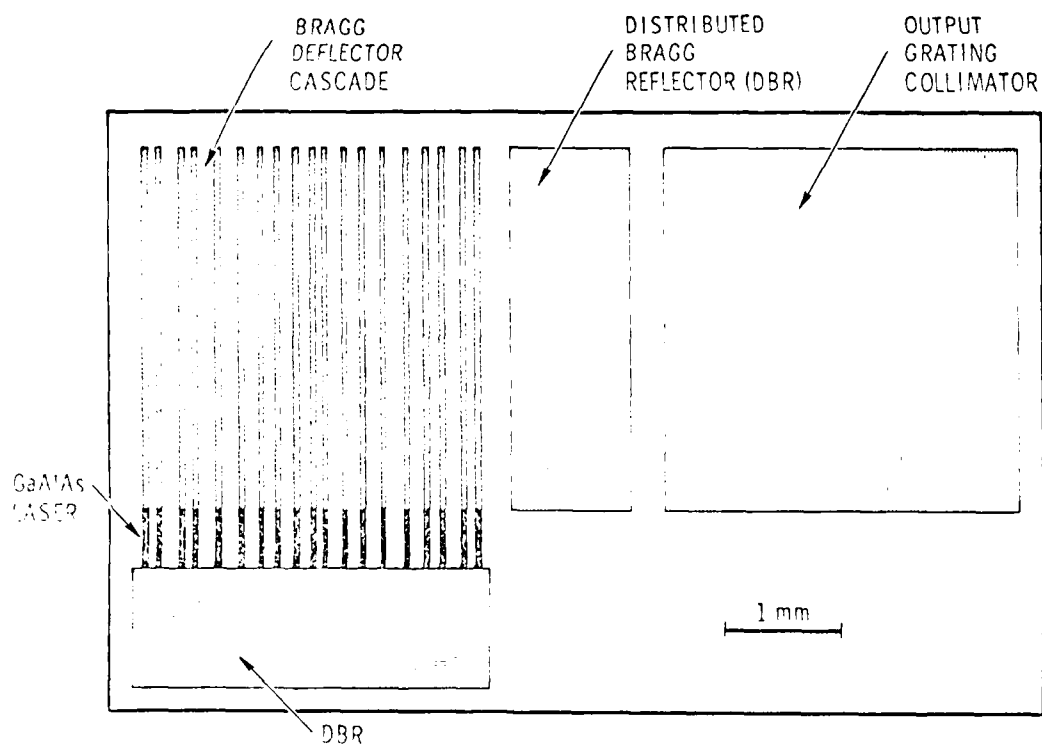


Fig. 1-1. High-Brightness GaAs Laser Source

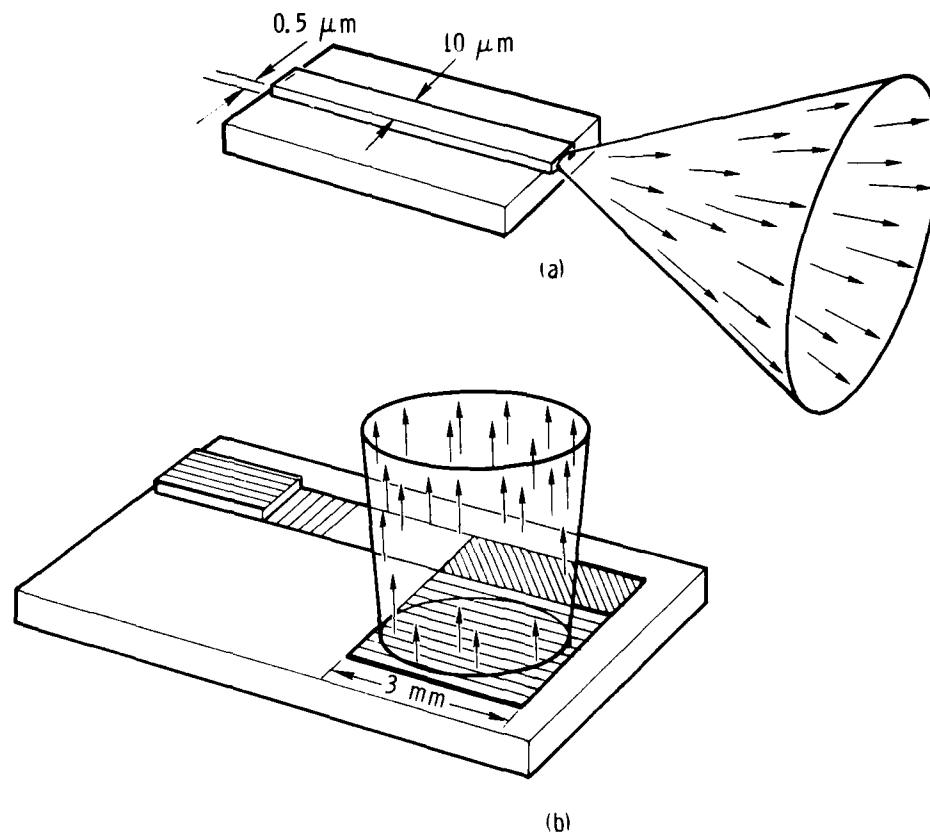


Fig. 1-2. Comparison of Single-Stripe Geometry with Proposed Laser Array.
 (a) Single-stripe geometry laser; beam power = 0.01 W, maximum beam divergence = 1.22 rad. (b) High-spectral radiance laser array; beam power = 1 W, maximum beam divergence = 10^{-3} rad.

output coupler. At Aerospace, we have succeeded in fabricating the individual components. The fabrication techniques and experimental results for the individual devices are discussed in Section 4, as are some results on coupling of stripe geometry lasers. We have not, however, advanced to the point of integrating the components together.

It is our belief that the successful fabrication of a high-brightness laser will profoundly impact optical systems of the future. For this reason, Aerospace is investing corporate funds to support the basic research in the materials growth area required for sustained progress. In parallel with the materials effort, further refining and optimization of the fabrication techniques required to produce the key elements of the high-brightness laser is under way.

2. SUPPORTING MATERIALS TECHNOLOGY

2.1 LIQUID PHASE EPITAXY SYSTEM

The Aerospace liquid phase epitaxy (LPE) system is shown schematically in Fig. 2-1. Photographs of the system are shown in Fig. 2-2. The important features are a temperature-controlled furnace, a high-purity gas-flow system, and a graphite boat and slider.

The furnace is a three-zone Thermco minibrute with a Eurotherm programmer having a quoted stability of $\pm 0.25^\circ\text{C}$. In fact, we measured a temperature stability of $\pm 0.1^\circ\text{C}$ over typical growth times. After careful adjustment, we obtained the temperature profile shown in Fig. 2-3. The temperature was the same within 0.33°C over the full 9 in. of the boat and slider. The programmer dropped the temperature at rates typically $1^\circ\text{C}/\text{min}$ but was capable of rates as slow as $0.2^\circ\text{C}/\text{min}$.

A high-purity H_2 stream at a rate of $10 \text{ cm}^3/\text{min}$ (5 standard ft^3/hr) was produced from commercial hydrogen by diffusing through a palladium hydrogen purifier, resulting in ~ 0.1 ppm impurities. The gas flow system also included N_2 flushing capabilities, and dust, oil, and preliminary oxygen-removing filters. Figure 2-4 is a photograph of the graphite boat used for DH laser growth. This is machined out of high-density POCO graphite (DP-7) and placed in the center of the furnace. An unusual feature of this particular boat is evident, i.e., the two sapphire plates used as wiper blades to remove melt. As part of this contract, new and more sophisticated growth techniques were developed. The growth procedure used now will be described in detail in Appendix A.

The typical double heterostructure laser structure is shown in Fig. 2-5, including an active GaAs layer of thickness t , surrounded by $\text{Ga}_{1-x}\text{Al}_x\text{As}$ several microns thick with an AlAs concentration of $x = 0.47$. The structure also includes a cap of GaAs, which occurred as a consequence of melt remaining on the surface after growth and causing GaAs deposition as the sample cooled. A SEM photograph of a cleaved and stained cross section of a typical double

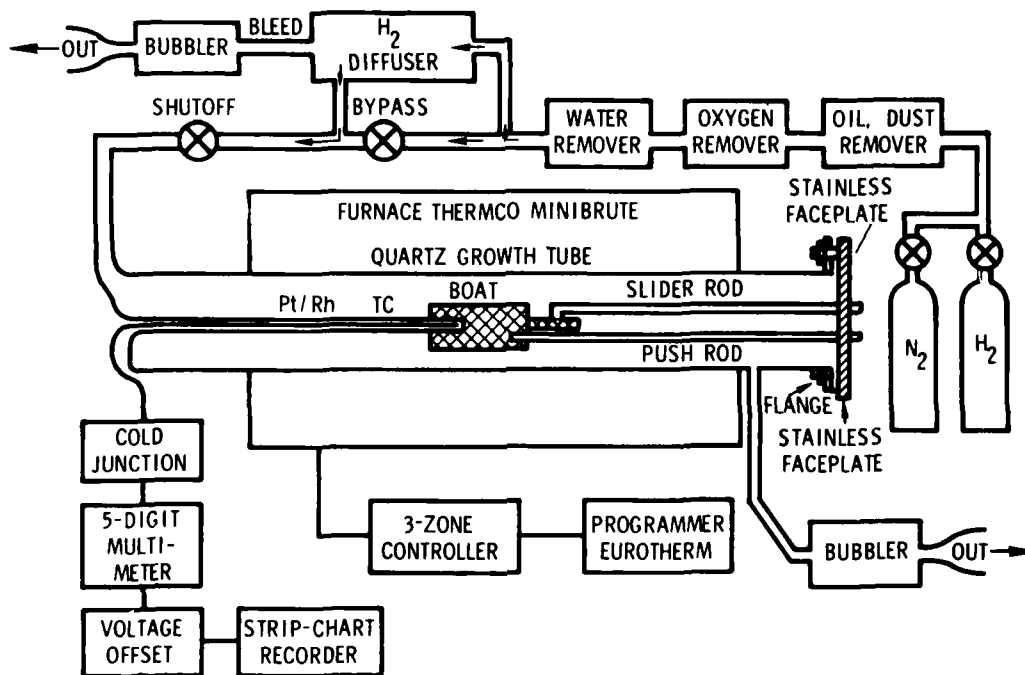


Fig. 2-1. LPE Experimental Setup

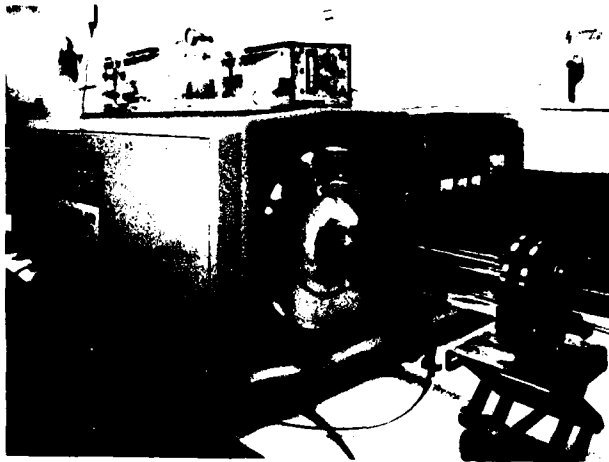


Fig. 2-2. Photographs of LPE Apparatus

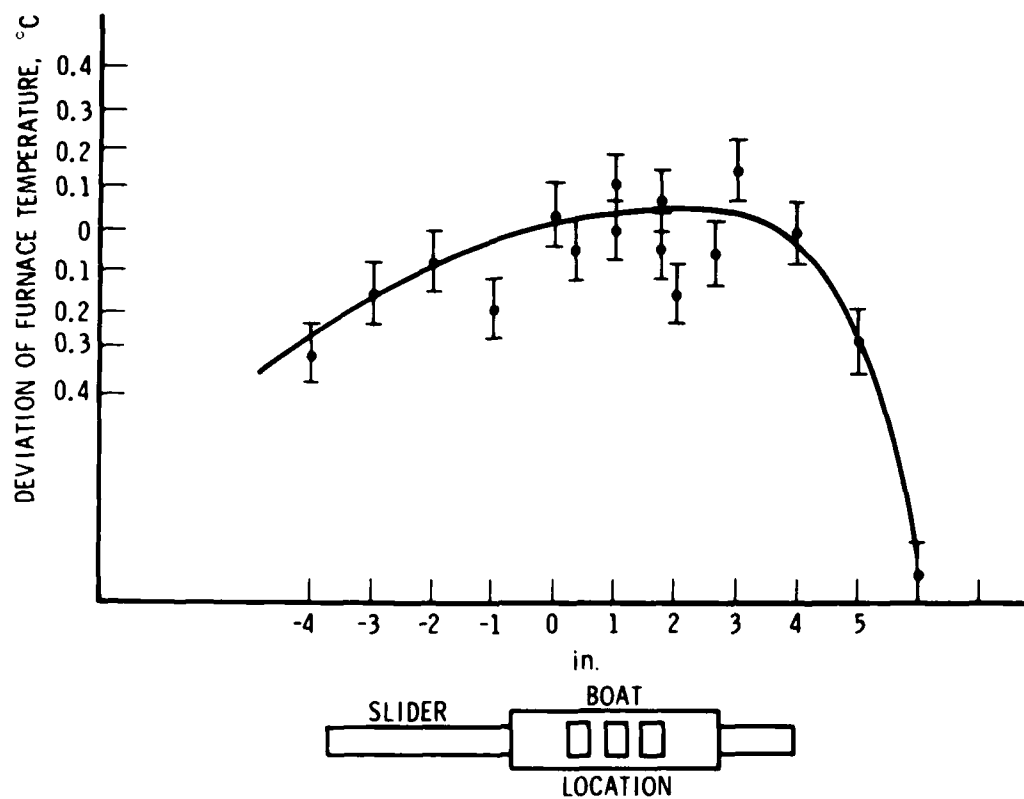
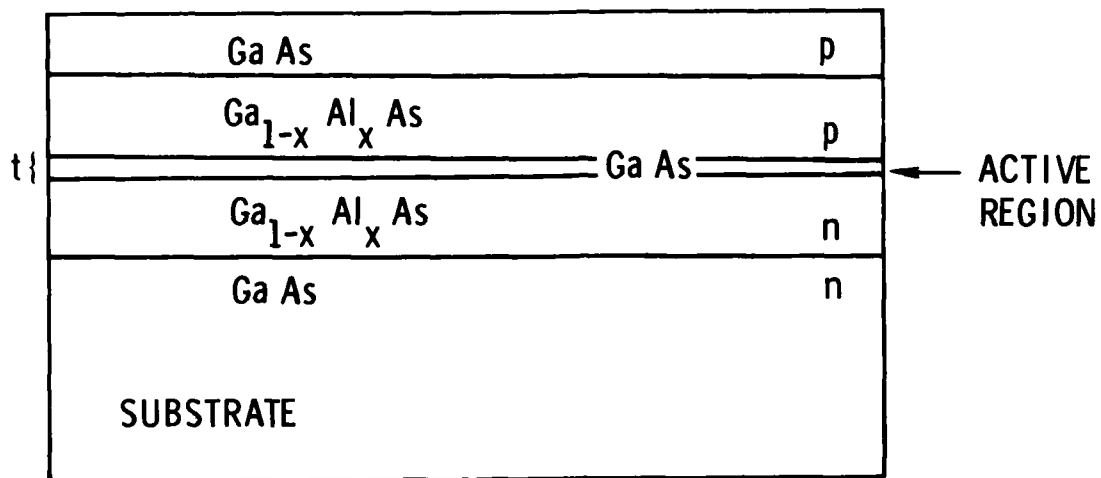


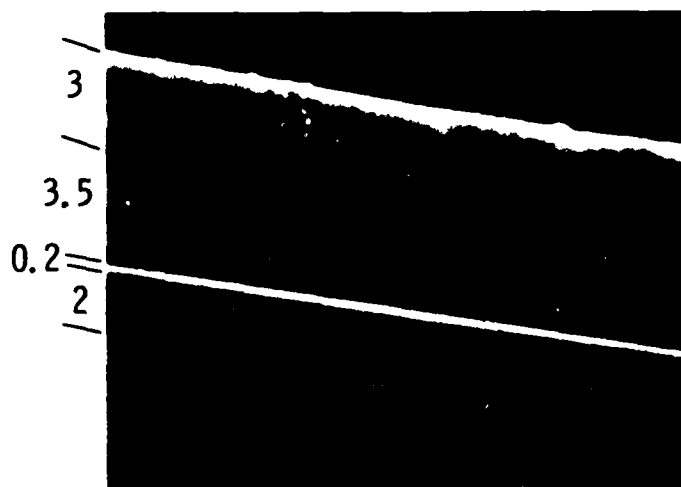
Fig. 2-3. Temperature Profile for Furnace Used in LPE



Fig. 2-4 Graphite Boat for LPE of DH Lasers



(a)



(b)

Fig. 2-5. DH Laser. (a) Epilayer structure. (b) SEM photograph of cleaved and stained epilayers.

heterostructure is shown in Fig. 2-5. The stain used for this photograph was Monsanto etch (1:1:4; HF:HNO₃:H₂O) for 10 sec.

After the double heterostructures were grown, ohmic contacts were fabricated. First, 500 Å of chromium and then 200 Å of gold were evaporated on the p-side, with the substrate at 300°C. Then, the samples were thinned to 7 mil thick, and 2000 Å of AuGe was evaporated on the p-side, with the sample at 180°C. These contacts were then alloyed by heating to 300°C for 3 min while still in the vacuum system. As part of this contract, new ohmic contact techniques were developed, which will be described later in this report. After application of ohmic contacts, the wafer was cleaved into bars 16 mils wide and then scribed into dice 7 mils wide. The dice then were mounted on a TO-5 header with indium solder, and a gold wire lead was attached with a thermo-compression bonder.

Laser thresholds were measured by monitoring the light output through a monochromator. The results are summarized in Table 2-1. The results demonstrated that we could easily and reproducibly achieve cleaved double-heterostructure GaAs lasers with state-of-the-art properties, and work was begun on development of a high-brightness double heterostructure (DH) laser using distributed Bragg reflector (DBR) structures, a beam expander, and an output collimator.

First, a preliminary design study was carried out. The results of this study indicated that the integrated optics laser source could most conveniently be fabricated by means of chemical etch techniques. The structure decided upon is shown in Fig. 2-6, and is called an asymmetric large optical cavity (ALOC).

The high-brightness integrated-optics laser source requires an active laser layer coupled to a passive waveguide layer (the region in which beam expansion takes place). The passive waveguide layer must have a composition different from the laser layer in order to minimize absorption loss and inefficient operation. The need for different layer compositions requires the use of different melts during the liquid-phase epitaxy (LPE) epigrowth process. In the original proposal, it was suggested that this could be achieved

Table 2-1. Experimental Results for Double Heterostructure Lasers

Wafer	x	t, μm	Average Measured Threshold, kA/cm^2	Average Measured Threshold, kA/cm^2	Wave-length $\lambda, \text{\AA}$
L7	0.47	0.2	2.4 ± 0.5	1.9	8750 ± 50
L8	0.47	0.6	3.8 ± 0.8	2.0	8825 ± 25
L10	0.47	0.1	2.6 ± 0.9	2.0	8600 ± 20
L11	0.44	0.46	4.4 ± 1.5	2.9	8800 ± 70

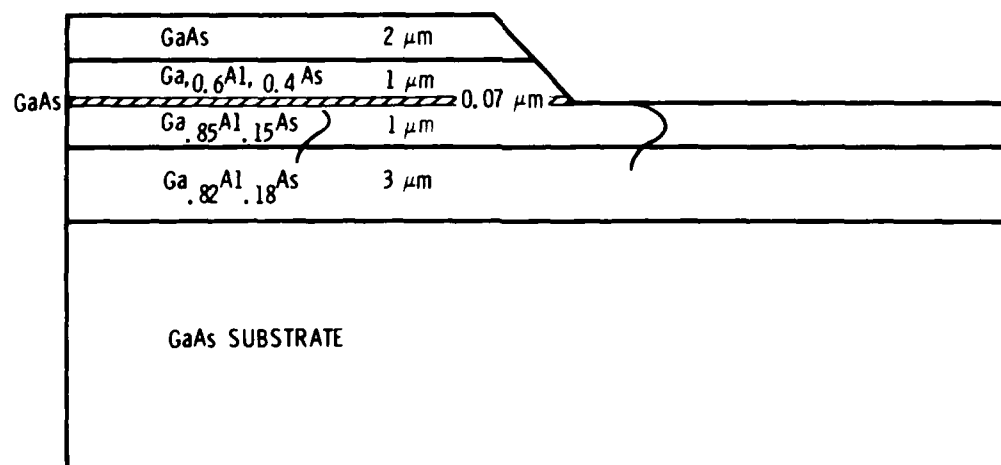


Fig. 2-6. Epilayer Structure, Integrating Laser, and Passive Waveguide on Same Substrate. Planar epitaxy with chemical etch and ion milling used for measurements.

by nonplanar epitaxy. During the design study, however, it was discovered that the ALOC structure allows for planar layers to be grown and then the active-passive transition to be fabricated later by chemically etching through a photoresist mask. In the active region, the guided light is not confined only to the laser layer but extends throughout the waveguide layer. When the absorbing GaAs layer in the passive region is removed, the light propagates in the waveguide layer. A detailed analysis of the design of the DBR structure is included as Appendix B.

The result of this analysis was the calculation that the layer structure shown in Fig. 2-7 should have a threshold less than 2 kA/cm^2 and an efficiency 87% that of typical cleaved lasers. An additional conclusion of the analysis is that there is a five-layer symmetric large optical cavity (SLOC) structure, which has an even lower threshold and higher efficiency. However, because of the greater difficulty in fabrication, we decided to make our first high-brightness lasers using the asymmetric large optical cavity (ALOC) structure. Later research efforts to increase efficiency of the devices can be directed toward development of the SLOC.

The decision was made to use the ALOC structure, and, accordingly, crystal growth was begun in order to fabricate these epilayers. Six wafers were grown, and cleaved lasers were fabricated. The structure is shown in Fig. 2-7. The results are summarized in Table 2-2. Lasers L15 and L16 produced the expected results, that is, the thresholds for the ALOC were lower than any of the DH lasers. In fact, Fig. 2-8 demonstrates this dramatically by showing the threshold plotted on the same scale as the DH lasers. The results of these L15 and L16 ALOC lasers gave us confidence in the basic design. There were problems, however, with samples L17 through L19, indicating that there was something wrong with the thin active regions. Later the cause was discovered. It was attributed to the use of a too high aluminum concentration in the layer above the active region, which caused strain in very thin active regions.

In parallel with these crystal growth runs, we began to study selective chemical etching of the epilayers. For this purpose, we grew layers L20

2 μm	GaAs	CAP	
2	47% AlAs	p-ISOLATION	LAYER
t	GaAs	LASER	
1 μm	18% AlAs	WAVEGUIDE	LAYER
2 μm	20% AlAs	n-ISOLATION	LAYER

Fig. 2-7. ALOC Laser Layer Structure

Table 2-2. ALOC Laser

Wafer	t, μm	J_{ave} , kA/cm^2	J_{min} , kA/cm^2	λ , \AA
L15	0.2	2.8 ± 1.1	1.4	8760 ± 1000
L16	0.3	1.6 ± 0.4	1.0	8750 ± 30
L17	0.1	No lasing		
L18	0.15	4.0	4.0	8550
L19	0.1	No lasing		

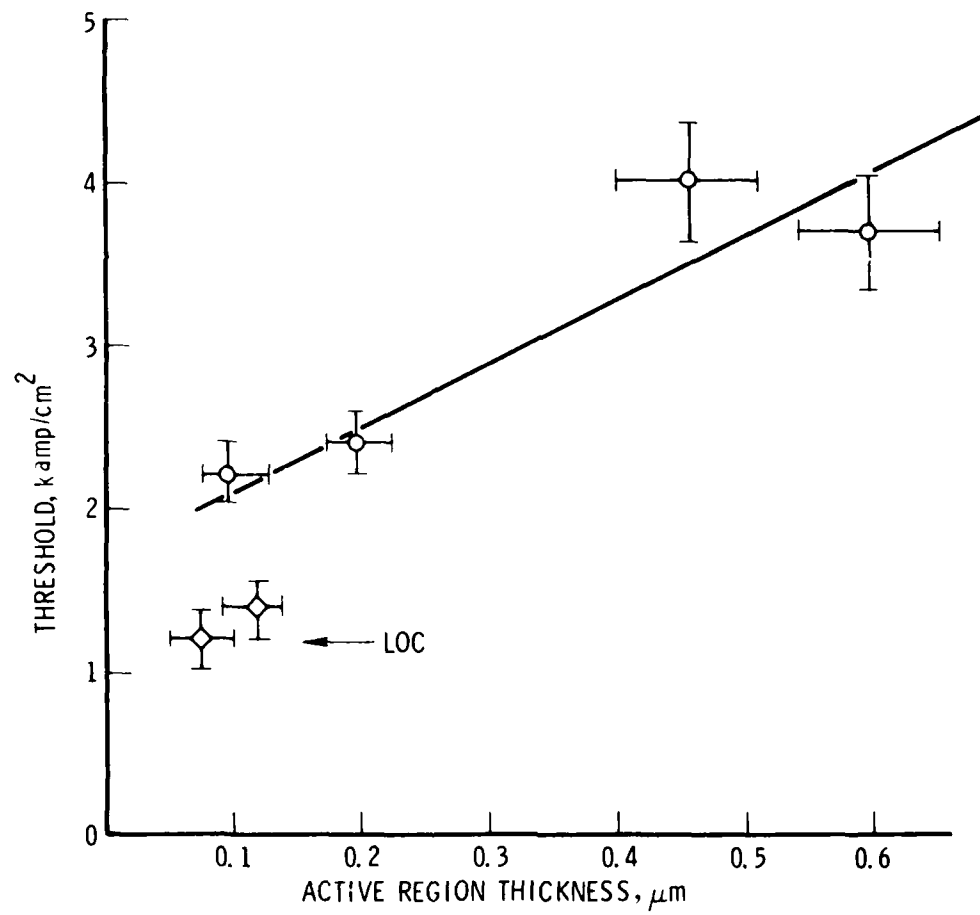


Fig. 2-8. DH Laser

through L24, which were not double heterostructures, but were layers of high AlAs concentration grown on layers of low AlAs concentration.

In all these runs, we found that the layers we grew had microscopic pits, which did not seem to interfere with cleaved laser operation, but which were unacceptable for the high-brightness laser. It became clear that we required more sophisticated crystal growth techniques. We attributed these pits to aluminum oxide, and decided to develop a new boat that would permit us to add the aluminum dopant only after an initial prebakeout period. We followed a procedure outlined by one of the research scientists at RCA.* This boat was designed and fabricated and is shown in Fig. 2-9.

A sliding one-piece lid was made for the boat, which would drop into the melt wells when positioned properly. This lid is shown at the bottom of Fig. 2-9(a). The boat is loaded before growth, with the aluminum dopants sitting on the edges between melt wells. The lid rests on top of the melt wells, positioned so as to be able to push the aluminum into the melts when required. After a preliminary bakeout the lid is pushed over the melts, the aluminum falls in, and the lid drops down onto the melt. The melts are then taken to growth temperature.

Experiments began with the newly designed boat. Crystals N1 through N4 were simple double heterostructure lasers, and O1 through O4 were grown as low-threshold symmetric large optical cavities. It appeared that most of the pits were eliminated, but there appeared to be excess GaAs on the surface, which made it difficult to use for the chemical etching.

We decided that the best way to provide a good quality thin cap was to grow a surface layer of $\text{Ga}_{0.2}\text{Al}_{0.8}\text{As}$ on top of the cap. It would not matter if this layer were uneven since the very first step in the processing would be the removal of this layer by HCl.

Wafers A1 through A12 were grown as ALOC lasers with this AlAs surface layer. These layers were very flat and were of the desired thickness. A

*M. Ettenberg, RCA Corporation, private communication.

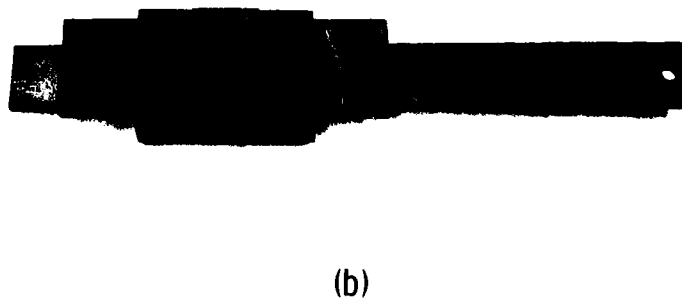
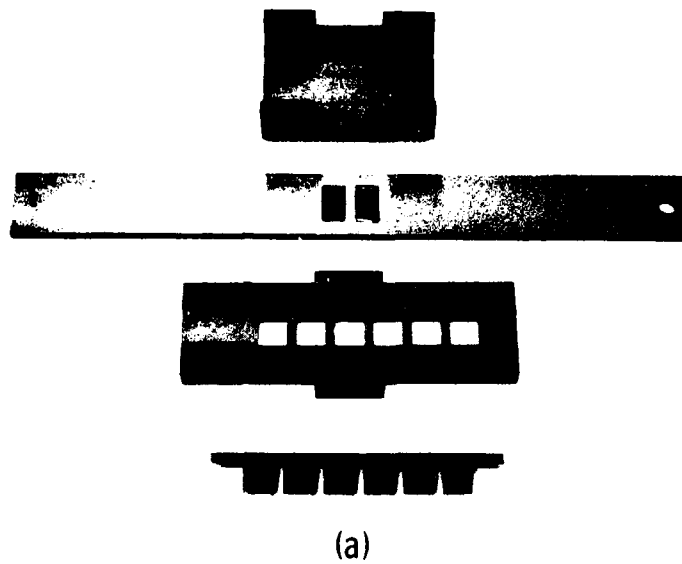


Fig. 2-9. Six-Well Graphite Boat for LPE Growth of ALOC Laser
(a) Disassembled view. (b) Assembled view.

typical SEM of a cleaved and stained wafer is shown in Fig. 2-10. Processing was begun on all these wafers before making the active or passive lasers. The layer structures grown are summarized in Table 2-3.

We also decided that one crystal growth furnace was insufficient for the demands of the program, so a second identical furnace was introduced and plumbed.

Next, wafers A13 through A16 were grown. These were ALOC structures essentially identical to A1 through A12 and were intended for DBR lasers. The layer surfaces were smooth, and the thicknesses were as expected. During this period of growth, it was known that the current-voltage (I-V) characteristics of lasers made for ALOC material were poor, but the reason for this was not understood. After the growth of A16, however, it was discovered that they were poor because the surface AlAs layer that was to have been etched away was not in fact fully removed. Because we had anticipated its removal, this layer had not been electrically doped. The incomplete removal resulted, therefore in an i-layer instead of an ohmic contact. With this fact now fully understood, the ALOC heterostructures were grown with p-doped surface layers. Layers A17 through A23 were grown with this configuration.

As a result of later discoveries, that is, the AB etch removed layers with lower AlAs concentration, the AlAs concentration was reduced for A20 through A22. When it was discovered that thin active and waveguide regions required even lower AlAs concentrations to lase, the last sample in this series was grown with considerably lower AlAs concentrations. A summary of the samples grown and their structure is provided in Table 2-4.

As a result of passive waveguide tests, we decided to grow a buffer layer of GaAs on the substrate before the first GaAlAs layer was grown. There is evidence in the literature that this would reduce the dislocations and improve the quality of the passive waveguides, a necessity for efficient high-brightness lasers. Therefore, crystals C1 through C6 were grown. The layer structure for the C-layers is given in Table 2-5. Because the buffer layer required the use of one of the melt holes of the boat designed for the ALOC structure, the surface layer could not be grown. As a result, the cap layer was very thick, and these wafers were not suitable for DBR lasers.

Table 2-3. Layer Structure of Wafers

Wafer	n-Isolation		Waveguide		Active t, μm	p-Isolation		Cap t, μm
	x	t, μm	x	t, μm		x	t, μm	
A1	0.3	3.6	0.29	0.43	0.11	0.6	8.6	1
A2	0.3	12	0.29	1	--	0.6	8	1
A3	0.3	15	0.29	2	--	0.6	6	3
A4	0.2	8	0.18	1	--	0.6	9	1
A5 ^a								
A6	0.32	8 ^b	0.29	3 ^b	0.46 ^b	0.6	4.6	2
A7	0.32	3.9	0.29	0.7	--	0.6	3.3	3
A8	0.32	2	0.29	1.6	0.46	0.6	2.3	3
A9	0.32	3	0.29	1.2	0.3	0.6	5	3
A10 ^c								
A11	0.32	3.8	0.25	--	0.2	0.6	5.1	1.8
A12	0.4	3.7	0.9	1.2	0.6	0.6	7	1.8

^aBad growth, need to readjust furnace profile.

^bGrown thick to assist in identifying layers.

^cBad growth, mistake.

Table 2-4. Layer Structure for ALOC Wafers

Wafer	n-Isolation		Waveguide		Active	p-Isolation		Cap
	x	t, μm	x	t, μm	t, μm	x	t, μm	t, μm
A13 ^a								
A14 ^a								
A15	0.6	0.27	0.3	1.1	0.15	0.62	2.8	3.5
A16 ^b								
A17	0.4	3.14	0.29	1.1	0.27	0.62	3.5	0.8
A18	0.4	3.5	0.29	1.1	0.27	0.62	3.8	0.4
A19	0.4	2.3	0.29	0.96	0.5	0.62	2.5	2.4
A20	0.3	3.5	0.2	--	0.5	0.5	4	0.5
A21	0.3	3.6	0.2	0.4	--	0.5	4.8	0.6
A22	0.3	2.6	0.2	0.6	0.15	0.5	2.8	1.6
A23	0.3	1.2	0.1	0.6	0.15	0.3	3.2	0.5

^aAluminum did not fall in.^bOxygen leak.

Table 2-5. DBR Structure E-Series

Wafer	n-Isolation		Waveguide		Active		p-Isolation		p-Cap	FP Threshold,		Comments
	x	t, μm	x	t, μm	x	t, μm	x	t, μm	t, μm	kamp/cm ²		
E10	0.30 ^a 0.28 ^b	3.5	0.10 0.14	0.6	0.0	0.4	0.30 0.35	2.8	0.0	1.1	1.8	Good F-P laser.
E12	0.35	3.2	0.15	1.0	0.0	0.2	0.35	5.4	0.0	2.3	3.5	Thin active layer.
E13 ^c	0.30	3.8	0.10		0.0		0.35	2.7	0.0	2.7	-	Plug did not fall in.
E14	0.35 0.30	3.4	0.15 0.12	1.6	0.0 7.4	0.07 0.13	0.35 0.30	2.7	0.0 0.0	4.4 2.5	4.5	Very-thin active. High Al concentration.
E15	0.35 0.30	3.9	0.15 0.11	1.3	0.0 0.032	0.15	0.35 0.23	3.6	0.0 0.02	4.3	3.6	Waveguide too thick. Good surface.
E16	0.35	2.5	0.15	1.0	0.0	0.25	0.35	2.1	0.0	2.3	-	Plug did not fall in.
E17	0.35	2.4	0.15	1.1	0.0	0.0640	0.35	2.9	0.0	1.4	7.0	Active layer very thin. Caused high threshold.
E18	0.35	0.5	0.15	1	0.0		0.35	1.1	0.0	0.3	-	Plug did not fall in.

^aPredicted.^bMeasured.^cBad run.

A new boat was therefore designed with an additional melt hole for the buffer layer. This boat was also designed to make it possible to grow samples twice the size of the previous boat. The new boat design did increase the waveguide performance and lower the threshold.

While this boat was being built, a new E-series of DBR crystals was grown in a six-well small boat. Previous runs, C1 through C6, had indicated that growth at 800°C was not as good as at 850°C because of composition phase changes at 800°C. These E-series runs produced fairly good DBR samples, but they had a waveguide thickness greater than 0.6 μm , which was later decided to be the optimum desired thickness. Also, the active layer tended to be too thin causing thresholds greater than 2 kamps/cm².

When the new seven-hole boat was ready, a new temperature profile had to be made of the furnace containing the new boat. A profile was made with a gradient 1°C colder at the final melt hole than the first hole and a neutral top-to-bottom gradient. We did not realize until the complete series of crystals (Table 2-6) were grown that the oven profile caused etchback of the just grown epilayer. The proper profile should be flat or increase in temperature about 1°C from the first hole to the last hole to prevent etchback.

Because the epilayers grown in the first five crystals of the H-series were uneven, a boat modification was made to permit excess melt to flow into channels along corners of the melt well. We thought this modification would help the layers grow flat and parallel, since the channels would equalize the heights of all the melts and result in a uniform melt pressure from well to well. This modification did not produce the hoped for improvement in layer uniformity. The typical layer variation for the H-series crystals is shown in Fig. 2-11. The corresponding surface roughness of the same crystal is shown in Fig. 2-12. Typical layer uniformity and surface smoothness for LPE-grown crystals are illustrated in Figs. 2-13 and 2-14. At present, we are experimenting with the old six-well boat and the latest seven-well boat with flat and increasing temperature profiles. The preliminary results indicate much smoother layer structure.

The H-series crystals were grown from a new ingot of substrate materials that had an etch-pit density of 1500/in². In previous runs of A-series

Table 2-6. DBR Structure H-Series

Water	Substrate	Reflection	Waveguide	Action	Pre-fabrication	p-Cap	t, μ m	FP Threshold, kmp/cm ²	Comments
x	t, μ m	x	t, μ m	x	t, μ m	x	t, μ m		
H3	0.0	0.0	0.15	0.0	0.12	0.15	1.4	-	Plug did not fall in. Poor surface quality.
H4	0.0	0.0	0.15	0.0	0.12	0.15	1.4	3.5	Good crystal during FP process. Polished too thin for handling.
H5	0.0	0.0	0.15	0.0	0.19	0.35	3.5	2.6	Good crystal. New ingot substrate material.
H6	0.0	0.0	0.15	0.0	0.28	0.45	3.2	1.4	Waveguide Al concentration tapers from 10% at bottom to 2% in top. Too thick.
H7	0.0	0.0	0.15	0.0	0.14	0.45	3.2	-	Plug did not fall in. Al did not totally go in second layer.
H8	0.0	0.0	0.15	0.0	0.21	0.45	4.0	1.4	Good crystal except for optical properties in waveguide.
H9	0.0	0.0	0.15	0.0	0.25	0.45	3.6	1.0	Dirty surface.
H10	0.0	0.0	0.15	0.0	0.18	0.45	3.3	1.6	Al reacted with graphite, causing low concentration in melts.
H11	0.0	0.0	0.15	0.0	0.23	0.45	2.6	1.0	Substrate scratches. Too much Al in waveguide, carried over from second melt.
H12	0.0	0.0	0.15	0.0	0.22	0.45	3.9	0.8	Substrate had too many scratches.

aBad run.
bPredicted.
cMeasured.

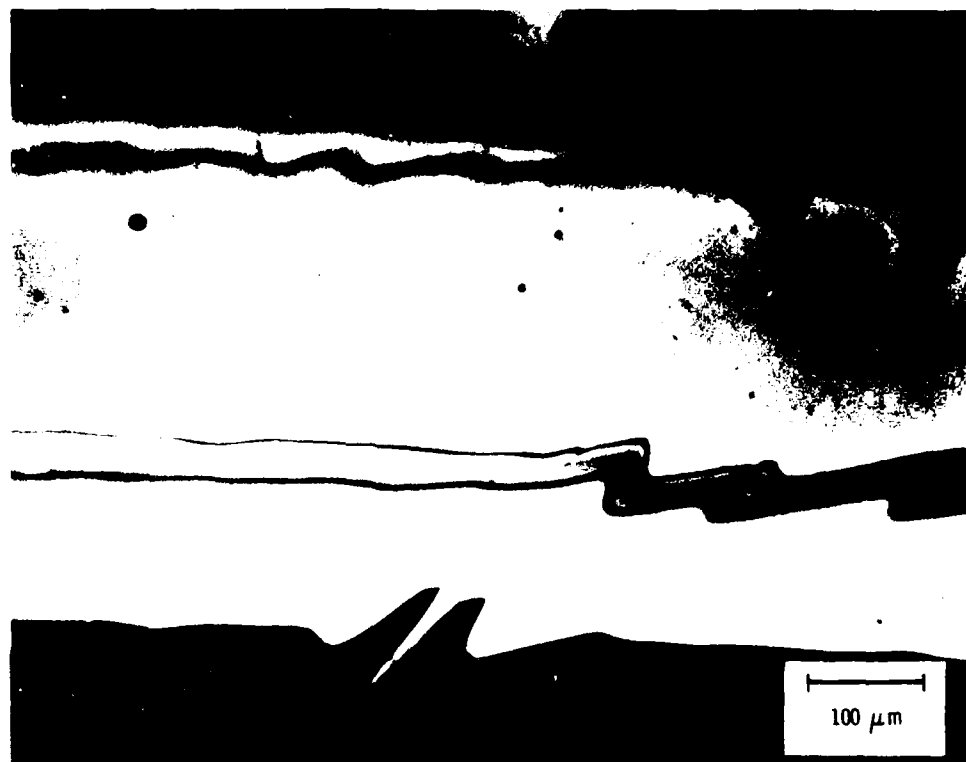


Fig. 2-11. Angle Lapped Section of Sample H3 with Epilayer Variation Shown

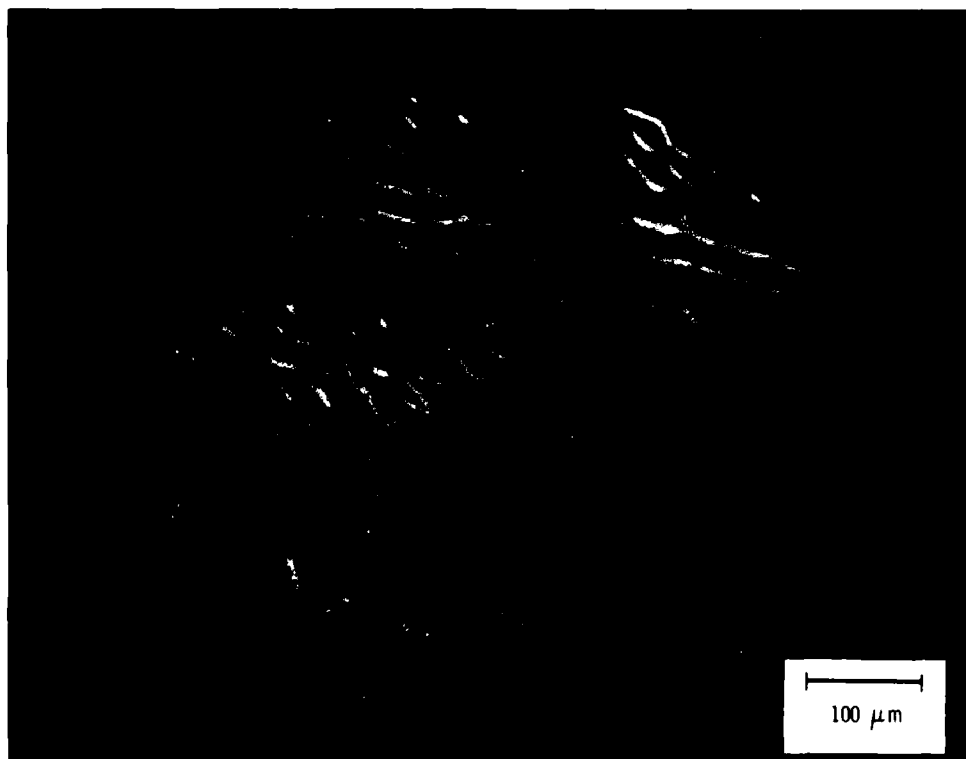


Fig. 2-12. Surface of Sample H3 with Surface Roughness Shown

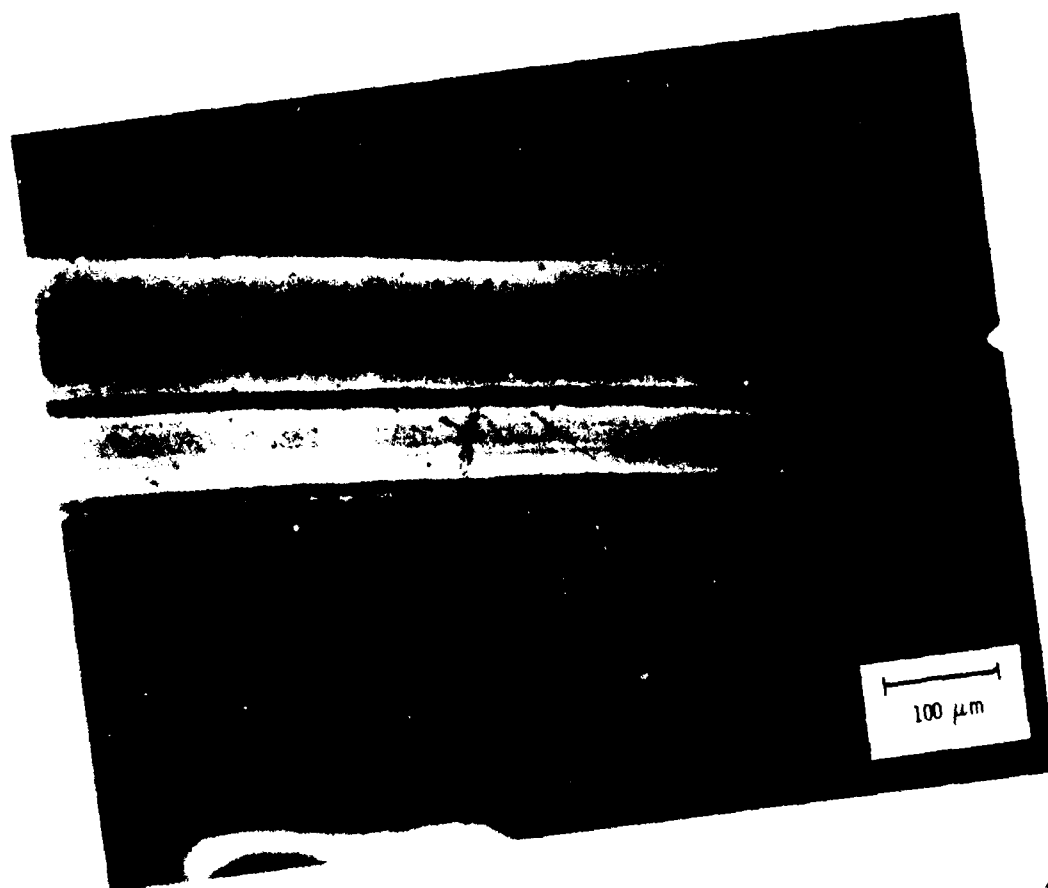


Fig. 2-13. Angle lapped Section of Sample LDL-102. Even layers are typical for good LPE growth.

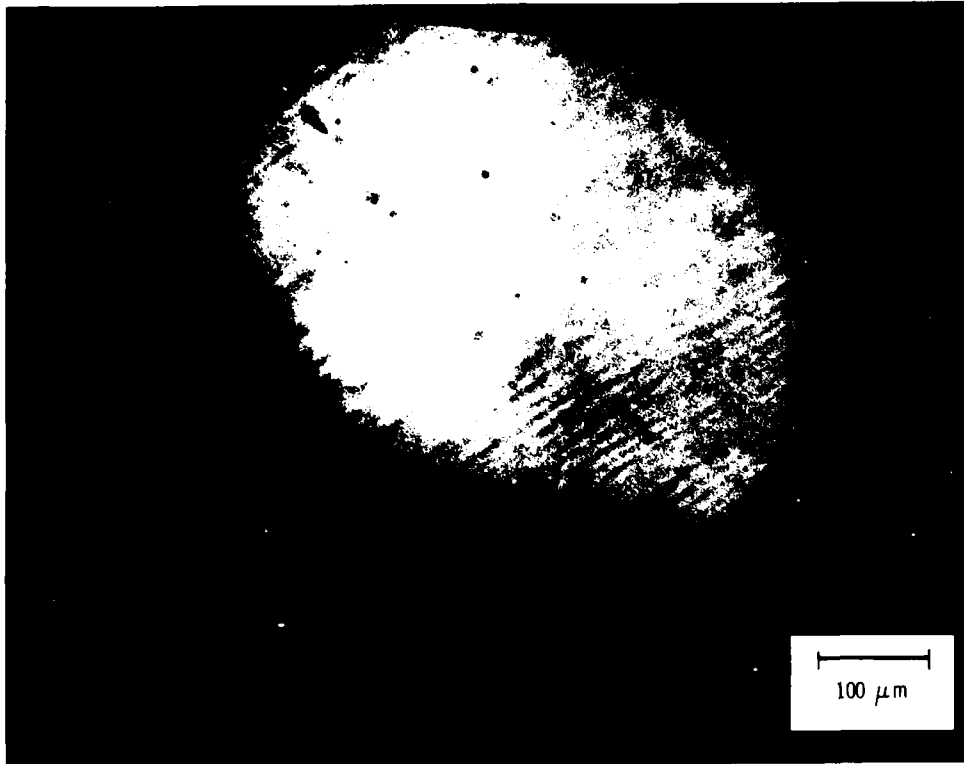


Fig. 2-14. Surface of Sample LDL-102. Only slight terrace formation is apparent.

through E-series crystals substrates with an etch-pit density of 1000/in.² or less were used. The difference in etch pit density did not seem to adversely affect the resulting + laser thresholds. Before we discovered that the furnace profile used for the H-series was incorrect, we checked the orientation of the H-series substrates by x-ray diffraction. We found that the substrates were oriented about 1 deg off the 100 axis, which is very close to the optimum orientation of 0.8 deg off the 100 axis for suppression of terrace formation for growth at 850°C.^{2,3} However, to achieve the high optical and electrical properties over the large areas required to make a high-brightness laser, we completed the design and are presently assembling a metal organic chemical vapor deposition (MOCVD) system. The expected capabilities of the MOCVD system are described in Section 2.2.

With proper furnace temperature profiles and control, a pure hydrogen atmosphere, a well-designed boat, and high-quality substrates at the proper orientation, we hope to solve the problem of producing crystals with high-quality optical and electrical properties for low-threshold DBR lasers.

We had two crystals grown in the large optical cavity configuration by Laser Diode Laboratories (LDL). The measured parameters of the LDL crystals are shown in Table 2-7. As shown in Figs. 2-13 and 2-14, the layers are even, and the surface is relatively smooth. The optical quality, measured by waveguiding through the crystal, was very good. The Fabry-Perot (FP) lasers fabricated from the LDL material generally were a factor of 2 or more higher than the H-series thresholds. The DBR lasers that were fabricated during this contract period were made from sample LDL-102.

2.2 METAL ORGANIC CHEMICAL VAPOR DEPOSITION SYSTEM

The metal organic chemical vapor deposition (MOCVD) system being designed and built at Aerospace consists of a number of subsystems. The systems structure is shown in block diagram form in Fig. 2-15. A hydrogen carrier gas is bubbled through the metal organic liquids trimethyl gallium, trimethyl

²D.L. Rode, R.W. Wagner, and N.E. Schumaker, Appl. Phys. Lett. 30, 75 (1977).

³D.L. Rode, Phys. Status Solidi 32, 425 (1975).

Table 2-7. DBR Structure LDL Series

Insulator	x	t , μm	κ	t , μm	Dielectric	κ	t , μm	κ	t , μm	p-Isolation	κ	t , μm	p-Cap	κ	t , μm	FP Threshold	Comments
0.011	0.2	-	0.34	2.27	0.11	0.86	0.15	0.25	0.26	3.4	0.02	2.5	~5.0				Difference in Al concentration between active and waveguide layers should be 0.10. In both crystals, 0.05 difference is marginally acceptable.
0.186	0	-	0.46	1.9	0.13	0.55	0.08	0.12	0.37	4.4	0.01	1.6	~5.0				

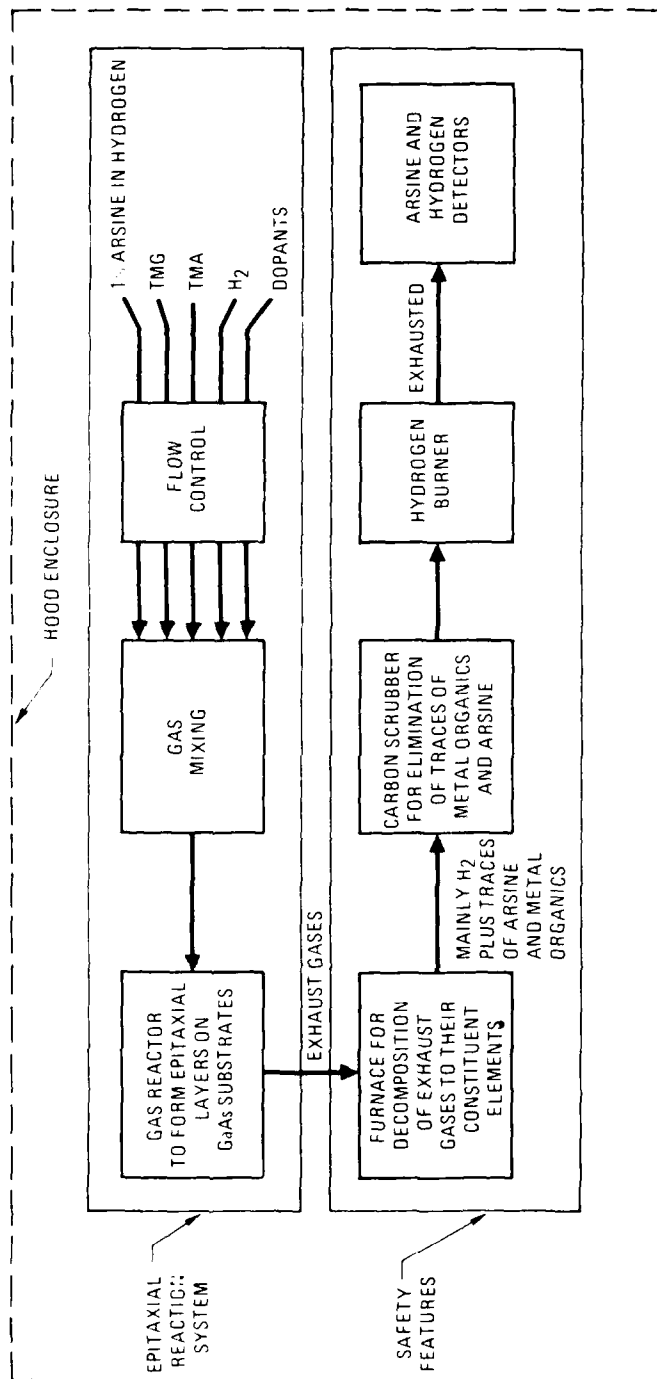


Fig. 2-15. Block Diagram of MOCVD System with Associated Safety System

aluminum, and the dopants diethyl zinc and diethyl telluride. These liquids are all kept at constant temperatures in constant temperature baths. The various streams of carrier gas now saturated with the different metal organic components are mixed with arsine gas and finally diluted with hydrogen. The mixture enters the reaction chamber and reaction occurs upon a substrate heated on a rotating pedestal to approximately 700°C. The exhaust gas is then decomposed in a furnace heated above 300°C. The gases exiting this scrubber are mainly H₂, traces of arsine and metal organics, and vapors of the unreacted metals. These trace components are eliminated with a small in-line carbon scrubber. The H₂ is then burned, and the exhaust gas is sampled for arsine by an arsine detector. The dashed lines in Fig. 2-15 indicate that parts of the system shown in the figure are in a fume hood. The parts of the system not shown that are outside the hood are the vacuum system or some part of the gas handling system.

Figure 2-16 is a detailed presentation of the gas-handling system used for MOCVD. The important points to be noted are: (1) The system is entirely stainless steel and connections are VCR type (two opposing ring-like faces bite into a stainless-steel washer). (2) All valves have welded bellows, and air-operated valves are used in key positions for safety and ease of operation. (3) Flow control valves can either be manually operated or remotely operated using a computer. The system has been designed for safety, for versatility, for system integrity needed to do high-quality semiconductor growth, and for the experimental control needed for reproducibility and composition control. Future needs will be taken into account in design of the system (Table 2-8).

It is our belief that the MOCVD system will permit the growth of uniform layers over large (0.5 by 0.5 cm) areas with high electrical and optical quality because of the excellent growth characteristics of MOCVD material as compared to liquid-phase grown material. Table 2-9 provides a comparison of the growth characteristics of the two techniques. MOCVD appears superior to LPE growth in all respects. MOCVD is more reproducible than LPE because MOCVD growth does not depend as critically on temperature for the growth rate or the prior history of a melt for layer composition; it is easier to grow a layer to

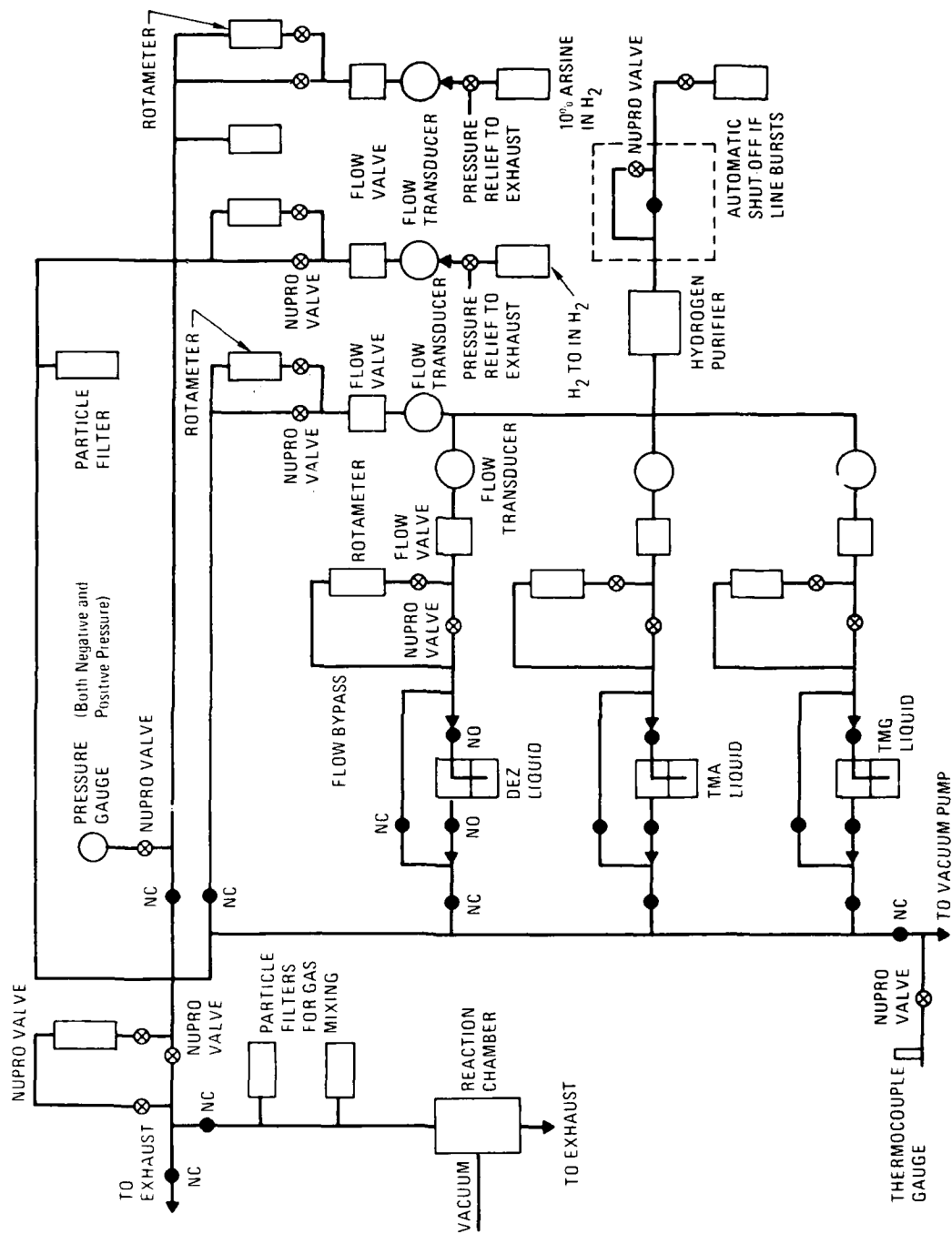


Fig. 2-16. Gas-Handling System for MOCVD

Table 2-8. Comparison of Capabilities of MOCVD and LPE Systems

Parameter	System	
	MOCVD	LPE
Different Material Systems (same apparatus)	Yes	No
Controlled Vertical Layer Composition	Yes	No
Artificial Crystal Lattices	Yes	Virtually impossible
Minimum Layer Thickness, Å	50	500
Turnaround	1 day	1 week

Table 2-9. Comparison of Characteristics of Growth by MOCVD and LPE Systems

Parameter	System	
	MOCVD	LPE
Reproducibility	Excellent ^a	Poor ^b
Layer Composition Homogeneity	Excellent ^a	Fair to good ^b
Layer Thickness Variations	Minimal ^a	Intrinsic variations ^b
Layer Composition Accuracy	Excellent	Fair to good
Final Surface Morphology	Smooth	Rough

^aNonequilibrium

^bUnstable equilibrium

a specific thickness and composition and repeat the growth of these layers with MOCVD. LPE layers are not homogeneous in composition from top to bottom because the composition of the melt is constantly changing during deposition. This is not a problem for MOCVD where gas is constantly entering the chamber, flowing by the substrate, and exiting from the chamber. In this case, a steady-state condition is set up and growth, if uninterrupted, remains unchanged with time. There is a minimal variation in thickness across the MOCVD grown layers because the rate of growth is not a sensitive function of temperature, and any temperature fluctuations across the heating stage do not show up as thickness variations. This is a very serious problem for LPE grown material because LPE is so sensitive to temperature. Desired layer composition can be obtained with MOCVD, but it is harder to obtain with LPE growth. The growth of GaAlAs by LPE involves the addition of aluminum to the melt in situ. It is not necessarily true that all the aluminum will dissolve in the melt nor that the solution will be uniform. The resultant composition of the layer can vary greatly from the desired composition. This error is amplified by the fact that a small error in the concentration of aluminum in the melt causes a large error in the amount of aluminum in the GaAlAs layers. The morphology of the top face and interfaces between the layers is poorer for LPE grown material than MOCVD material. The top face has poor morphology because there is no way to remove the excess liquid on the sample before removing the sample from the growth chamber. The interfaces have poor morphology because the underlying layers are subjected to a nonequilibrium environment, and there is some solution and dissolution of material from the underlying layer when the new layer is initially grown. No such problem occurs with MOCVD because it occurs so far from equilibrium that the only two processes that can occur are deposition or no deposition of a new layer; evaporation of a layer does not occur at normal working temperatures.

MOCVD is a more versatile experimental tool than LPE. With MOCVD, materials that have not been duplicated with LPE are synthesized. One can, in principle, make artificial lattices of any complexity with individual layer thickness to 50 Å. With electrical control of the flow controllers, it is possible to control the vertical composition or doping of a layer. None of

these controls on composition, doping, or thickness can be matched with the current LPE system.

The MOCVD project started in late 1978. At this time, we have all of the critically needed components that are necessary for a working system. The laboratory that is to house the experiment is near completion, and we are in the process of assembling the system. The system will take another three months for completion, but will probably not run until the early part of the summer because of the additional equipment that has to be installed to meet safety standards.

The experiment that we are setting up is a very complex and ambitious project. Instead of starting with a simple inflexible system, we have designed and are building a very sophisticated and very flexible system that we will be able to modify in the future to meet our needs.

3. MATERIAL CHARACTERIZATION

3.1 LAYER THICKNESS AND COMPOSITION

In order to predict and evaluate both device and crystal growing performance, the epilayers must be fully characterized with respect to layer thicknesses and compositions. Layer thicknesses are determined by means of both optical and electron microscopy. Figure 3-1 is an SEM photograph of a cleaved edge of sample H5.

Three techniques have been investigated for obtaining layer compositions: (1) photoluminescence; (2) electron dispersive analysis by x rays (EDAX); and (3) ion microprobe mass analysis (IMMA). Layer compositions of a 2-deg-angle lapped specimen were obtained with the use of all of these techniques.

Because it yields real-time data and does not require the use of a correction factor, the IMMA technique has been deemed the most accurate and useful of the three. The photoluminescence data, while not inconsistent with the IMMA data, must be corrected for wavelength shifts because of dopants. This effect leads to an underestimation of the aluminum content of a given layer. In addition, the photoluminescence data must be taken on a point-by-point basis and is not, therefore, real time. The EDAX technique suffers from similar drawbacks. While not influenced by dopants, the L_{α} emission line of arsenic interferes with both the K_{α} aluminum line and the K_{α} gallium line. Stripping the arsenic spectrum mathematically from the composite spectrum alleviates this problem to some degree but still yields what appears to be a consistently low aluminum concentration. Finally, as in the case of the photoluminescence technique, data must be gathered on a point-by-point basis and is not real time.

Composition traces obtained by means of the IMMA technique (sample H5) are shown in Fig. 3-2. This technique has been used on a routine basis to determine AlAs concentrations.

EXTRA LAYER 7.4 μm →

CAP 2.6 μm →

p-ISOLATION 3.7 μm →

ACTIVE 0.21 μm →

WAVEGUIDE 0.75 μm →

n-ISOLATION 4.2 μm →



Fig. 3-1. SEM Photograph of Cleaved Edge of Sample H5

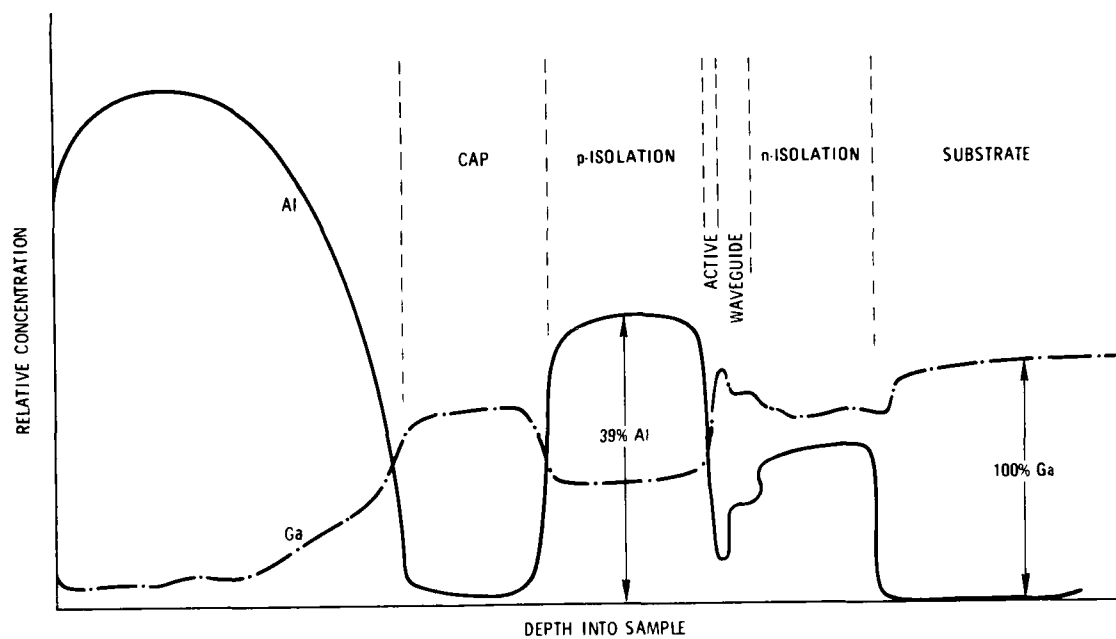


Fig. 3-2. IMMA Scan for Sample H5

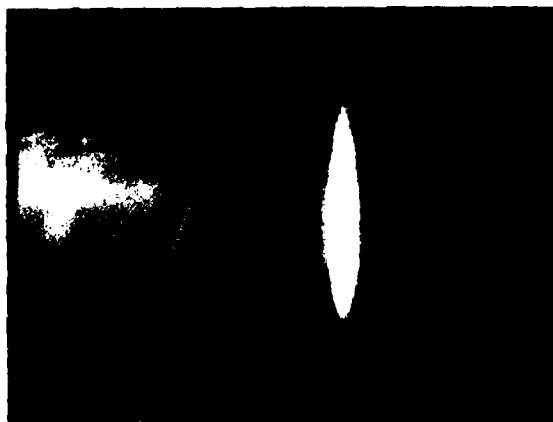
3.2 WAVEGUIDE EVALUATION

Experiments were begun on the guiding of 1.15- μ m light in the GaAlAs and GaAs waveguides to aid in the development of the beam expander and to evaluate the material quality for DBR lasers. In the early samples, it was discovered that the optical quality of the GaAlAs layers grown by LPE was of poor quality. In Fig. 3-3, near-field photographs of light guided through various epilayers are shown. The vertical light is the guided light; the haze left of the line is light going through the substrate; the haze right of the line is light going through the air. In Fig. 3-3(a), the light is shown guided through a piece of vapor phase epitaxial GaAs, which was the same material as used for the passive studies of beam expansion. The guided light forms a smooth line, corresponding to good-quality epitaxial material.

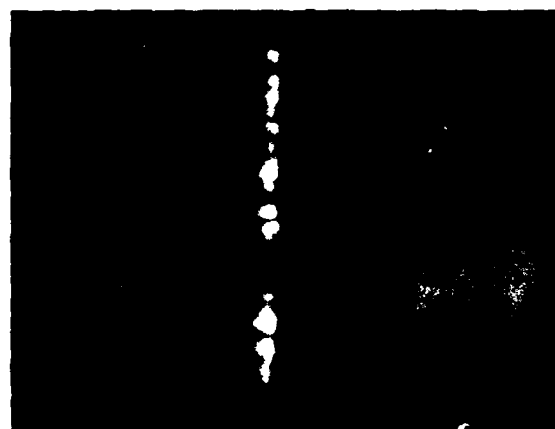
In contrast, passive guiding experiments with sample A19 indicate that there is a tendency for the light to break up as it travels in the waveguide, causing a characteristic beading pattern shown in Fig. 3-3(b).

A program was therefore begun to improve the quality of the epilayers grown by LPE. It was discovered that if a GaAs buffer epilayer is grown first, that is, before the layers of GaAlAs, the quality of the waveguides is improved. In Fig. 3-3(c), light has been guided through sample C2, an epilayer that includes a buffer GaAs layer. There is almost no beading, and the quality of the optical waveguide is almost as good as that of the vapor-phase epitaxy (VPE). The structure of sample C2 is shown in Fig. 3-4, including the GaAs buffer layer. This buffer layer was included in all later DBR laser structures to improve their efficiency.

The effectiveness of the GaAs buffer layer is the result of the poor optical quality of the GaAlAs layers caused by nonuniformities in the refractive index that are caused by the nonuniform growth of GaAlAs around dislocations. It is a well-known fact that an epilayer of GaAs has fewer dislocations than the substrate upon which it is grown. By contrast, an epilayer of GaAlAs tends to increase the number of dislocations, since there is a slight lattice mismatch. Therefore, the buffer layer is required to remove as many dislocations as possible before the waveguiding GaAlAs layers are grown.



(a)



(c)



(b)

Fig. 3-3. Passive Waveguiding Through (a) Vapor-Phase Epitaxy of GaAs, (b) ALOC Material, and (c) GaAlAs LPE with Buffer Layer

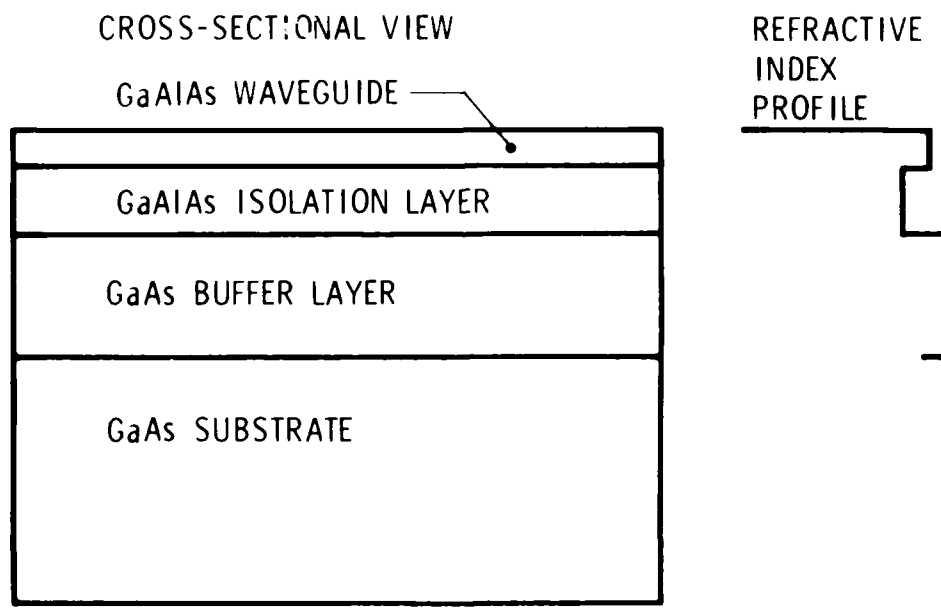


Fig. 3-4. Passive Waveguide Structure Including GaAs Buffer Layer to Ensure Homogeneity

3.3 PHOTOLUMINESCENCE MEASUREMENTS

In the process of developing etch techniques for the selective removal of epilayers from the ALOC structure, we found it important to monitor whether or not the layer had indeed been removed. We developed a photoluminescence technique to make this evaluation.

A diagram of the experimental apparatus is shown in Fig. 3-5. The peak of the photoluminescence spectrum is a function of the aluminum concentration and the doping level. In Fig. 3-6, a map of the photoluminescence spectrum of a 2-deg angle lapped section of crystal 186 is shown. The photoluminescence peaks corresponding to the cap, p-isolation, active, waveguide, n-isolation, buffer, and substrate layers are indicated. In Fig. 3-7(a), a photoluminescence scan of sample 186E before processing is shown. After 20 min of ion milling, the scan shown in Fig. 3-7(b) indicates the cap layer has been removed and the p-isolation layer is exposed. After 10 min of exposure to AB etch, Fig. 3-7(c) indicates that the cap layer has been removed, and two peaks, corresponding to the active and waveguide layer, are seen. After an additional 5 min exposure to an AB etch, the active layer is removed, with only the waveguide layer exposed, Fig. 3-7(d).

This photoluminescence technique is used extensively in fabricating DBR lasers and also provides additional information on the quality of the crystal.

3.4 FABRICATION OF BROAD-AREA FABRY-PEROT LASERS

As a test of the electrical and lasing qualities of the grown material, broad-area Fabry-Perot (FP) lasers were fabricated, and their lasing spectra and threshold characteristics were obtained.

Figure 3-8 is a flow chart showing the sequence in which the material characterizing steps are performed. The results of the characterization steps for the E, H, and LDE series of LDE grown material are summarized in Tables 2-5, 2-6, and 2-7, respectively.

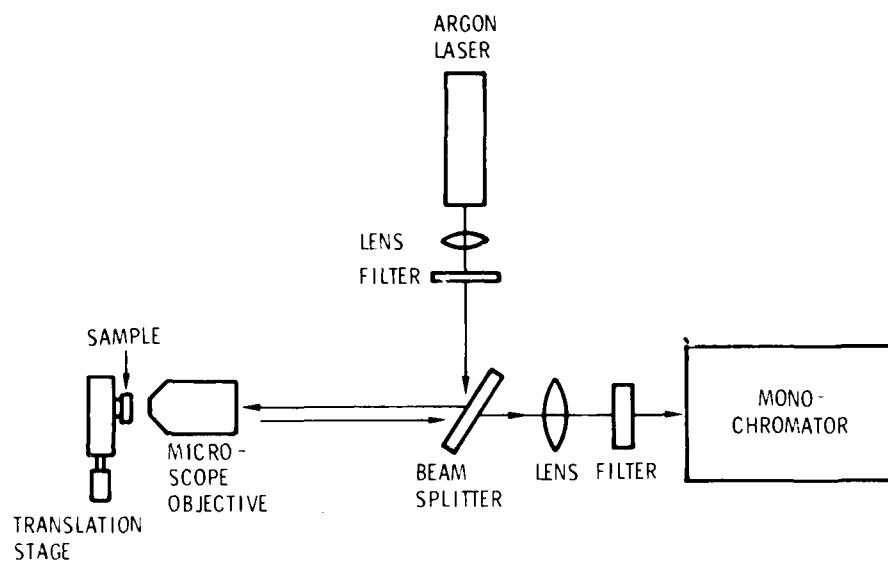


Fig. 3-5. Experimental Apparatus for Photoluminescence Measurements

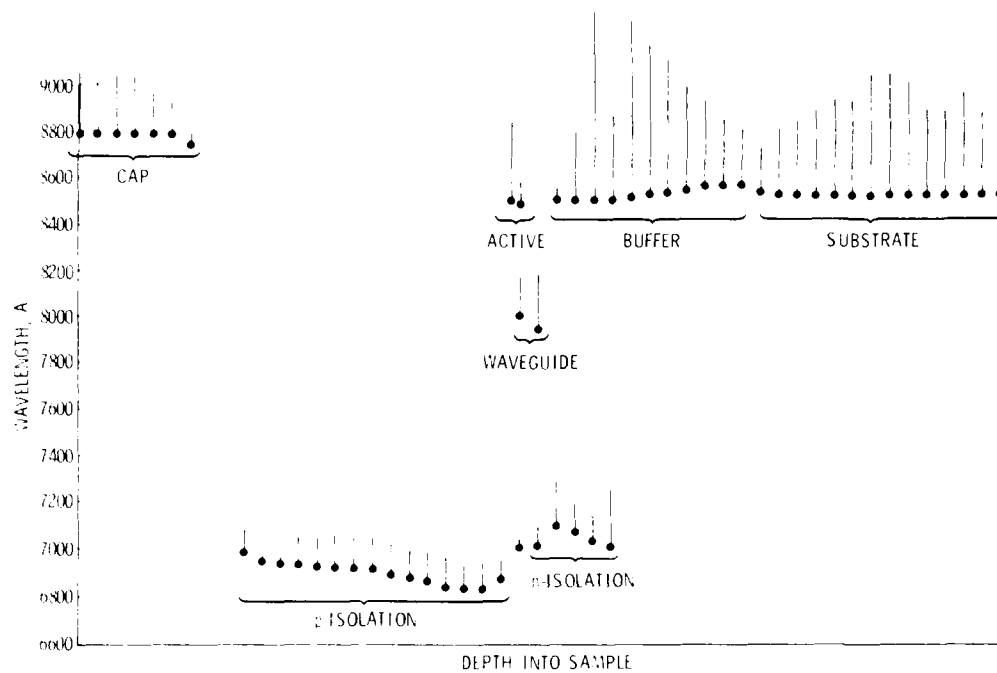


Fig. 3-6. Photoluminescence Map of Sample LDL 186. Dots indicate peak of photoluminescence; vertical lines indicate the relative intensity of the photoluminescence within the epilayer.

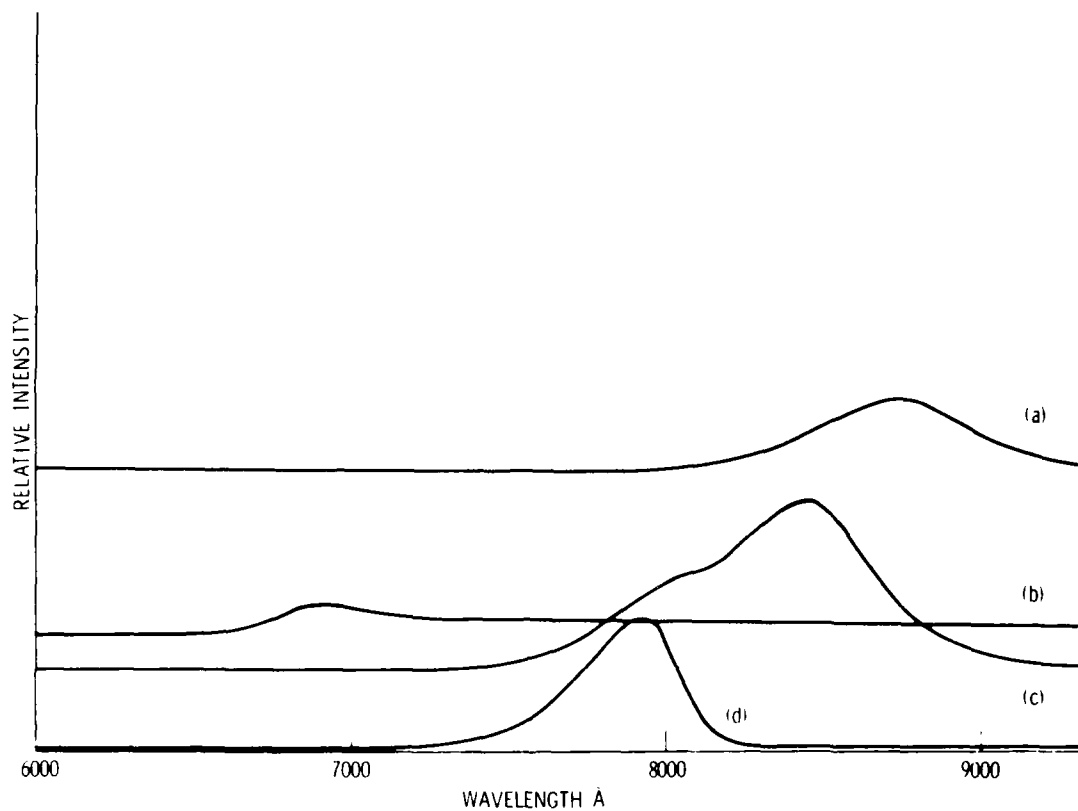


Fig. 3-7. Photoluminescence Scan With (a) Cap Layer Intact, (b) Cap Layer Removed and p-Isolation Layer Exposed, (c) p-Isolation Layer Removed and Active Layer Exposed, and (d) Active Layer Removed and Waveguide Layer Exposed.

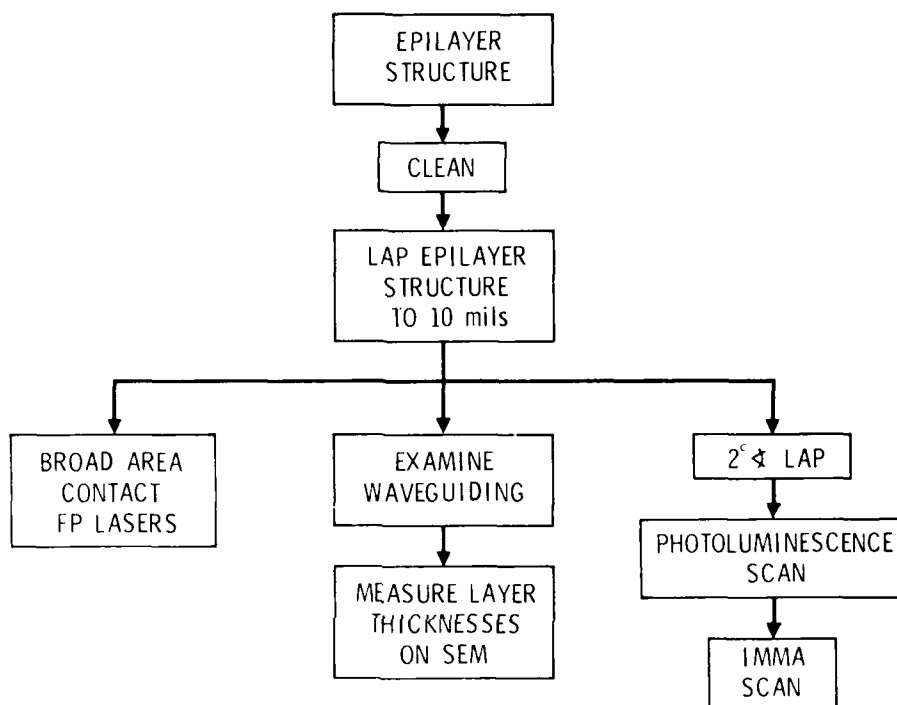


Fig. 3-8. Flow Chart for Characterizing Material

4. FABRICATION TECHNIQUES AND EXPERIMENTAL RESULTS

4.1 DBR LASERS

4.1.1 Fabrication

The development of the fabrication techniques has been described in a series of monthly progress reports. The fabrication processes that are described here are a result of refining many different approaches. A detailed, step-by-step process schedule is included in Appendix C.

Figure 4-1 is a cross section through an asymmetric, large-optical cavity DBR laser. In the DBR laser, feedback is provided by a cleave on one end and a distributed Bragg reflector (DBR) etched into the GaAlAs waveguide-SiO₂ interface on the other end of the active layer. The DBR end is sawed to eliminate end reflections.

The active-passive laser is identical to the DBR laser in construction, except that the DBR grating is eliminated and feedback is provided at both ends by cleaves. A primary reason for fabrication of the active passive device is to evaluate the coupling between the active-passive interface.

DBR lasers and active-passive lasers are fabricated in the same manner. Standard photolithographic procedures are used; 0.5-mm-wide strips of AZ1375 Shipley photoresist spaced 1 mm apart and 3 μ m thick are developed on an asymmetric large optical cavity (LOC) crystal, Fig. 4-2(a). The sizes of the crystals that have been processed range from 3 by 4 mm to 4 by 12 mm.

The photoresist stripes protect the underlying GaAs from erosion when the sample is subjected to chemical etchants and ion-beam etching. A combination of chemical and ion-beam etching is used to remove the first three layers (cap, p-isolation, and active) between the photoresist stripes. After the photoresist is removed, mesa structures composed of the original six epilayers remain separated by valleys of three epilayers (waveguide, n-isolation, and buffer).

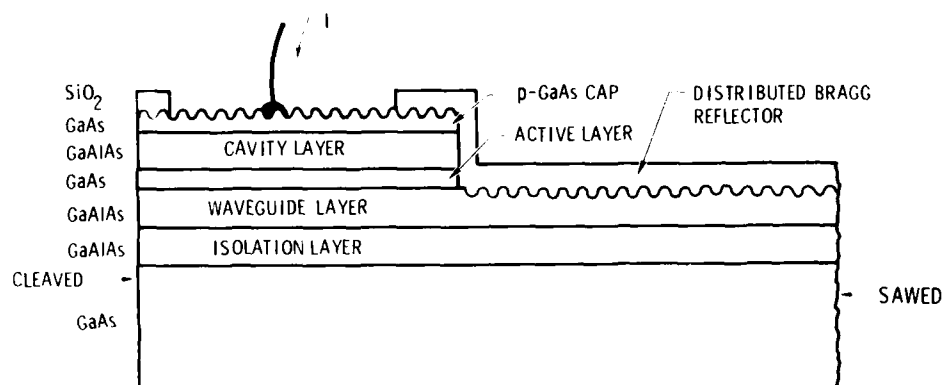


Fig. 4-1. Cross Section Through Asymmetric LOC DBR Laser

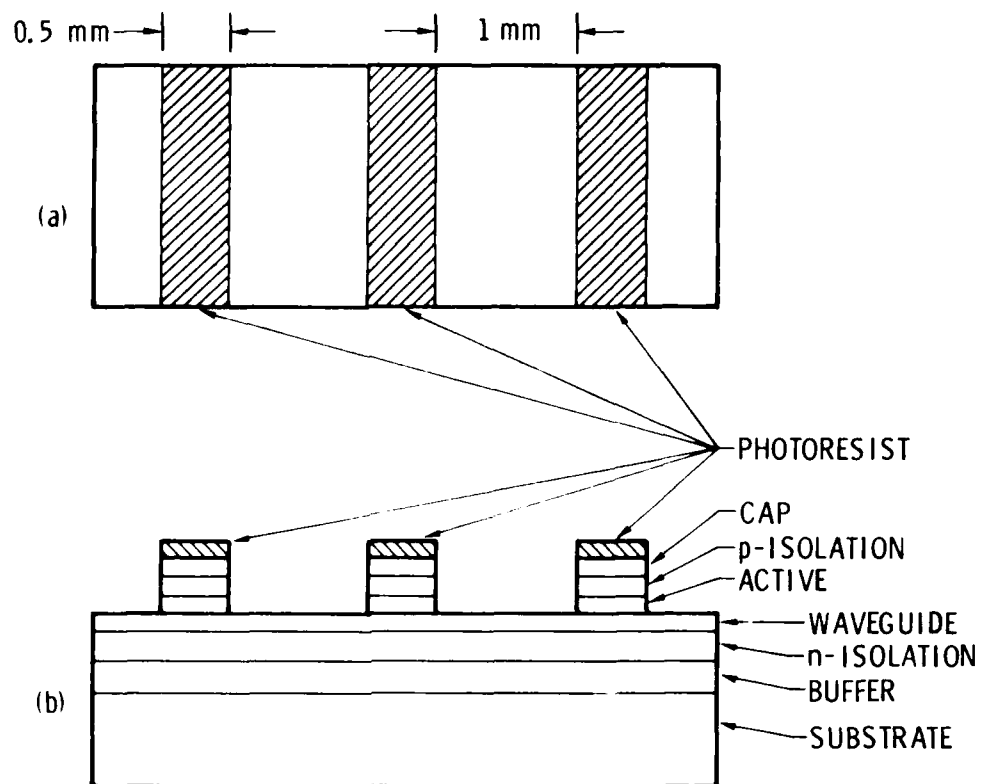


Fig. 4-2. Sample Before Processing. (a) Top view. (b) Side view after removal of three layers by ion-beam and chemical etching.

If DBR lasers are being fabricated, a holographically formed grating with a period of about 3600 Å is ion-beam etched into the top surface of the crystal. The grating structure over the waveguide layer provides third-order Bragg scattering and forms the DBR. The grating that is formed on the mesa region has no effect on the device performance. Since the procedure for fabricating gratings for DBR lasers is common to making gratings for distributed Bragg deflectors (DBD) and output couplers, a discussion of grating fabrication is given in the next section.

Once the grating is in place (for DBR lasers), a 3000-Å-thick layer of SiO_2 is deposited over the entire surface of the sample. A 1.6- μm -thick layer of Shipley AZ1350J photoresist is deposited over the oxide, and a series of windows (25 by 450 μm) spaced 250 μm apart are developed through the photoresist down to the oxide layer on the mesa regions. The oxide layer exposed by the windows is etched away reactively in a plasma gas of CF_4 . Windows exist through the photoresist and oxide layer down to the GaAs cap layer on the mesas. A layer of platinum and gold contacts can now be electroplated to the GaAs in the windows through the photoresist and the oxide layer (Fig. 4-3). The photoresist and oxide layers provide a mask to confine the plating to the conductive GaAs stripe and also provide sidewall confinement of the plated material. The back side of the sample is also electroplated to form the bottom contact. A detailed explanation of the plating procedure is given in Appendix D. After cleaning the sample, the crystal is cut into individual lasers. The bottom side of the laser is soldered to a TO-18 transistor header, and a gold wire is ball bonded to the top contact and to a header post. A complete DBR laser is shown in Fig. 4-4.

Preliminary tests of the laser diodes include checking the I-V characteristics on a transistor curve tracer and observing the luminescence through a hand-held infrared viewer.

4.1.2 Experimental Results for DBR Lasers

The mode spectrum, total power, light current characteristics and beam divergence were measured for the fabricated DBR lasers. Figure 4-5 is a block diagram of the laser test setup. A typical spectrum of a DBR laser is shown

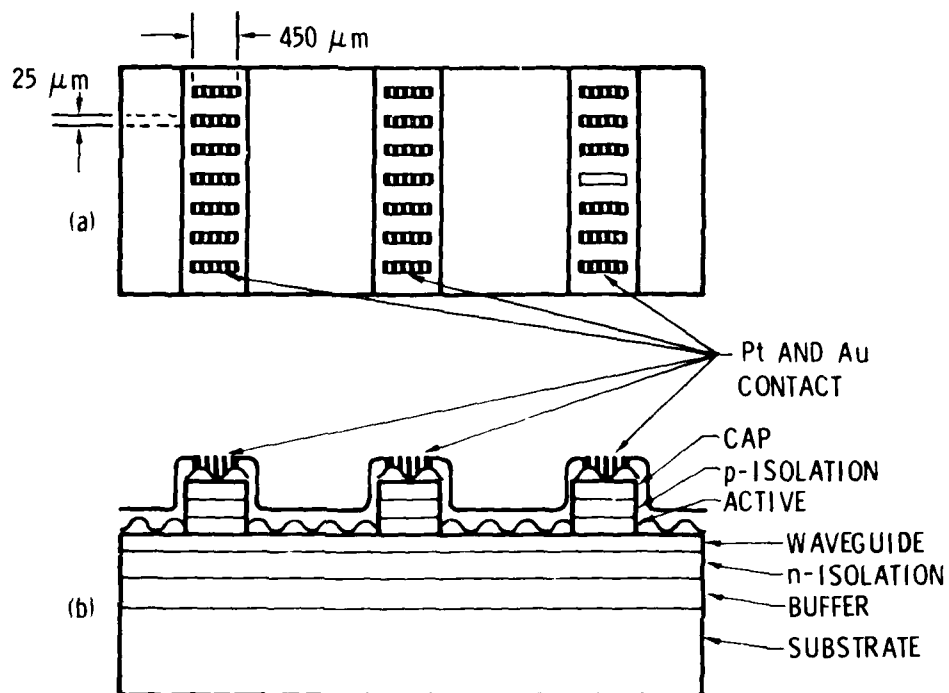


Fig. 4-3. Sample After Processing, Ready to be Cleaved into Individual DBR Lasers. (a) Top view. (b) Side view.

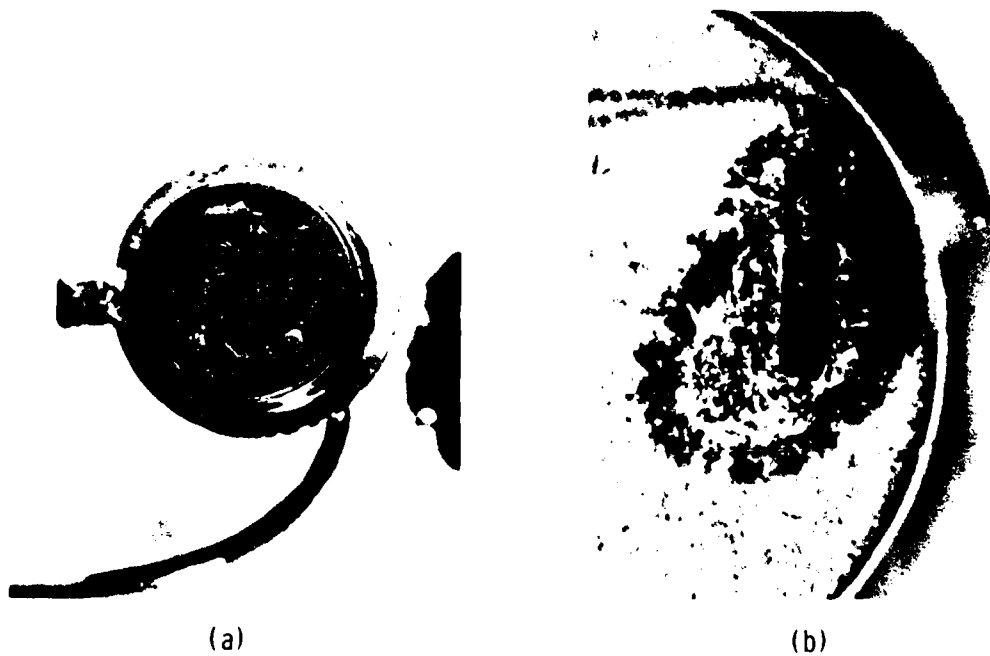


Fig. 4-4. DBR Laser. (a) Mounted on TO-18 transistor header. (b) Close-up view.

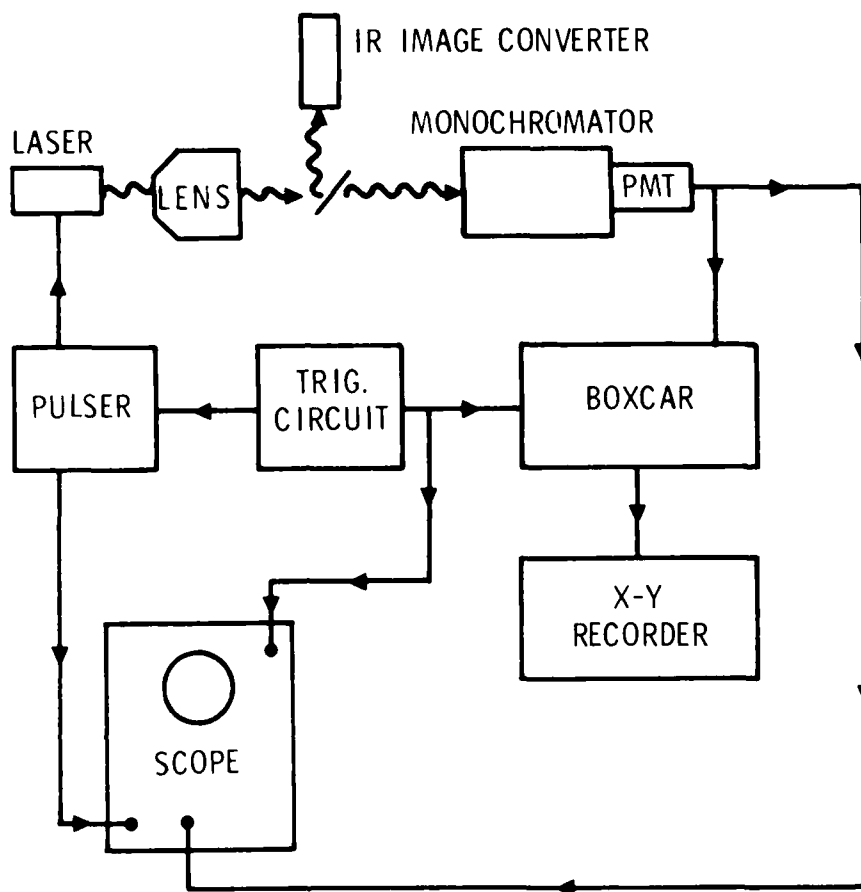


Fig. 4-5. Experimental Setup for Laser Spectrum Measurements

in Fig. 4-6. In order to verify that the laser action occurred from the grating and not from spurious reflections, several tests were performed.

It was observed that the DBR spectrum was a single mode. Comparable spectra for Fabry-Perot lasers from the same material were multimode (Fig. 4-7). In addition, a DBR laser, which operated at room temperature, was cooled to liquid nitrogen temperature, and laser action ceased, since the reflectivity of the grating was no longer at the frequency of the fluorescence. This is in contrast to Fabry-Perot lasers whose frequency shifts with temperature.

In some of the DBR lasers, two lines occurred (Fig. 4-8) because the waveguide was sufficiently thick that not only the lowest even mode but also the lowest odd mode could propagate.

An example of a two-mode DBR laser is shown in Fig. 4-9. As shown in Fig. 4-10, a grating-wave vector K ($K \equiv 2\pi/\Lambda$) can cause a DBR laser to oscillate in more than one transverse mode, depending upon the spacing of the waveguide modes to the width $\Delta\lambda$ of the gain profile and the relative strength of the intermode and intramode coupling coefficients. A graphical solution for the DBR lasing spectra that accounts for the refractive index variation with wavelength is indicated in Fig. 4-11. The graphical solution compares favorably with the 40-Å spacing between modes observed experimentally.

The linewidths just above threshold were typically 1 Å. DBR laser G8, (Fig. 4-6) has a linewidth of 1.1 Å, and DBR laser G9 (Fig. 4-8) has a width of 1.6 Å. The apparent linewidth broadened slightly with pumping (Fig. 4-12) in which DBR laser G5 is pumped at three times threshold. The line had broadened to about 3 Å, but it was observed on the oscilloscope that the frequency changed during the 100-nsec input pulse. The broadening is believed to be a chirp caused by heating in the junction. Such effects have been observed in Fabry-Perot diode lasers.

Diode G9 had a complicated behavior, since the two frequencies corresponding to two guided modes occurred at high pumping rates. It was observed that at low excitation levels, the shorter wavelength was the strongest peak, and the longer wavelength occurred only during the initial portion of the

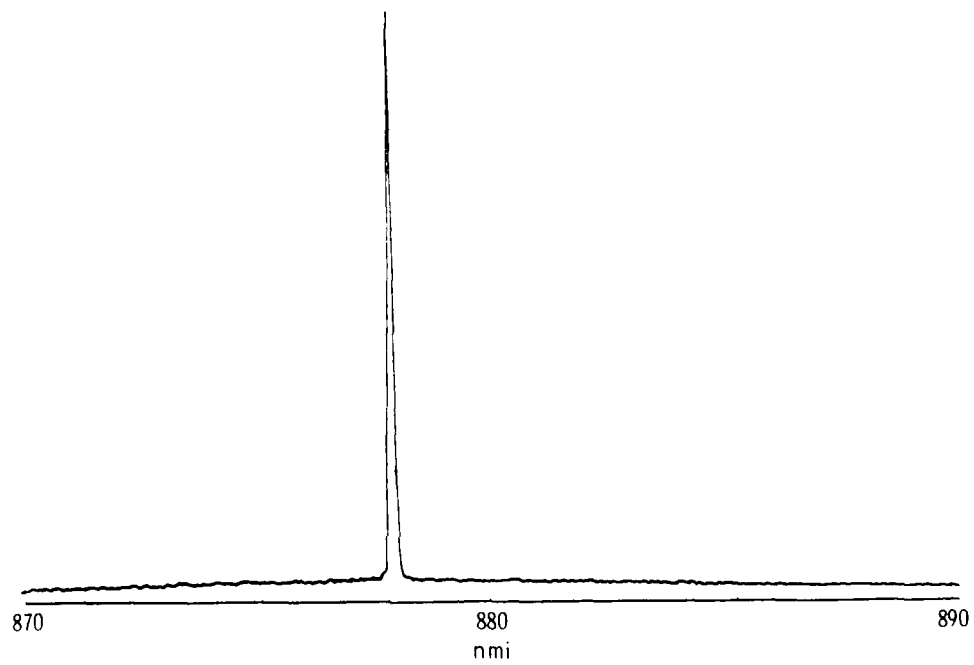


Fig. 4-6. Spectrum of Typical DBR Laser

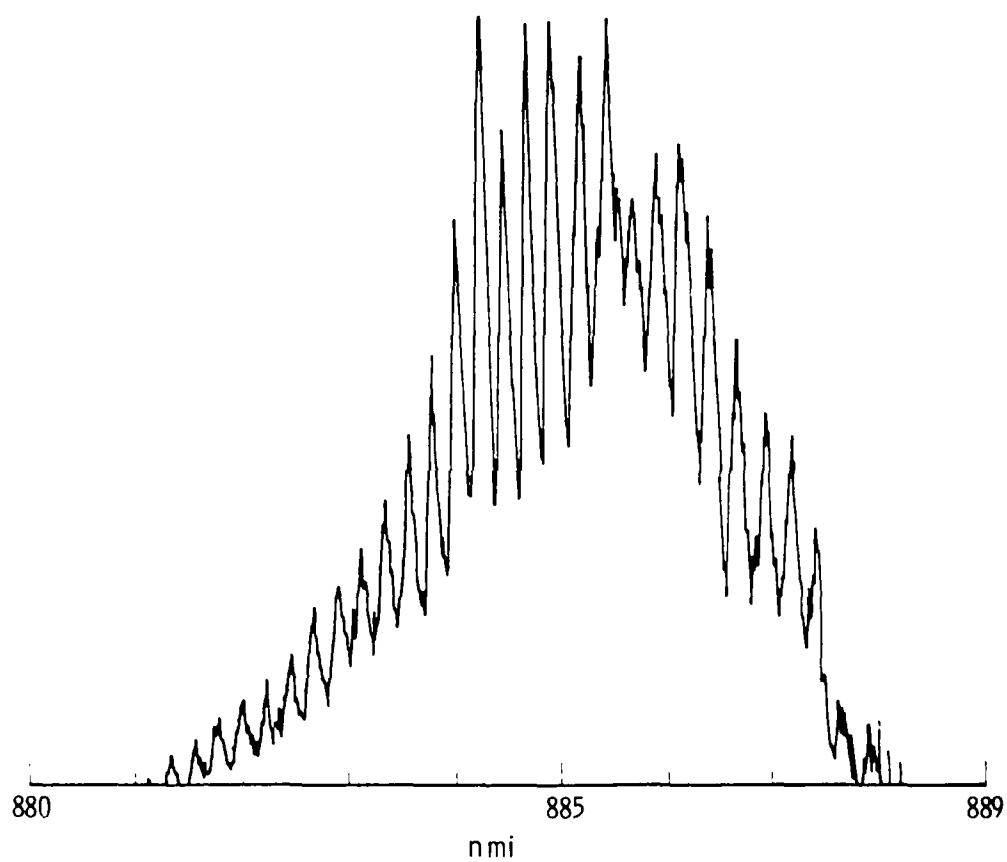


Fig. 4-7. Spectrum of FP Laser Fabricated from Same Material Used in Fig. 4-6

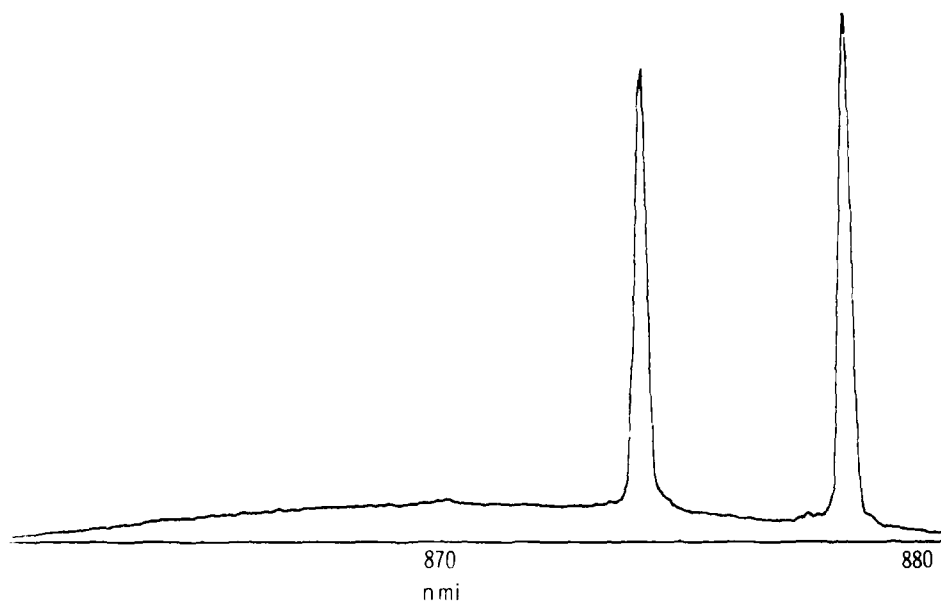


Fig. 4-8. Spectrum of DBR Laser That Supports Two Waveguide Modes and Has Two Oscillation Frequencies

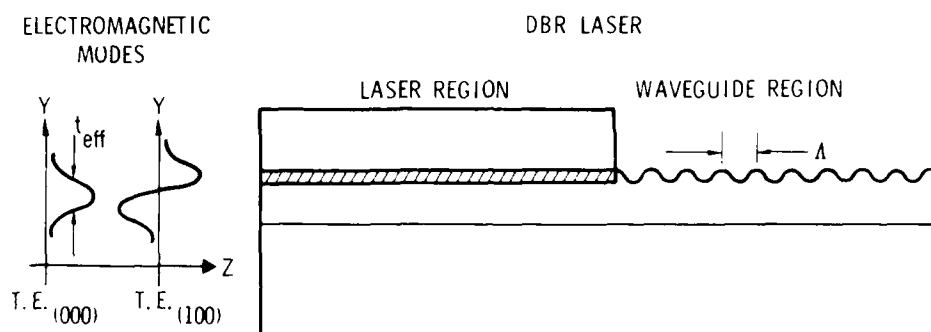


Fig. 4-9. Two-Mode DBR Laser

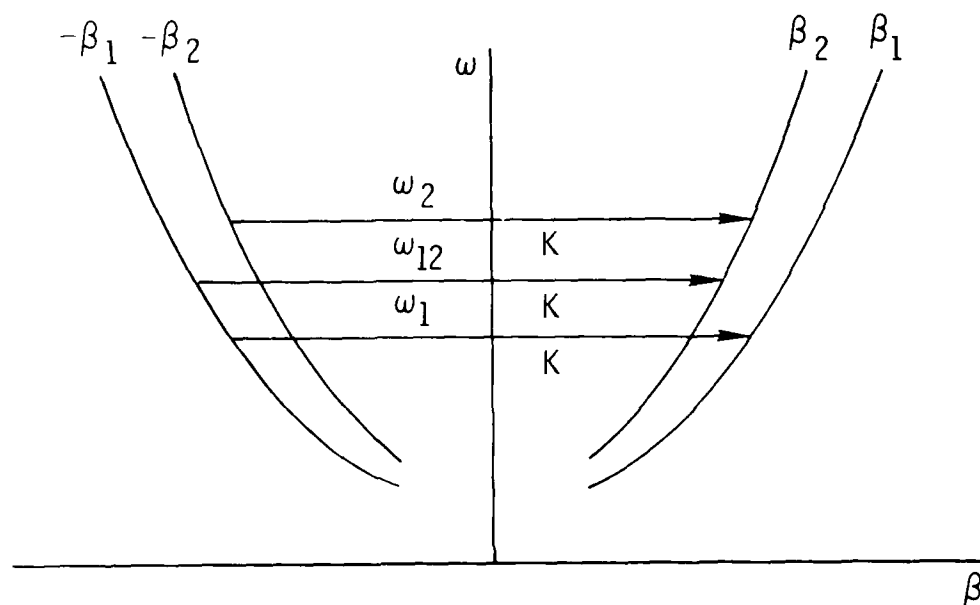


Fig. 4-10. ω - β Diagram of Three Scattering Processes. The grating wave vector $K = 2\pi/\Lambda$ has same length for each process. Backward scattering between modes 1-1, 1-2, and 2-2 occurs at frequencies ω_1 , ω_{12} , and ω_2 , respectively.

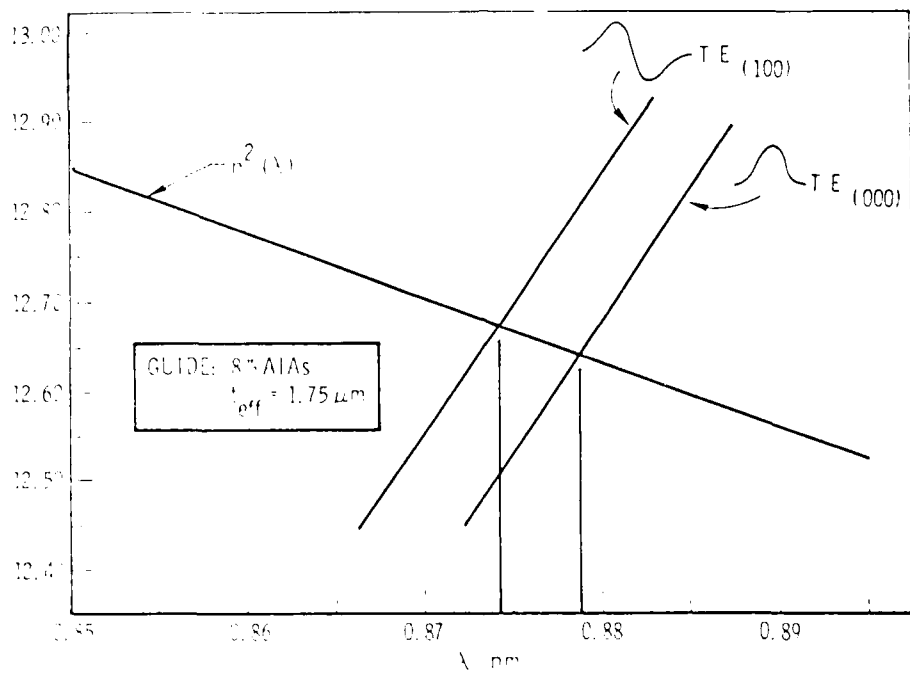


Fig. 4-11. Oscillation Wavelengths of DBR Laser with Two Waveguide Modes

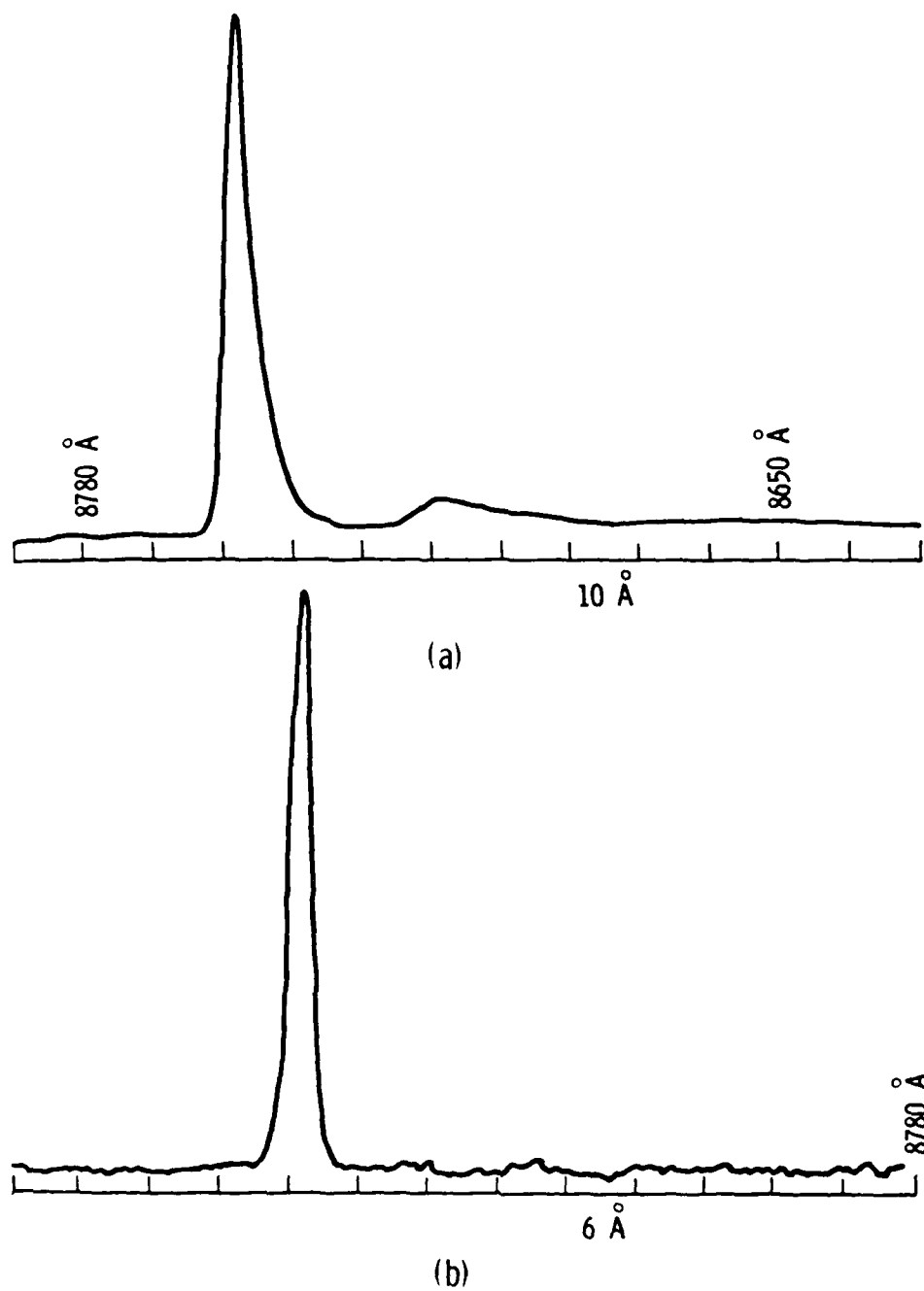


Fig. 4-12. DBR Laser Spectra. (a) Diode G5 at three times threshold current. (b) Diode G9 just above threshold.

pulse. Evidently, heating caused the resonance condition to change. Near the end of the pulse, the shorter wavelength had a lower threshold and was the only frequency above threshold. These data demonstrate that, even when a grating is used, it is possible to get several wavelengths oscillating, and not necessarily simultaneously.

The complexity of device G9 can be seen from the light-current curve (Fig. 4-13), which has several kinks. The DBR laser causes only one or two frequencies to oscillate, but does not necessarily improve light-current characteristics, in relation to Fabry-Perot lasers.

Since kinks seem to be related to the filamentary structure of lasers,⁴ and since we were interested in beam quality, in order to perform beam expansion, we made a careful study of the diffraction qualities of the light emitted from the DBR lasers. Depending on the device used, we were able to observe diffraction-limited operation just above threshold. This is demonstrated by studying the divergence of sample G9, right above threshold. Near-field patterns were observed both from the cleave and the grating face (Fig. 4-14). In addition, the in-plane beam divergence was measured coming out of the cleave. This was accomplished by monitoring the spot size as a function of distance from the cleave. The data are shown in Fig. 4-15.

The data are analyzed by comparing the measured divergence with that expected for a Gaussian beam of the width determined from the near field intensity profiles (Fig. 4-14).

The angular divergence of a Gaussian beam is

$$\theta_0 = \lambda / \pi \omega_0 \quad (4-1)$$

where θ_0 is the half-angle, and ω_0 is the half width of the beam at $1/e^2$ in intensity. Redefining the quantities in terms of full width half maximum,

$$\theta = \frac{\lambda}{0.72 \pi \omega} \quad (4-2)$$

⁴N. Chinone, J. Appl. Phys. 48, 3237 (1977).

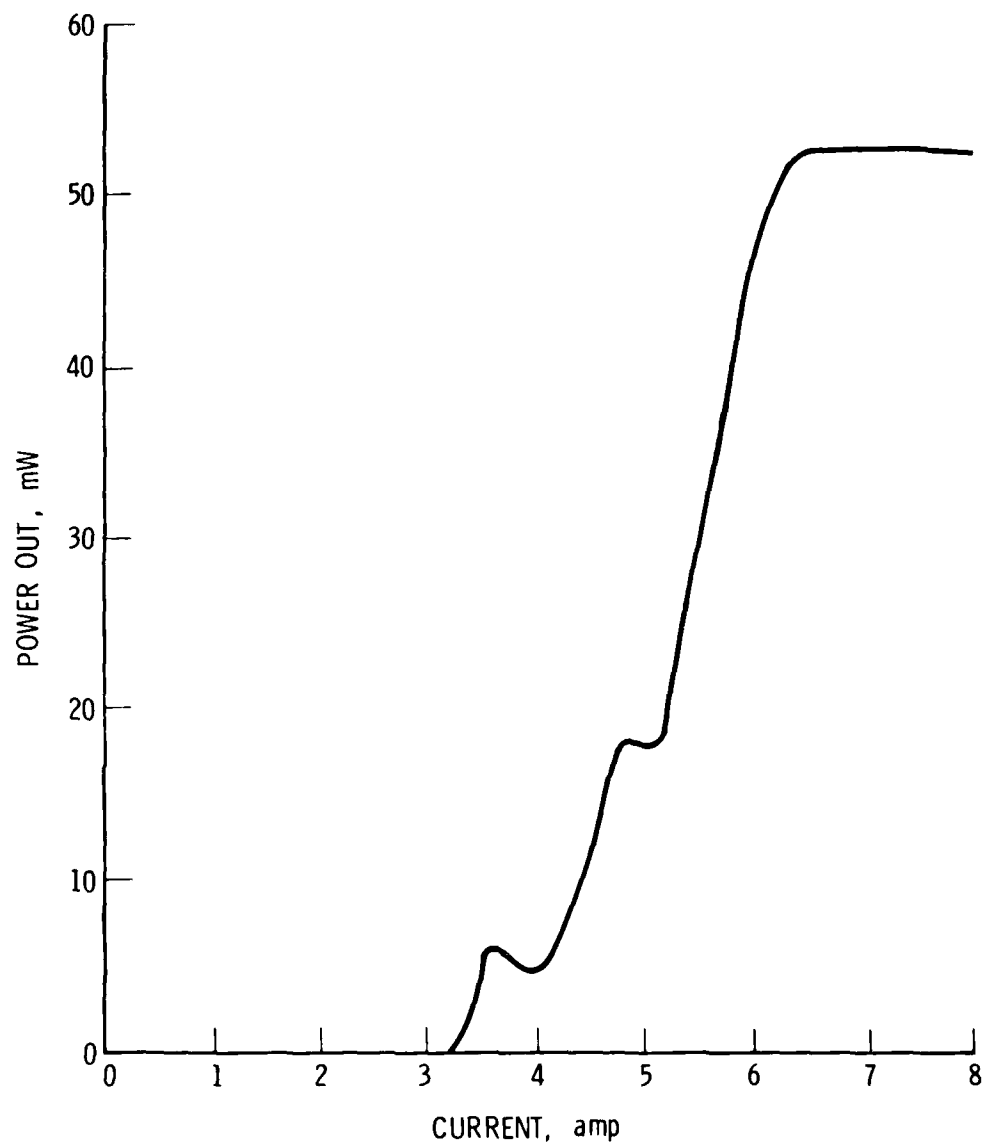


Fig. 4-13. Light-Current Characteristics for Diode G9

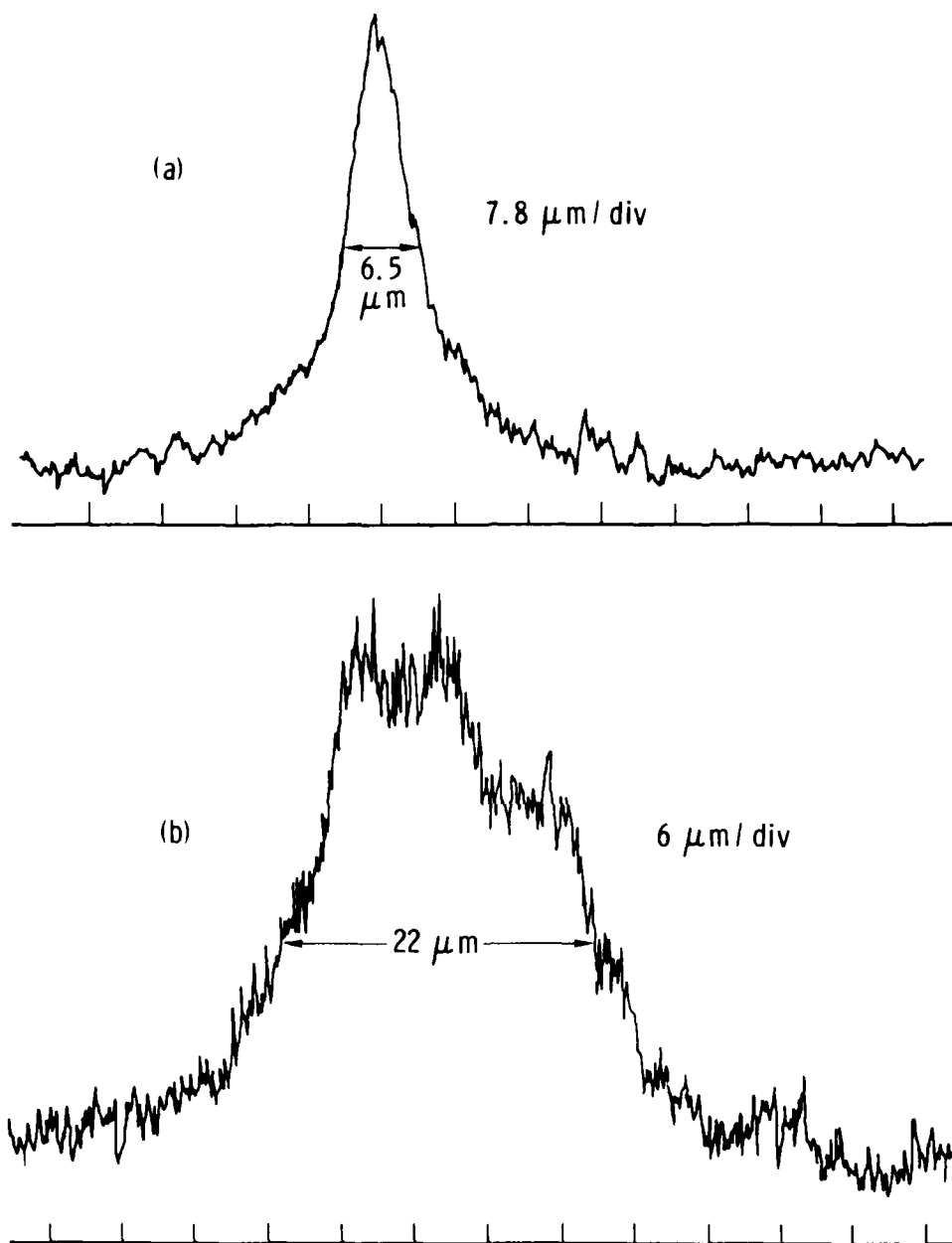


Fig. 4-14. Near-Field Profiles for DBR Laser with Diode G9 at Threshold.
(a) Cleaved face. (b) Grating face.

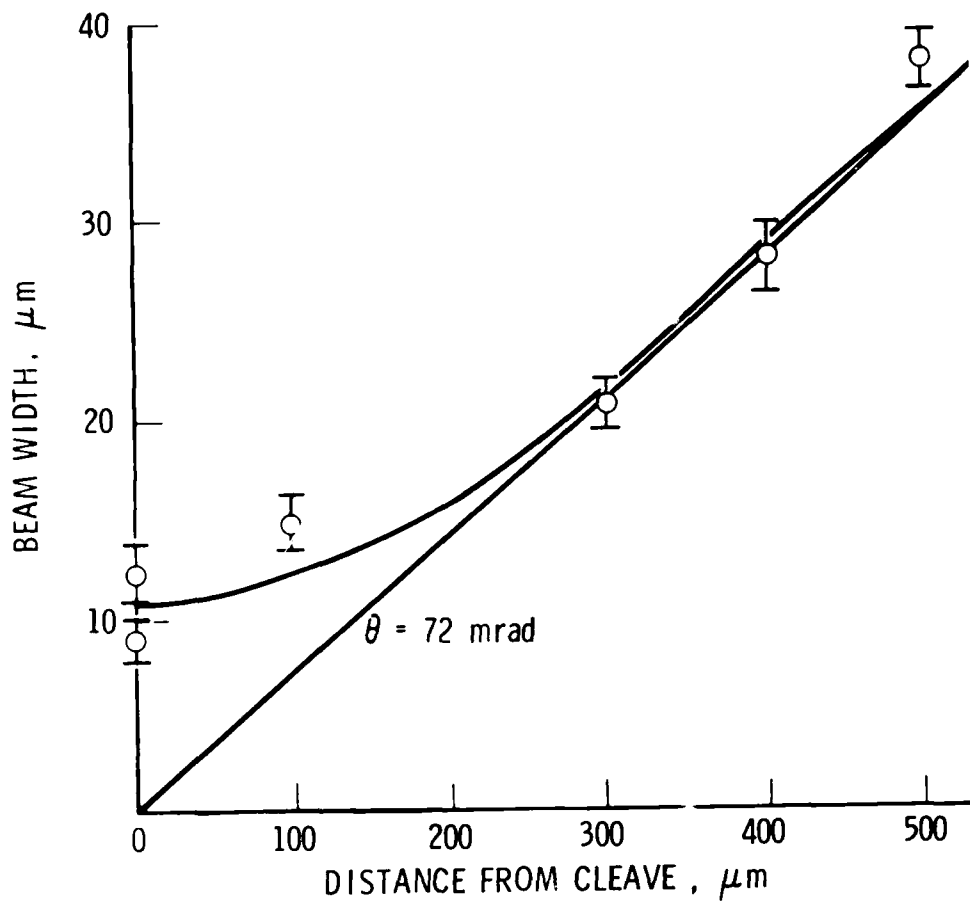


Fig. 4-15. In-Plane Beam Width Versus Distance from Exit Face (as measured on a television monitor). Far-field divergence angle is 72 mrad.

The filament measured in the near field had an apparent width of $6.4\text{ }\mu\text{m}$ (correction has not been made for resolution of the microscope objective used in this measurement). The far-field beam divergence out the cleave was 0.072 rad , which corresponds to the diffraction expected from a filament of width $5.4\text{ }\mu\text{m}$. This agrees well with the measured filament width and supports the assumption that this laser operated in a single spatial mode.

The laser output from the cleaved face was observed to have a near-field profile that was a single filament $22\text{ }\mu\text{m}$ wide. This profile is the beam that has diffracted from the $5.4\text{-}\mu\text{m}$ filament in the laser region as a result of a 1-mm grating (Fig. 4-16). If the filament is assumed to extend the length of the active region of the laser diode and begins to expand when it enters the grating, the diffraction should occur for a distance of 1 mm , at an angle given by the far-field divergence angle divided by the index of refraction of the medium (0.02 rad). This divergence would cause the output of the grating to have a width of $20\text{ }\mu\text{m}$, which compares favorably with the measured filament width of $22\text{ }\mu\text{m}$.

For completeness, out-of-plane beam divergence was measured also. It was observed that the frequency corresponding to the higher order waveguide mode caused a double-humped far-field pattern from the cleave. The divergence was greater than 0.48 rad and could not be measured since it was limited by the aperture of the lens that was used. The other frequency was a lowest order waveguide mode and had a beam divergence of 0.3 rad . This supports the assumption discussed earlier that the two frequencies are caused by the different modes occurring in the laser region.

Other diodes did not necessarily show in-place diffraction-limited behavior. The near-field profiles of diode G5 are shown in Fig. 4-17. Although the apparent near-field profile was $15\text{ }\mu\text{m}$ wide, the beam divergence was 0.165 rad , corresponding to a filament size of $2.4\text{ }\mu\text{m}$. In other words, the diode had a highly filamentary character, which caused a great deal of beam divergence. This fact was made clear by looking at the profile out of the grating. The output had several filaments and an overall width of almost $100\text{ }\mu\text{m}$.

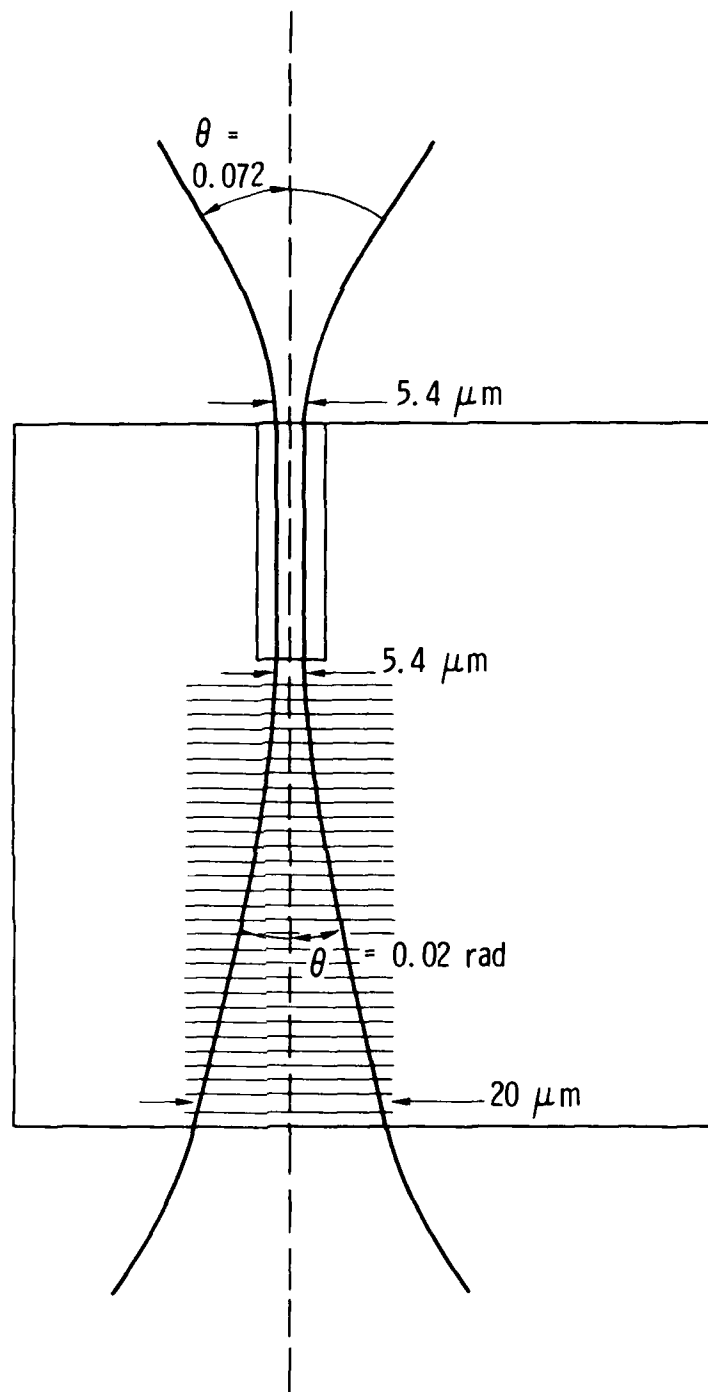


Fig. 4-16. Geometry for In-Plane Divergence of DBR Laser

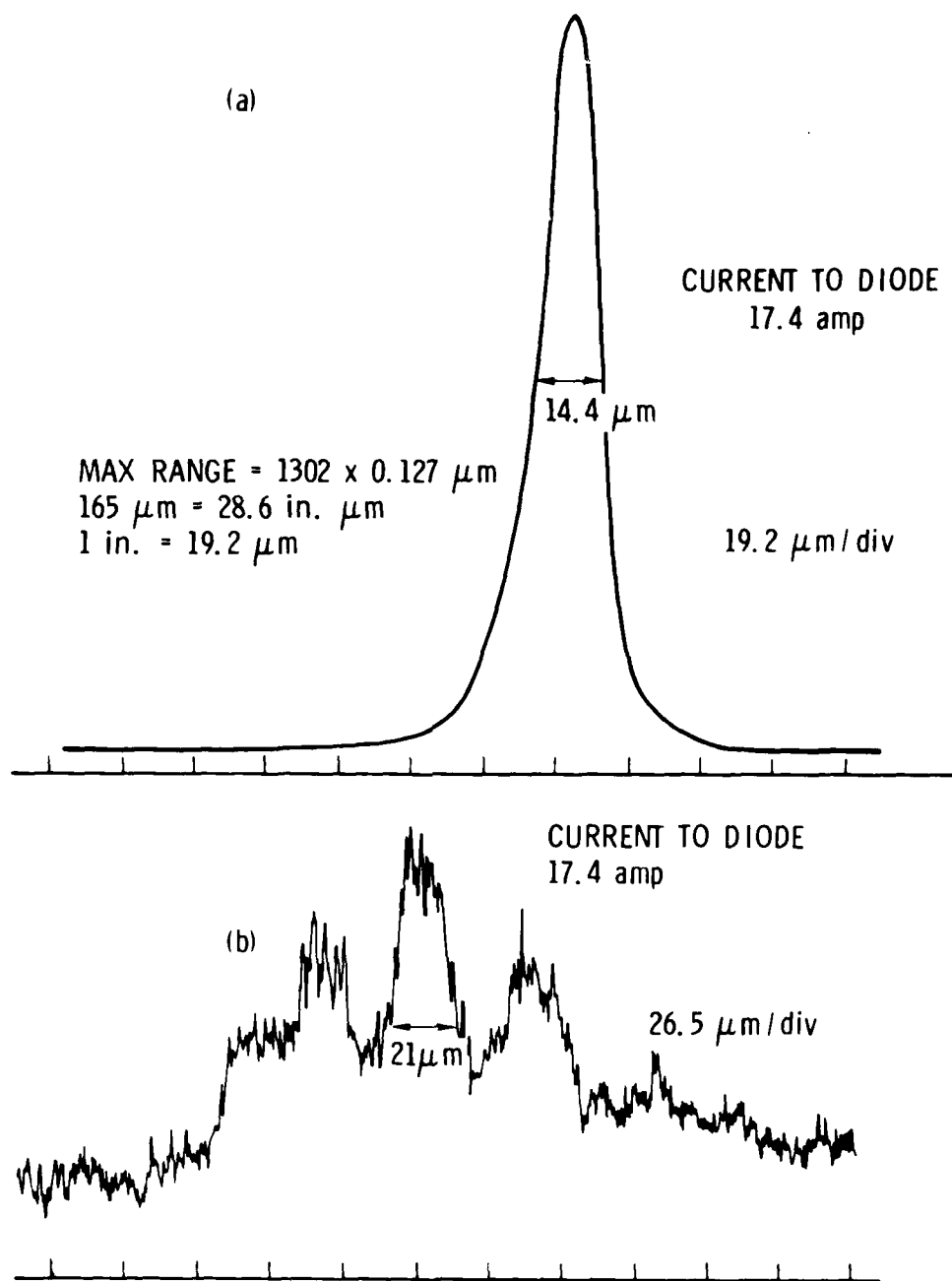


Fig. 4-17. Near-Field Profiles for DBR Laser with Diode G5. (a) Cleaved face. (b) Grating face.

Additional measurements were made of the front-to-rear power ratio of DBR lasers of differing lengths to determine the coupling coefficient of the grating and to check for its reproducibility. Two devices were compared in detail; the data are shown in Table 4-1.

According to the theory, a retroreflector of length L on resonance has the following behavior for transmission:

$$T = \frac{1}{\cosh^2 KL} \quad (4-3)$$

and reflection:

$$R = \frac{\sinh^2 KL}{\cosh^2 KL} \quad (4-4)$$

When $KL \gg 1$,

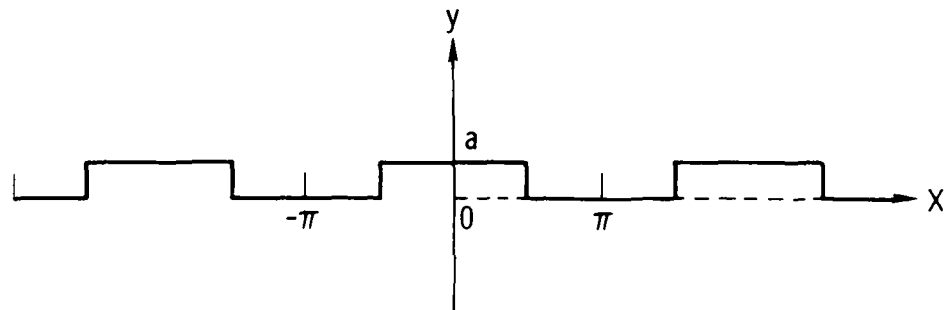
$$T = 4e^{-2KL}, \quad R = 1 - T \quad (4-5)$$

The coupling coefficient was determined from Eq. (4-5) with the assumption that the front-to-back power ratio will be the same as the ratio of the transmission of the grating to the transmission of the GaAs cleave on the front output face (85%). The results give an average coupling coefficient of $K = 0.0036 \mu\text{m}^{-1}$.

The theoretical expression for the coupling coefficient of a grating is given for square teeth in Appendix B. The experimental grating looked more like triangular teeth than square teeth, however. The comparison between square and triangular shapes may be made by comparing the Fourier transforms for the third-order coefficients for square and triangular shapes. Using the calculations shown in Fig. 4-18, we see that the polarization induced by a triangular grating will be two-thirds that induced by the step index. Thus, we expect the grating coupling coefficient to be

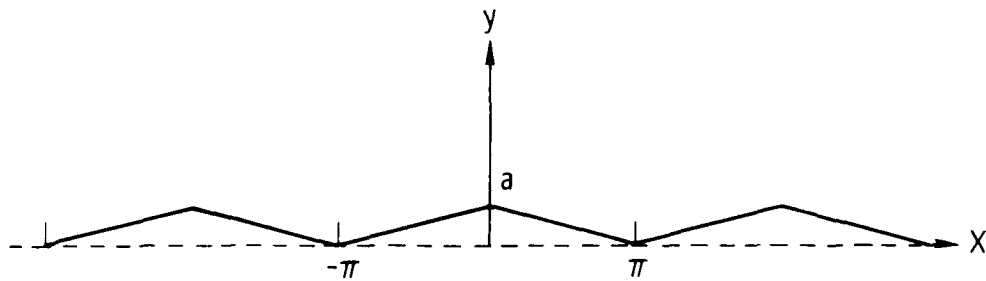
Table 4-1. Data Used to Determine Coupling Coefficient of Gratings in DBR Lasers

	G9	G5
Power-Out Grating, mW	1	0.5
Power-Out Cleave, mW	30	10
Power Ratio (grating to cleave), T	0.03	0.05
$\ln T/4$	-5.3	-4.4
Grating Length, μm	1000	464
K	0.0026	0.0047
L_g , μm	192	106



$$F = \int_{-\pi}^{\pi} y(x) \cos 3x \, dx = a \int_{-\pi/2}^{\pi/2} \cos 3x \, dx = \frac{2a}{3}$$

(a)



$$F = \int y(x) \cos 3x \, dx = -2a \int_0^{\pi} x \cos 3x \, dx = \frac{4a}{9}$$

(b)

Fig. 4-18. Third Harmonic Calculation for Square and Triangular-Shaped Grating Teeth

$$K = \frac{4\pi^2(n^2-1)}{9m\lambda n} \left[\frac{a}{t_{\text{eff}}} \right]^3 1 + \frac{3\lambda/a}{2\pi(n^2-1)} + \frac{3(\lambda/a)^2}{n^2-1} \quad (4-6)$$

where n is the refractive index of the guide and where we have taken the result of Yariv,⁵ multiplied by two-thirds, and used t_{eff} instead of t for guides that are not far from cutoff.

From SEM photographs of the grating, we estimate $a = \Lambda/3$, $t = 1.54 \mu\text{m}$, and $\Lambda = 0.36$. The grating was used in third order, and the refractive index of GaAs at $0.88 \mu\text{m}$ is 3.6. These numbers give the theoretically expected coupling coefficient of $K = 0.0044 \mu\text{m}^{-1}$. In order to calculate this number, the effective guide width was required. This was determined by solving the eigenvalue equation for the waveguide to determine the exponential profile outside of the guide and to calculate $t_{\text{eff}} = t + 1/\gamma$. For the DBR lasers, the V parameter for the waveguide was $\Delta\epsilon k_0^2 d^2 = 146$, resulting in two modes, given by the following eigenvalue equations:⁵

$$\tan u = \frac{146}{u^2} - 1$$

and

$$\tan u = - \left(\frac{146}{u^2} - 1 \right)^{-1/2} \quad (4-7)$$

The solutions are $kd = 1.7$ and 3.4 , which yield $\gamma d = i2$, with an effective thickness of $1.62 \mu\text{m}$. This is the value used in Eq. (4-6) to determine the theoretical coupling coefficient.

The excellent agreement between theory and experiment permits us to predict behavior for other waveguides. We are presently in the process of fabricating devices from material with a waveguide thickness of $0.6 \mu\text{m}$. These samples should yield devices with coupling coefficients as much as eight times larger.

⁵A. Yariv, Quantum Electronics, Second ed., Wiley, New York, 1975.

4.2 GRATING FABRICATION BY HOLOGRAPHIC EXPOSURE

Holographic exposure is accomplished by exposing the substrate to two interfering argon-ion laser beams. The argon laser beams are spatially filtered, expanded, and collimated prior to being split. The split beams are interfered at an angle θ , necessary for a given periodicity of grating. The relationship between θ , the grating periodicity and laser wavelength, is

$$\Lambda = \frac{\lambda}{2 \sin \theta} \quad (4-8)$$

where Λ is the grating periodicity, λ is the laser wavelength (0.4570 μm), and θ is the angle of interference. In Fig. 4-19, the optical system for holographic exposure is shown.

In order to achieve precise alignment of the substrate with respect to the two interfering argon laser beams (and therefore accurate control of the grating orientation), an HeNe laser is used. The HeNe laser, aligned level with respect to the argon beam, is reflected off a (110) crystal plane of the substrate and back onto the front laser window, ensuring that the (100) crystal plane is normal to the interfering argon beams and thereby accurately orienting the grating.

The substrate is mounted on a precision coaxial rotational stage accurate to 0.01 deg of arc so that once the substrate has been oriented to the normal it can be rotated to the required angle of grating orientation. The substrate is then exposed (~ 30 sec at a beam intensity of 10 mW/cm^2) and developed. The sample is now ready for ion-milling replication of the photoresist grating into the substrate. A rotary ion-milling technique is used with a beam current of 0.5 mA/cm^2 and an acceleration voltage of 500 Vdc.

A grating with a period of $\sim 3600 \text{ \AA}$ fabricated by this technique is illustrated in Fig. 4-20. Although the techniques for grating fabrication were well developed before the beginning of the contract once etched structures were fabricated, it was found that the photoresist deposition techniques required for grating exposure were not sufficiently smooth. A new technique

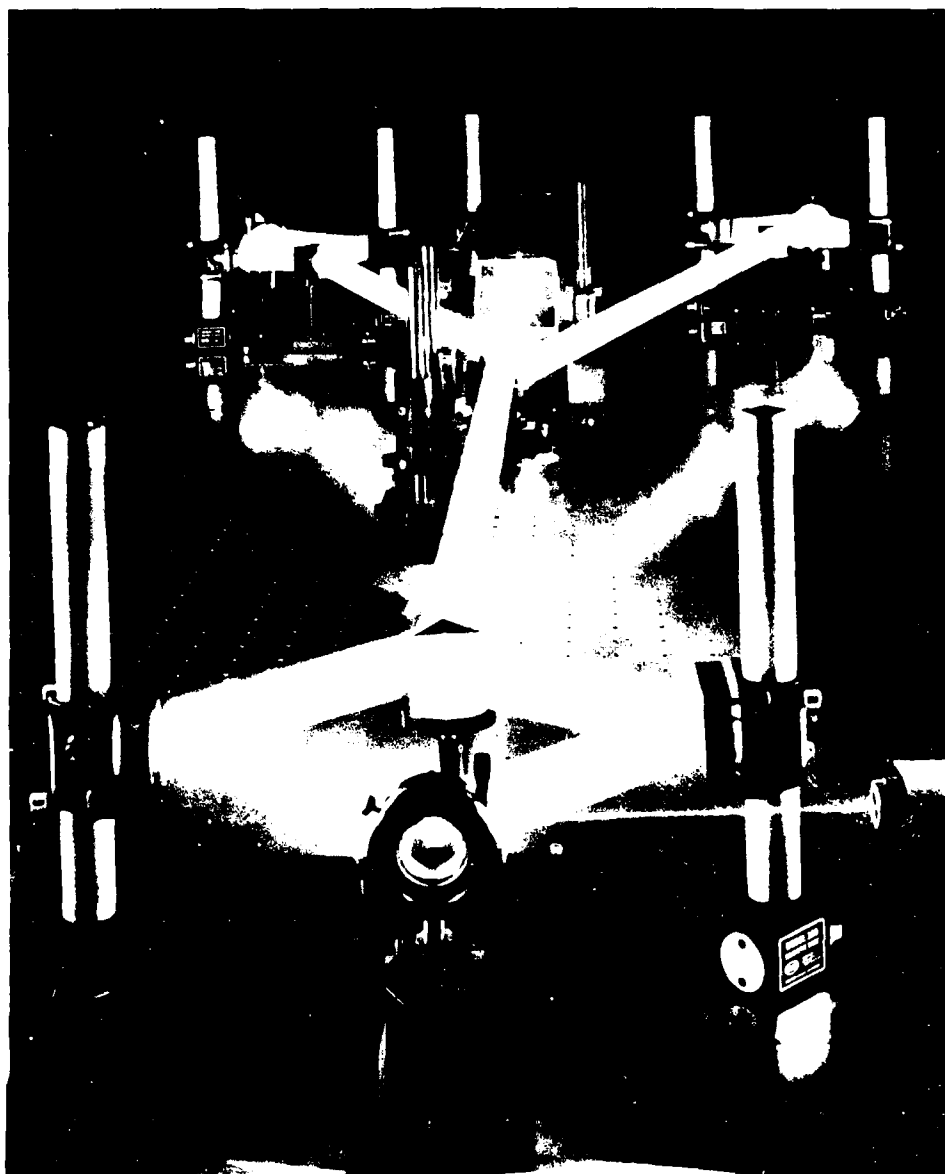


Fig. 4-19. Laboratory Setup for Exposure of Three Gratings for High-Brightness Laser



Fig. 4-20. Cross Section Through Ion-Milled DBR Reflector.
Grating periodicity is 3600 Å.

was therefore developed in which the application of thin films of photoresist for grating fabrication was accomplished by a technique other than centrifugal spin coat application. The spin-coat technique was acceptable for a flat sample with no changes in surface topography. Once surface steps were introduced by the etch techniques, bordering effects occurred, which originated from the bottom edge of the mesa, anywhere from 5 μm to 0.3 or 0.4 mm, depending on photoresist viscosities and speed of spinning. Studies were therefore initiated to develop alternative techniques of photoresist deposition.

Several techniques have been used to apply photoresist films,⁶ such as dip coating, which is simply dipping the substrate into the photoresist solution and drawing it out at a fixed rate for a selected thickness. By means of this technique layers are produced whose thicknesses vary from 5 to 50 μm . Another technique is roller coating, which involves the application of photoresist by the contact of a photoresist impregnated roller against the substrate. By means of this technique layers are produced whose thicknesses vary from 25 to 300 μm . One final technique is a spray coat application, which is simply passing the substrate through a heavy spray of photoresist at a fixed rate. Typical layer thicknesses for the technique are 3 to 25 μm .

All of the aforementioned techniques result in somewhat thick, films, ranging from a thickness of 3 μm for the spray coating technique to 0.4 mm for the roller technique. The film thickness necessary for holographic exposures of gratings is $\sim 0.15 \mu\text{m}$, a factor of 20 thinner than obtainable with the spray coating technique. However, since the spray coating technique proved to be the most promising, work commenced to refine and modify the technique to facilitate films as thin as 0.1 μm .

The problems to be addressed were the proper atomization of the photoresist and the ability to precisely control the time that the substrate was

⁶W.S. DeForest, Photoresists: Materials and Processes, McGraw-Hill, New York, 1975.

exposed to the spray. The first problem was solved by determining the optimum viscosity of the photoresist; the selected viscosity in simple measures was 4:1 Shipley Thinner to Shipley to AZ1350 B, respectively.

Two other important factors in the atomization process are the proper air to photoresist mixture, which was ~100:1, and the supply pressure, which was ~80 psi.

The second problem was controlling the amount of deposition time for a given film thickness. The standard technique is the movement of the substrate in front of the spray. This technique is unacceptable because of the mechanics involved with moving the substrate at a high rate of speed in order to obtain a thin film. Two techniques were evaluated to accomplish a short deposition time, one of which was the switching of the air pressure used to propel the photoresist. This technique proved to be too slow because of residual pressure in the system after the supply pressure had been switched off. The other technique, which was successful, was an electromechanical shutter placed between the spray and the substrate.

Because of a lack of such a device, one had to be designed and built. The shutter had to be capable of actuation times of less than 30 msec, while being subjected to a flow at ~80 psi. A standard electromechanical shutter actuator was used to switch a relay supplying the power to the shutter.

One last parameter in the deposition process was the distance between the spray source and substrate. This variable was solved by several test depositions. The optimum distance for the most uniform coverage in this system was 11 cm.

This photoresist deposition system proved successful in the uniform application of thin films of photoresist on large nonflat surfaces for the purpose of high-resolution photolithography and holography.

In parallel with the effort to fabricate DBR lasers, we developed the techniques for multiple-grating exposures that would be needed for fabrication of the high-brightness laser.

Device integration on a common substrate generates severe placement and orientation tolerances on each of the individual gratings. In addition, each grating must bear a different periodicity, thus requiring multiple holographic exposure and development steps. As a result of these constraints, we must have the ability to control the placement, orientation, periodicity, and the amount of area to be covered by each individual device grating. The three primary devices and their relative area, placement, and orientation on the common substrate are shown in Fig. 4-21.

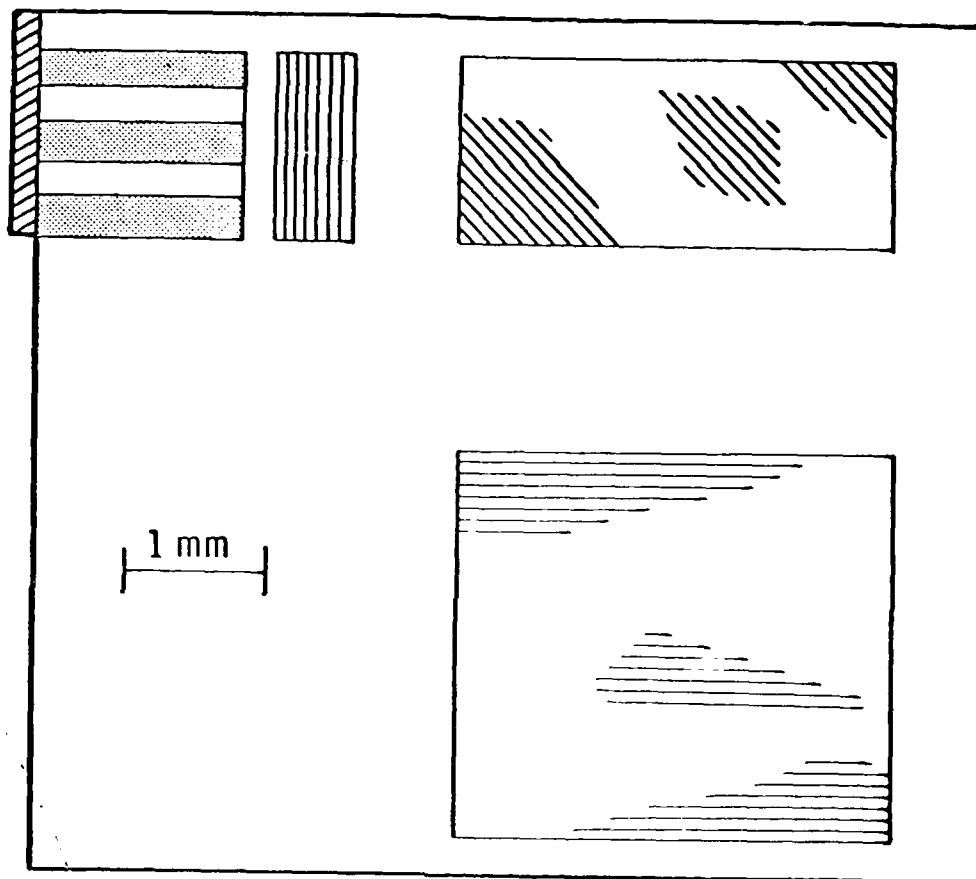
A very important process in the multiple-placement procedure is multiple masking for control of the area and placement of the gratings. This is photolithographically facilitated with the use of a novel photoresist mask. The first step in the photolithographic process is the application of the primary photoresist layer ($\sim 0.05 \mu\text{m}$ thick) whose application can be accomplished either by centrifugal spin or by spray deposition. Following photoresist application, a window is exposed and developed in the photoresist photolithographically, Fig. 4-22(a). At this point, the photoresist is hardened at 210°C for 1 hr. The photoresist mask is now insoluble in CH_3OH and C_2HCl_3 , facilitating a suitable surface for the holographic processing.

The next process in the procedure is the holographic production of photo-resist gratings. The preholographic, surface preparation consists of an abrasive application of CH_3OH followed by a flowing of C_2HCl_3 over the surface, immediately followed by a drying flow of dry N_2 . The holographic photo-resist is then applied, using either the centrifugal spin or spray deposition technique, to a thickness of $0.15 \mu\text{m}$, Fig. 4-22(b). Following the photoresist application and prior to exposure, the coated sample is baked at 70°C for 25 min. The photoresist is then holographically exposed, Fig. 4-22(c), and the resultant grating replicated into the GaAs material by ion beam milling, Fig. 4-22(d). Following this step, the residual photoresist from the first ion mask is now removed in an O_2 plasma, Fig. 4-22(e).

The second phase of the multiple-masking procedure involves the addition of succeeding gratings on the same substrate. A $0.5\text{-}\mu\text{m}$ -thick film of photoresist (for the protection of the first grating during the ion milling of

DBR LASER ARRAY

DISTRIBUTED BRAGG DEFLECTOR



OUTPUT GRATING COLLIMATOR

Fig. 4-21. Three Primary Devices on Common Substrate

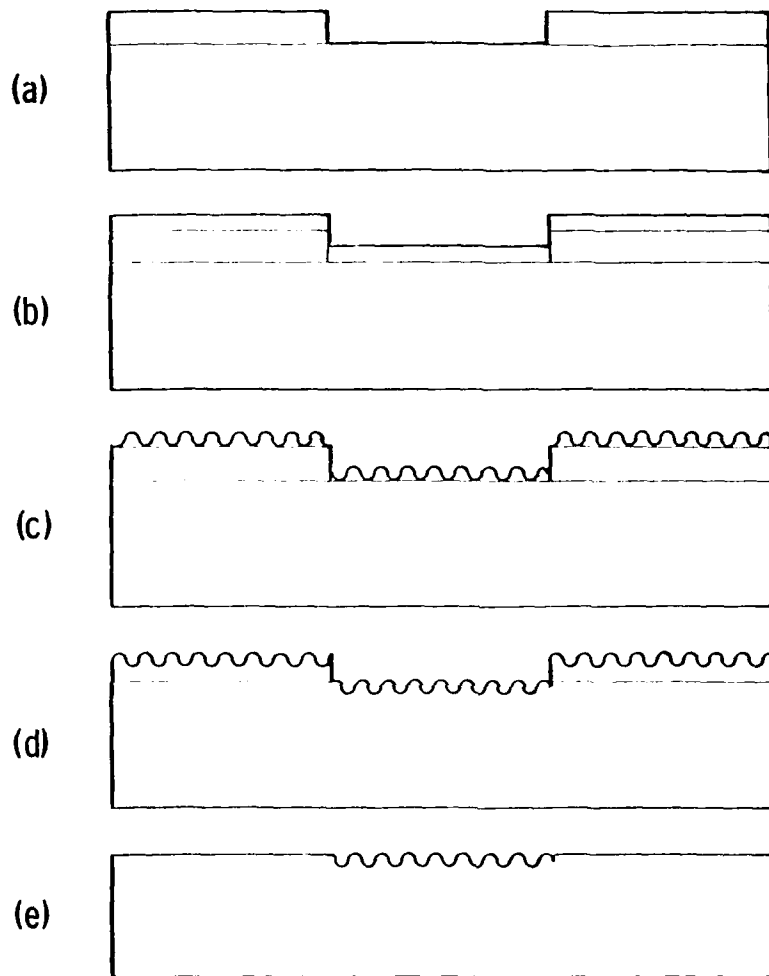


Fig. 4-22. Fabrication of Holographic Gratings

the second grating) is first deposited onto the substrate. A window is then exposed photolithographically and developed in the photoresist film, Fig. 4-23(a), thereby facilitating the application of a $0.15\text{-}\mu\text{m}$ film of photoresist on the substrate surface while still providing an ion-milling mask for the protection of the first grating, Fig. 4-23(b).

The substrate is now ready for the second holographic exposure. The substrate is aligned, exposed, and developed, Fig. 4-23(c), as described earlier. At this point, the substrate is again rotary ion milled in order to replicate the photoresist grating into the surface, Fig. 4-23(d). Whatever residual photoresist remains is then removed in an O_2 plasma (power density of $\sim 8\text{ W/cm}^2$), Fig. 4-23(e). What remains are two precisely placed diffraction gratings with different periodicities and orientations on a common substrate.

This technique can be repeated any number of times, in the integration of an arbitrary number of thin film optical devices, each requiring diffraction gratings of differing periodicity, orientation, depth, and geometry.

This multiple-placement technique has proven to be useful in the integration of various thin-film optical devices as a result of the resolution and placement capabilities of high-resolution photolithography (placement accuracies of ~ 3 to $5\text{ }\mu\text{m}$ and edge resolutions of $\sim 1\text{ }\mu\text{m}$). In addition, grating orientations can be controlled to an accuracy of 0.16 deg of arc and grating periodicities to accuracies of three parts in $10^{-4}\text{ }\mu\text{m}$.

4.3 LOCKING OF LASER STRIPE ARRAYS

The concept of the high-brightness laser included obtaining power levels of 0.1 to 1.0 W by locking several DBR lasers together. In parallel with DBR laser development, some initial studies were made on locking of Fabry-Perot stripe geometry lasers. A theoretical study of coupled lasers appears in Appendix E. The geometry of the first laser array studied is shown in Fig. 4-24.

The lasers were pulsed, and device behavior was mapped out from near field profiles obtained as a function of frequency for different input

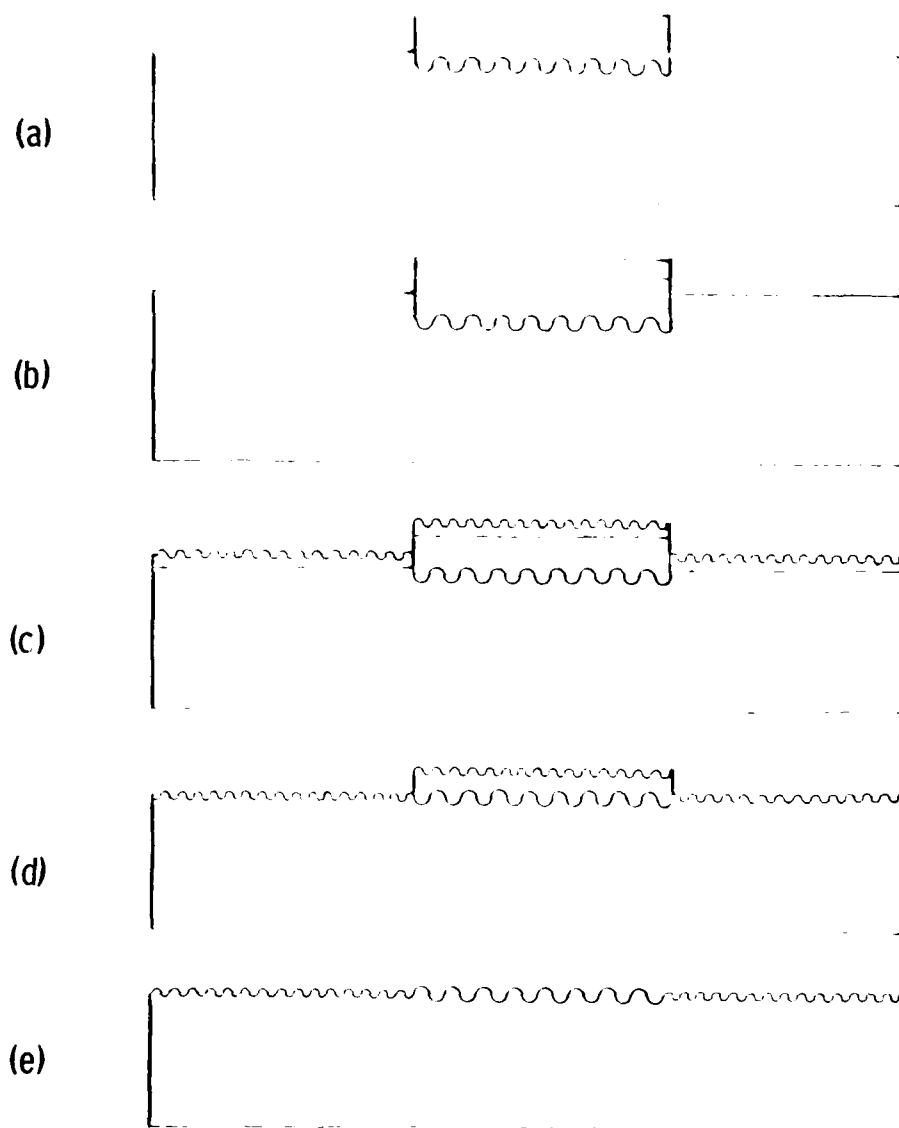


Fig. 4-23. Multiple Grating Fabrication

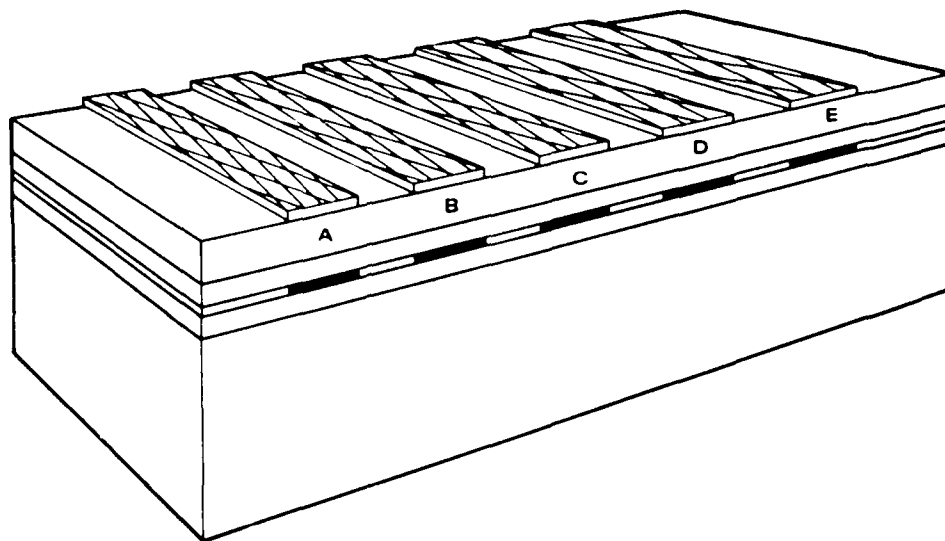


Fig. 4-24. Laser Stripe Array

currents. Optical coupling was indicated by noting the development of a new laser frequency in one stripe due to the presence of adjacent stripes (Fig. 4-25). At 0.38 V, only stripe A was lasing, at frequency ν_2 , and the spectrum of stripe B showed only a weak component at frequency ν_2 because of optical coupling from laser A. The threshold for stripe B was 0.39 V, at which point frequency ν_1 began to lase, taking over and becoming dominant as the current was increased. This new laser frequency ν_1 was optically coupled to stripe A and caused laser action at frequency ν_1 in stripe A.

This interpretation was verified by observing near-field profiles at the two frequencies (Fig. 4-26). Frequency ν_2 occurred strongly only in stripe A, while at frequency ν_1 , all three stripes were lasing at high current levels. The double peak at frequency ν_1 in stripe A was because of depletion resulting from action at frequency ν_2 . Suppression of frequency ν_2 , such as with use of DBR, would result in three coupled stripes lasing only at frequency ν_1 .

A model for optical coupling between the laser stripes considers directionally coupled single mode waveguides. In the strong coupling limit, the directional coupling coefficient becomes

$$K = (\Delta\epsilon w)^2 k_o^3 \left[\frac{\exp(-\Delta\epsilon w) k_o^2 s}{\epsilon} \right]^{1/2} \quad (4-9)$$

where k_o is the free-space propagation vector, $\Delta\epsilon$ is the difference in dielectric constant between the laser and surrounding region, w is the stripe width, and s is the stripe separation. This coupling coefficient has a maximum value at $\Delta\epsilon w = 2/sk_o^2$, which is $K_{\max} = 0.74/\lambda/2\pi |s^2 L \epsilon|^{1/2}$. This maximum value of coupling is the same order of magnitude as that which simple diffraction would produce. For the 26- μ m stripe separation used in this experiment, the fractional optical coupling power in length L would be $\Gamma = K^2 L^2 = 0.0012$. This can be compared to the optical coupling which was observed in Fig. 4-27, which is of the order of 5%. The higher experimental coupling coefficient is due to the effect of gain in the active region. This effect is described in Appendix E. An estimate of the locking range may be made from an analysis by

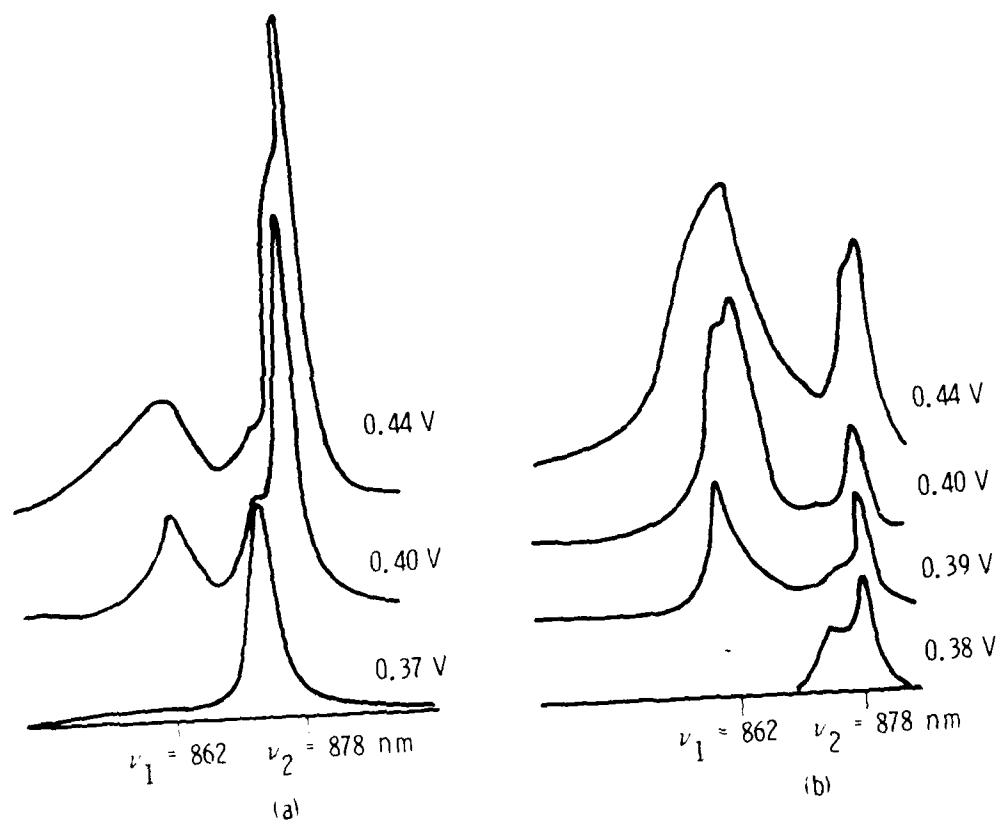


Fig. 4-25. Spectra for Optically Coupled Lasers. (a) Output from stripe A. (b) Output from stripe B.

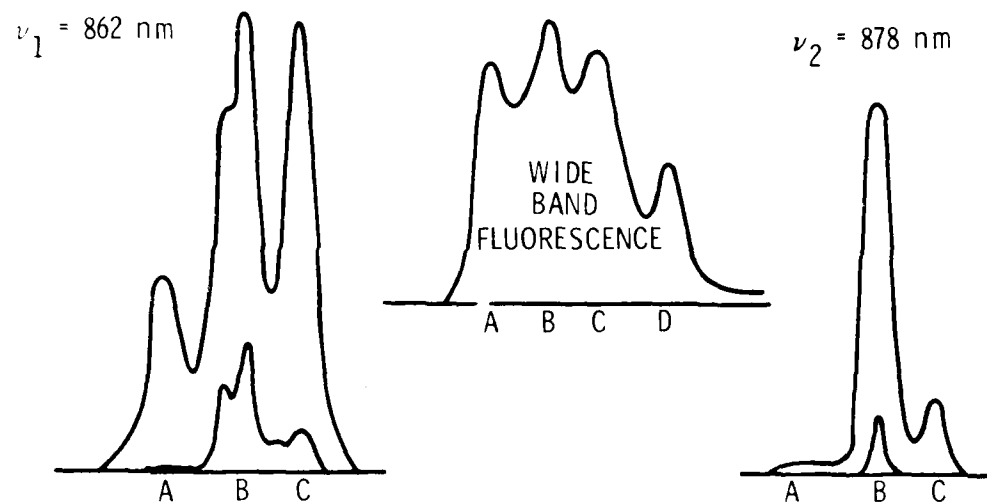
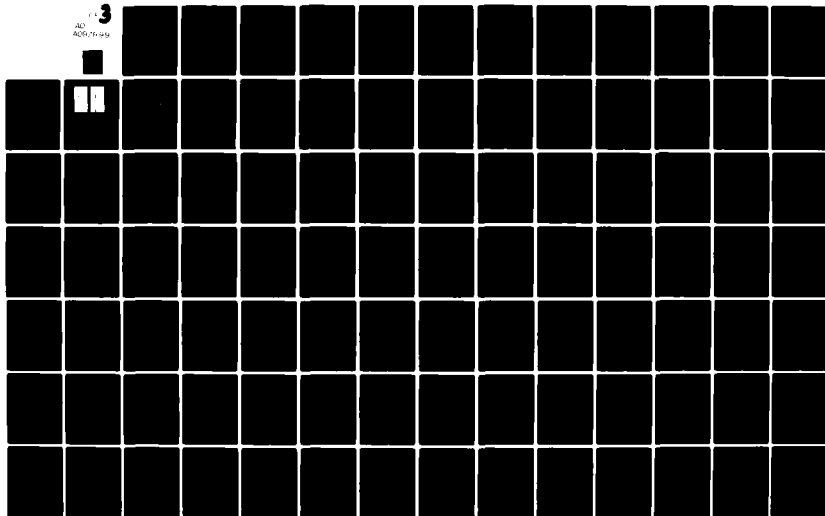


Fig. 4-26. Near-Field Intensity Profiles for Laser Stripe Array

AD-A097 899

AEROSPACE CORP EL SEGUNDO CA ELECTRONICS RESEARCH LAB F/G 20/5
PROGRESS TOWARD A MONOLITHICALLY INTEGRATED COHERENT DIODE LASE--ETC(U)
FEB 81 G A EVANS, E M GARMIRE, H M STOLL F04701-80-C-0081
UNCLASSIFIED TR-0081(6930-04)-2 SD-TR-81-7 NL

3
AD
A097899



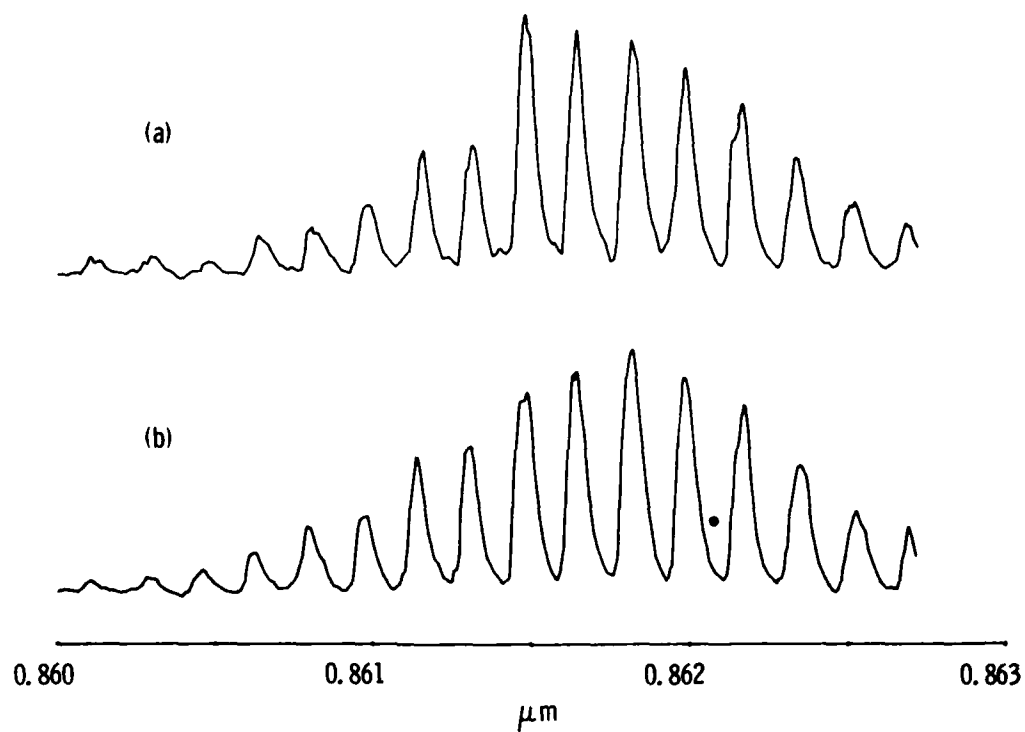


Fig. 4-27. Spectra for Locked Lasers. (a) Output from stripe A.
(b) Output from stripe B.

Basov,⁷ who showed that lasers of length L can be locked as long as they differ in wavelength by less than $\delta\lambda$

where

$$\frac{\delta\lambda}{\lambda} < \Gamma/2\pi L \quad (4-10)$$

and Γ is the exchange of energy between adjacent lasers. Since the experimentally observed optical coupling was on the order of 5%, the estimated locking range is 0.04 Å. If the parallel DH lasers are not close enough in frequency, they may be tuned with separate excitation of the individual laser stripe. This varies the local temperature or refractive index the small amount necessary to lock the lasers.

Additional measurements were completed to demonstrate locking by using a high-resolution spectrometer and comparing individual laser mode frequencies of two adjacent laser stripes. The device geometry was the same as that shown in Fig. 4-24. In order to prove locking, it is necessary to demonstrate that both laser stripes oscillate at the same frequency. This is discussed in more detail in Appendix E. For these reasons, we carefully investigated the laser frequencies to measure locking and studied devices L10B and L10C.

The spectrum of laser stripe arrays made from L10B is shown in Fig. 4-28. The top trace is that of stripe A and the bottom trace is that of stripe B. Since these stripes were pumped in parallel, it was not possible to look at each spectrum without the effects of the adjacent stripe. However, it is clear that stripe A has a spectrum that peaks about 0.8625 μm , whereas stripe B has a spectrum that peaks about 0.8607 μm . In addition to the peak

⁷N.E. Basov, E.M. Belenov, and V.S. Letokhov, "Diffraction Synchronization of Lasers," Sov. Phys.-Tech. Phys., 845 (1965).

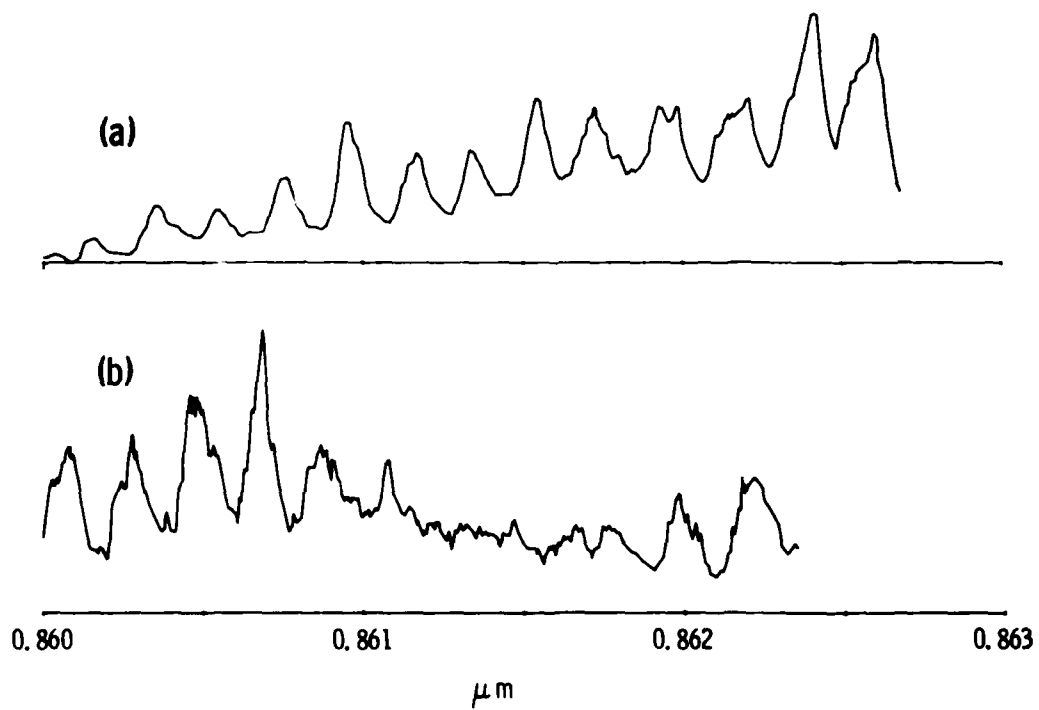


Fig. 4-28. Spectra for Unlocked Coupled Lasers. (a) Output from stripe A. (b) Output from stripe B.

wavelength, it can be seen that each stripe contains some light at the wavelength of the adjacent stripe, causing the spectrum of stripe A to have a subsidiary maximum at 0.8610 μm and stripe B to have a subsidiary maximum at 0.8623 μm . These subsidiary maxima are caused by optical coupling between the adjacent laser stripes, which, in this case, were separated by 25 μm .

When the laser stripes are closer together, they are locked. This is demonstrated by the spectra in Fig. 4-25. These data were obtained on sample L10D whose stripes are separated by 13 μm . In this case, both lasers have very similar spectra, proof that they are locked together. The spectra of locked lasers are particularly simple. The numerical analysis of this physical situation is discussed in more detail in Appendix E.

4.4 BEAM DEFLECTION AND EXPANSION

Beam expansion can be achieved with the use of a distributed Bragg deflector (DBD). This device consists of a corrugated waveguide, with a grating slanted at an angle θ with respect to the incident beam. The geometry of the DBD is shown in Fig. 4-29. The incident beam enters from the left into a confined slab guide with a corrugated surface. Bragg reflection occurs from the grating, reflecting the beam at an angle equal to the incidence angle. However, the reflections from the corrugations add up coherently only if the Bragg condition is satisfied, that is,

$$\Lambda = \frac{\lambda_m}{2n \sin(\theta/2)} \quad (4-11)$$

In addition to beam expansion, applications of the DBD include beam splitters (power division), deflectors (as, for example, to create ring geometries), polarizers and analyzers (with 90 deg deflection), and multiplexers-demultiplexers (with chirped gratings).

The theoretical analysis of the device was completed during the initial phases of the contract and is presented in Appendix F. For this reason, only the results of that theoretical analysis are presented in the section.

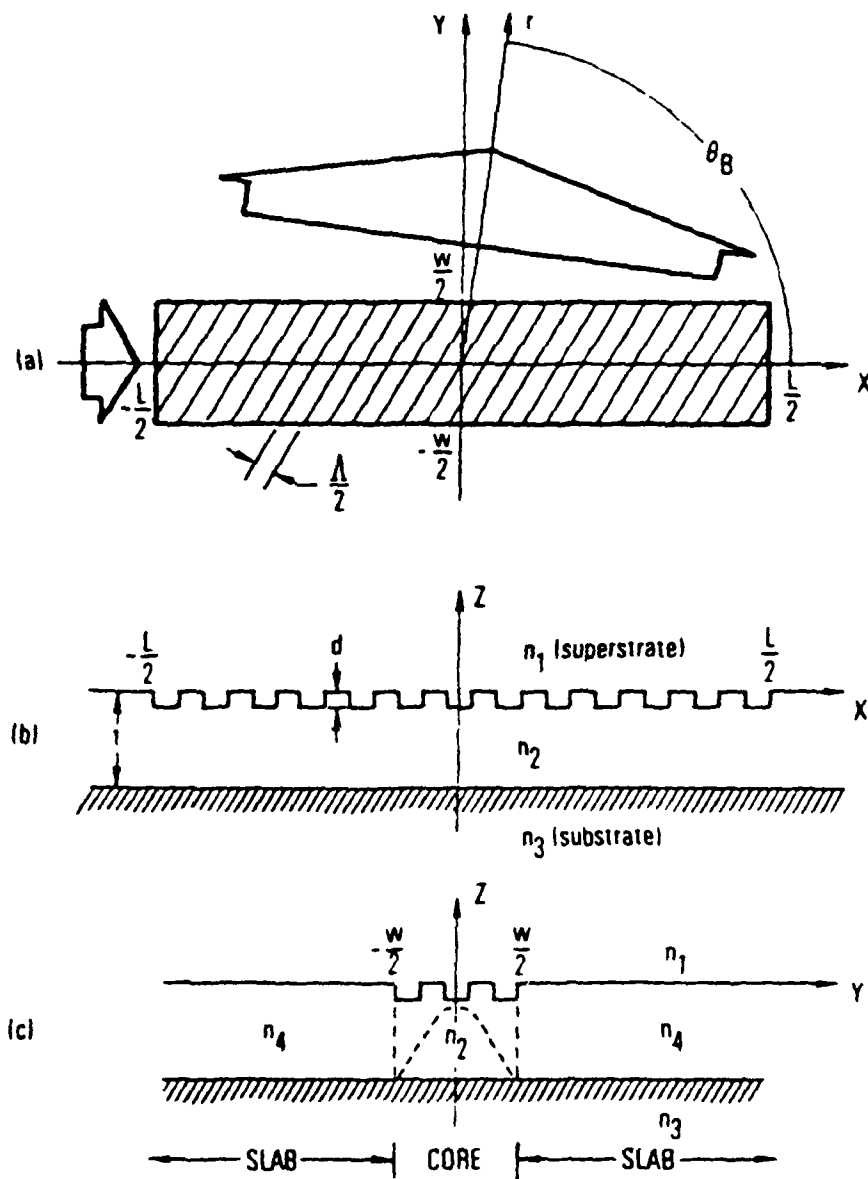


Fig. 4-29. DBD. (a) Top view. (b) Side cross-sectional view. (c) End cross-sectional view. Small and large (solid) arrows in (a) represent incident and deflected beams, respectively. Dashed sinusoid in (c) represents equivalent core field distribution in y -direction.

It was found that the incident-light-beam amplitude is reduced while traveling through the DBD region by an exponential factor with distance, that is, $\exp(-\gamma z)$, because of deflection. The results of the calculation are:

$$\gamma_{TE} = \nu \cos \theta_B \quad (4-12)$$

and

$$\gamma_{TM} = \nu \left[\frac{2n_2^2}{(n_2^2 - n_1^2)} \log \left(\frac{n_2}{n_1} \right) (\cos \theta_B - 1) - \cos \theta_B \right]^2 \quad (4-13)$$

where

$$\nu = w \left[\frac{4\pi(n_2^2 - n_1^2)d^3}{3(2l - 1)n_2\lambda_o t_e^3} \right]^2 \quad (4-14)$$

The quantities are as defined in Fig. 4-29, with λ_o the wavelength of incident light, l the Bragg scattering order, and t_e the effective guide thickness, ($t_e = t + 1/\delta$, where δ is the exponential decay constant of the mode in the substrate).

Consider the deflection of a TM polarized beam at 90 deg which is the configuration of greatest interest for beam expander applications:

$$\gamma_1 = \nu \left[\frac{2n_2^2}{n_2^2 - 1} \log n_2 \right]^2 \quad (4-15)$$

We have made use of the fact that $n_1 = \text{air} = 1$.

It is convenient to relate these results to those of retroreflection in a corrugated waveguide. By means of the coupled mode theory, it is predicted that a corrugated waveguide will couple forward and backward waveguide modes

with a coupling coefficient K . Light originally travelling forward transfers to the backward wave exponentially with length, with a coefficient given by K . Thus, the effectiveness of a grating can be described by describing its coupling coefficient. For square corrugations such as those used to derive Eq. (4-13), the coupling coefficient is

$$K = \frac{2\pi^2 \Delta n^2}{3 (2\ell - 1) \lambda n_g} \left(\frac{d}{t_e}\right)^3 \quad (4-16)$$

A related parameter is the characteristic distance at which the power in the initial mode decreases by a factor of $1/e$. This characteristic length is given by $l_g = (2K)^{-1}$. We then write the DBD exponential coefficient as

$$\gamma_{\perp} = \left[\frac{4n_g^2 \log n_g}{\pi (n_g^2 - 1)} \right]^2 K^2 W \quad (4-17)$$

Since the deflected beam has an amplitude that decreases with distance along the DBD according to an exponential with a coefficient γ , the intensity width of the expanded beam will be approximately $1/2 \gamma$.

Defining the expansion factor as the width of the deflected beam divided by the incident beam width, we write the expansion factor as

$$F_{\perp} = \frac{1}{2\gamma_{\perp} W} = 2 \frac{\pi (n_g^2 - 1)}{4n_g^2 \log n_g} \frac{L_g^2}{W} \quad (4-18)$$

$$\equiv 2f^2 \left(\frac{L_g}{W} \right)^2$$

where we have defined the grating by its characteristic length.

It is easy to obtain large expansion factors, since the characteristic length of gratings can be typically larger than W . The research program was designed first to demonstrate beam expansion in high optical quality vapor-phase epitaxy (VPE) GaAs waveguide material and then to apply the concept to liquid-phase epitaxy (LPE) GaAs double heterostructures, so that the laser and beam expander could be combined into the same substrate.

Demonstration of beam expansion in VPE GaAs epilayers was successful. A perspective view of the Bragg-effect polarizer-analyzer that we fabricated is shown in Fig. 4-30. The asymmetric slab waveguide structure consisted of a $1\text{-}\mu\text{m}$ thick, n-type, $\lesssim 10^{16}\text{ cm}^{-3}$ GaAs layer epitaxially grown over a heavily doped n-type, $\sim 5 \times 10^{18}\text{ cm}^{-3}$ GaAs substrate; it supported only the lowest order one-dimensional, transverse electric (TE) and transverse magnetic (TM) polarized modes. Ninety-degree Bragg scattering of the incident $1.15\text{-}\mu\text{m}$ radiation was accomplished by means of a second-order periodic surface corrugation ($\Lambda = 0.478\text{ }\mu\text{m}$) that was ion milled into the waveguide surface and overcoated with a $0.1\text{-}\mu\text{m}$ -thick layer of aluminum in order to increase its deflection efficiency. As revealed by SEM examination of a cross section through the device, the corrugations bore a nearly triangular tooth profile. The total corrugation length L and input beam width W were 3.2 mm and $50\text{ }\mu\text{m}$, respectively.

A semilogarithmic plot of the near-field deflected-beam intensity profile of one of our 90-deg Bragg deflectors is shown in Fig. 4-31. The data indicate that the deflected beam decreases by a factor of $1/e$ in 1.3 mm length. With an input beam of $50\text{ }\mu\text{m}$, this corresponds to an expansion factor of 38. From these data, it can be inferred that the effective coupling length of the grating was $L_g = 385\text{ }\mu\text{m}$, with a coupling coefficient of $K = 0.0013$. The reason for the weak coupling coefficient is the use of VPE GaAs. The index change caused by the reduction of the number of free carriers in the epilayer is very small. As a result, the guided mode extends into the substrate, and the effective guide width is larger than the $1\text{-}\mu\text{m}$ physical thickness of the epilayer. For the physical parameters used in the experiment, the effective guide thickness was several microns, causing the coupling coefficient to be small.

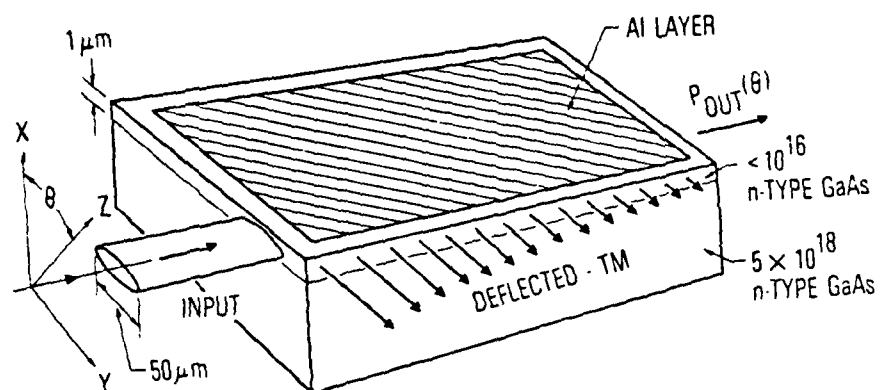


Fig. 4-30. Perspective View of Bragg-Effect Polarizer-Analyzer. Electric-field vector of input beam is oriented at angle θ to waveguide surface normal.

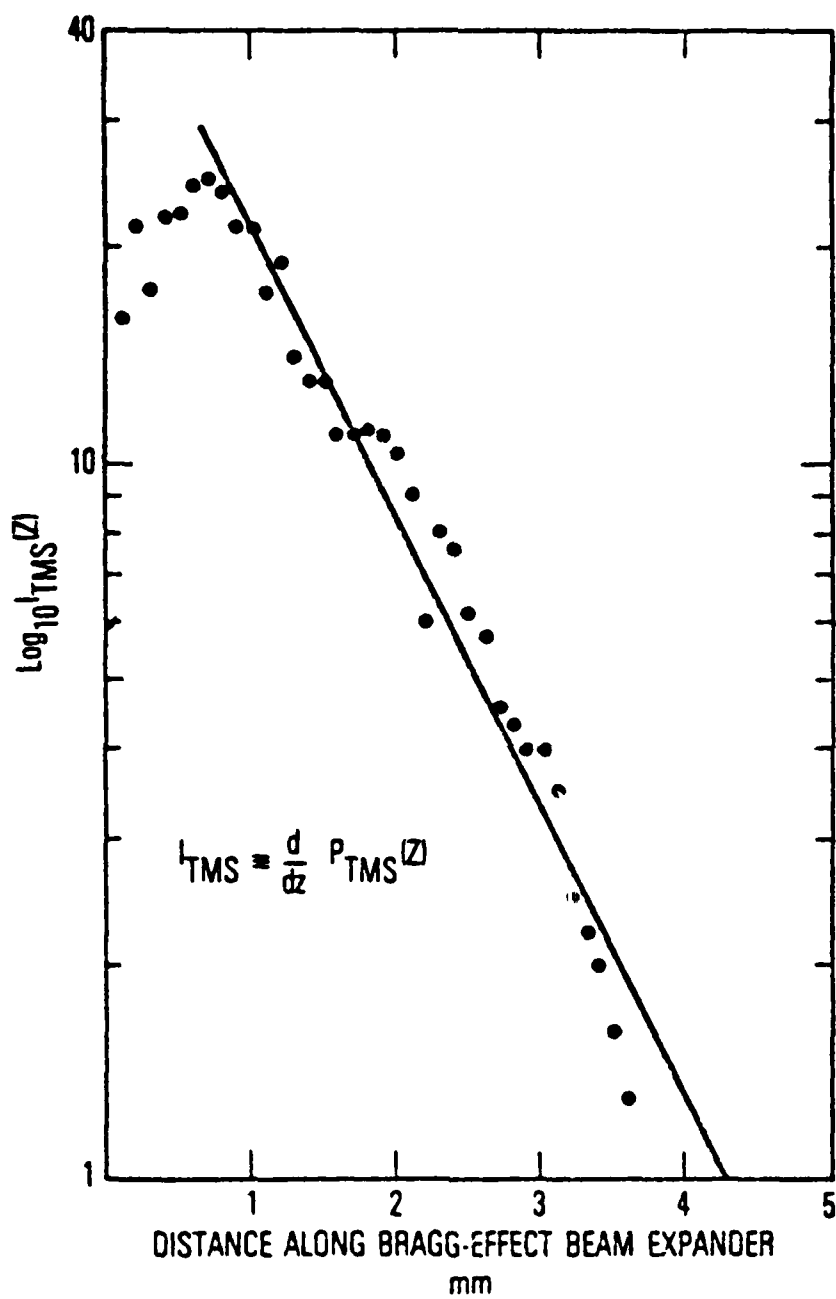


Fig. 4-31. Semilogarithmic Plot of Near-Field Bragg Scattered Beam Intensity Profile of 90-deg Deflector

Because of the weakness of guiding in the VPE material, the effective waveguide thickness was large and the grating coupling coefficient was small. We demonstrated that even a grating with a low-coupling coefficient can be used successfully as a polarizer-analyzer. A study of this effect was undertaken; the results of this study have been submitted for publication⁸ and are summarized in this report.

Operation of the DBD as a polarizer-analyzer can be seen by observing that $\gamma_{TE} = 0$ for a deflection angle of 90 deg. Polarizer-analyzer performance parameters of interest include the extinction ratio ρ , which we define as being equal to the ratio of TM to TE mode power deflected by the device, or

$$\rho = \frac{\gamma_{TM}}{\gamma_{TE}} \frac{\delta_{TE}}{\delta_{TM}} \frac{1 - \exp(-2 \delta_{TM} L)}{1 - \exp(-2 \delta_{TE} L)} \quad (4-19)$$

and the TM deflection efficiency η , which we define as being equal to the ratio of deflected to incident TM mode power, or

$$\eta = \frac{\gamma_{TM}}{\delta_{TM}} [1 - \exp(-2 \delta_{TM} L)] \quad (4-20)$$

In Eqs. (4-19) and (4-20), δ_{TE} and δ_{TM} are the total (including background) TE and TM mode attenuation coefficients, respectively, and L is the device length.

Experiments were performed on the polarization dependence of beam deflection using the VPE GaAs waveguide beam expander shown in Fig. 4-30. By measuring the near-field intensity profile of the beam which was Bragg

⁸H.M. Stoll and W.E. Soady, "Bragg Effect Polarizer/Analyzers and Lensless Waveguide Beam Expanders," presented at Integrated Optics Conference, Lake Tahoe, 1980.

deflected by the polarizer-analyzer, δ_{TM} , was determined to be 4.19 cm^{-1} . Knowledge of δ_{TM} together with measurements of the undeflected throughput power

$$P_{out}(\theta) = P_{in} [\cos^2 \theta \exp(-2 \delta_{TM} L) + \sin^2 \theta \exp(-2 \delta_{TE} L)] \quad (4-21)$$

$\theta = 0$ and $\pi/2$ were then used to yield $\delta_{TE} = 3.11 \text{ cm}^{-1}$, $\gamma_{TM} = 0.154 \text{ cm}^{-1}$, and $\eta = 0.034$. Direct measurement yielded an extinction ratio of 343 from which it was inferred that $\delta_{TE} = 3.6 \times 10^{-4} \text{ cm}^{-1}$. In Fig. 4-32, the $P_{out}(\theta)$ and $P_{TMS}(\theta)$ (the total TM power deflected) are plotted, and the experimental data summarized.

The passive beam expander in VPE GaAs demonstrated that beam expansion was indeed possible with the DBD. However, it was also demonstrated that the efficiency of deflection goes to zero for the TE mode at a deflection angle of 90 deg.

In Figure 4-33, a DBD at 45 deg, which was fabricated in VPE GaAs, is shown. The beam expansion is shown in Fig. 4-33 (bottom) as a streak to the left of the beam. The difficulty in observing this device is the necessity of polishing the end face to obtain the output at 45-deg. The advantage is that the grating can be used in fundamental order. The deflection of the DBD in the VPE waveguide was very weak, because the waveguide was so thick. Experiments on 45-deg deflection in thinner LPE GaAs waveguides are planned in the future.

To determine the required grating spacing for a DBD, it is necessary to measure β_1 , the propagation constant in the guide. For the VPE grown GaAs waveguides, the measured value of β was $18.887 \pm 0.002 \text{ } \mu\text{m}^{-1}$, determined for the output angle of 43.23 deg for a grating spacing of $0.4217 \text{ } \mu\text{m}$. The experimental setup used to make this measurement is shown in Fig. 4-34.

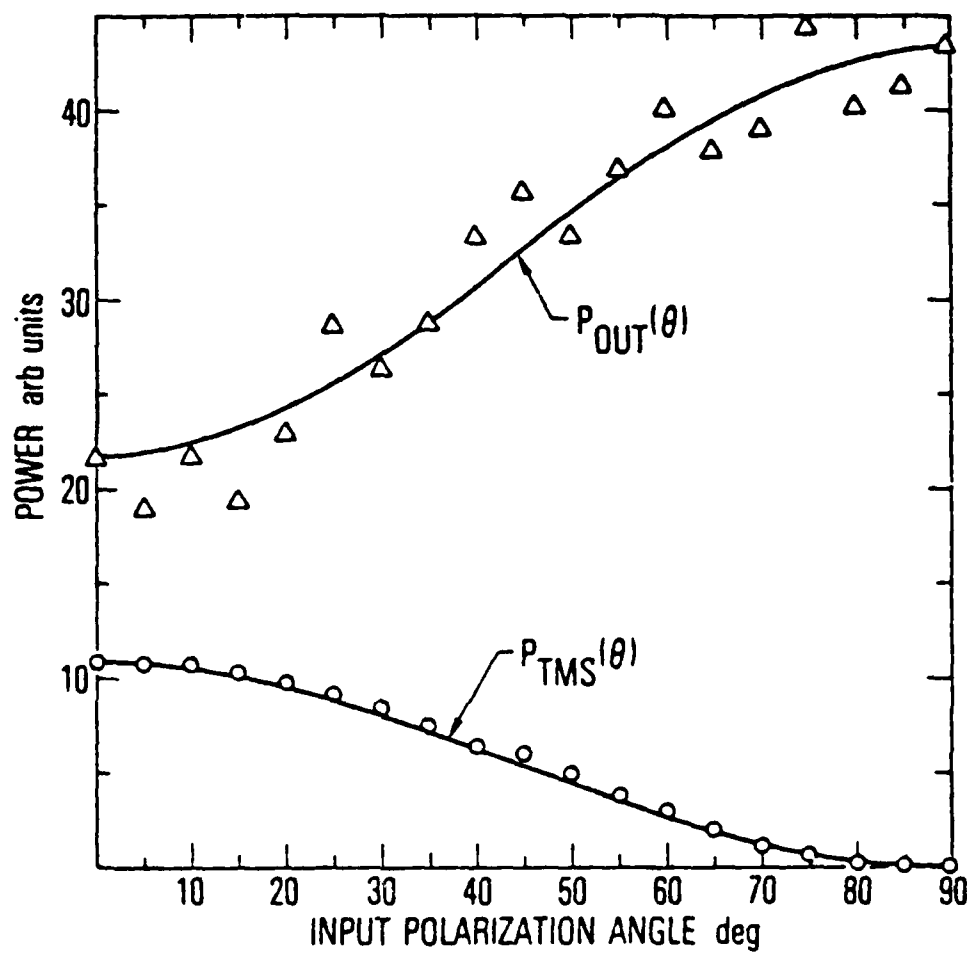


Fig. 4-32. Plots of Throughput Power $P_{out}(\theta)$ and Bragg-Scattered Power $P_{TMS}(\theta)$ as Functions of Input-Beam Polarization Angle θ . Also shown are experimental data Δ and O.

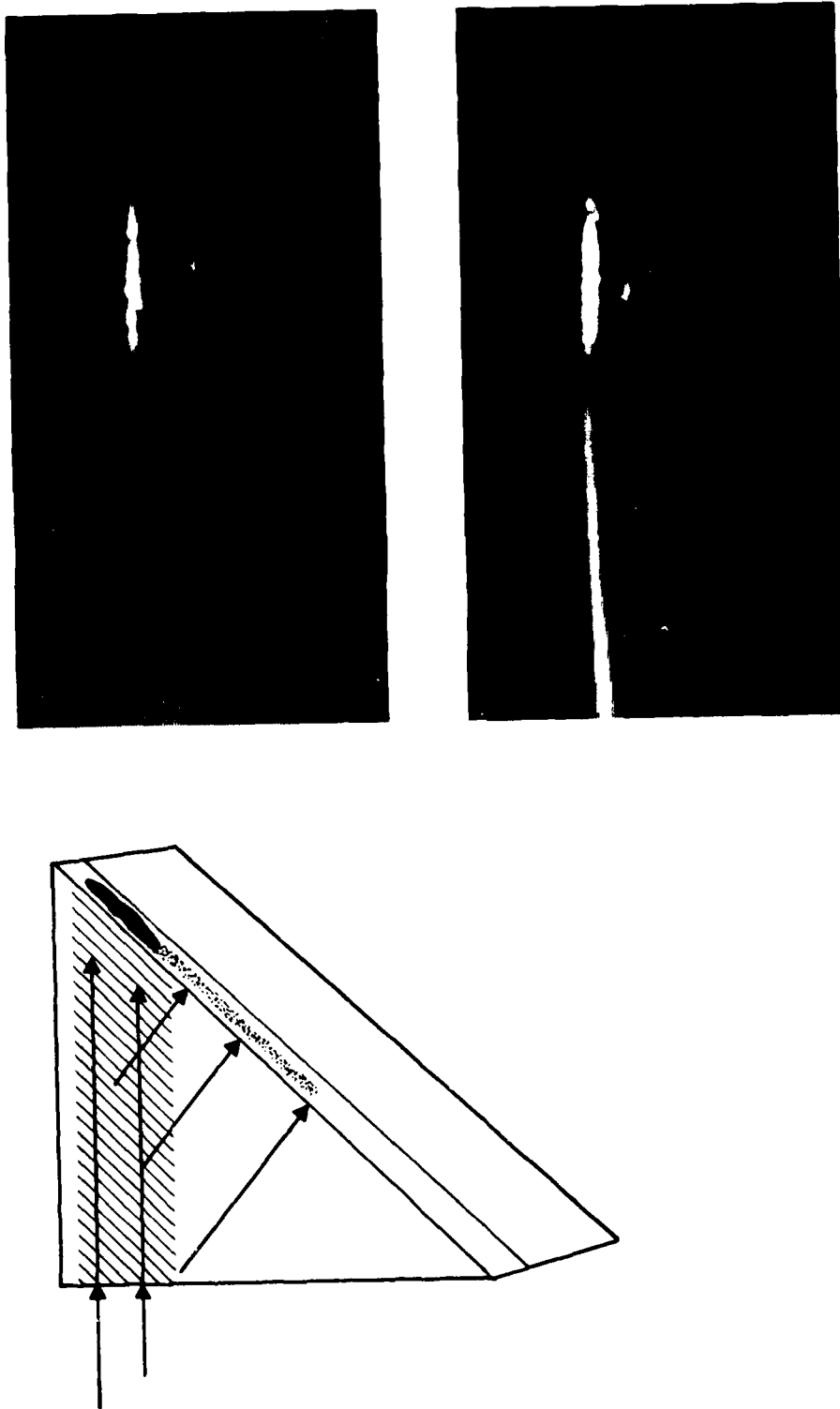


Fig. 4-33. Geometry for 45-deg Beam Expander Along with Photographs of IR Television Monitor of Near-Field Image of Guided Beam. Top photograph represents unexpanded beam 50- μ m wide before proper angular alignment. Bottom photograph represents beam expansion with the streak to the left.

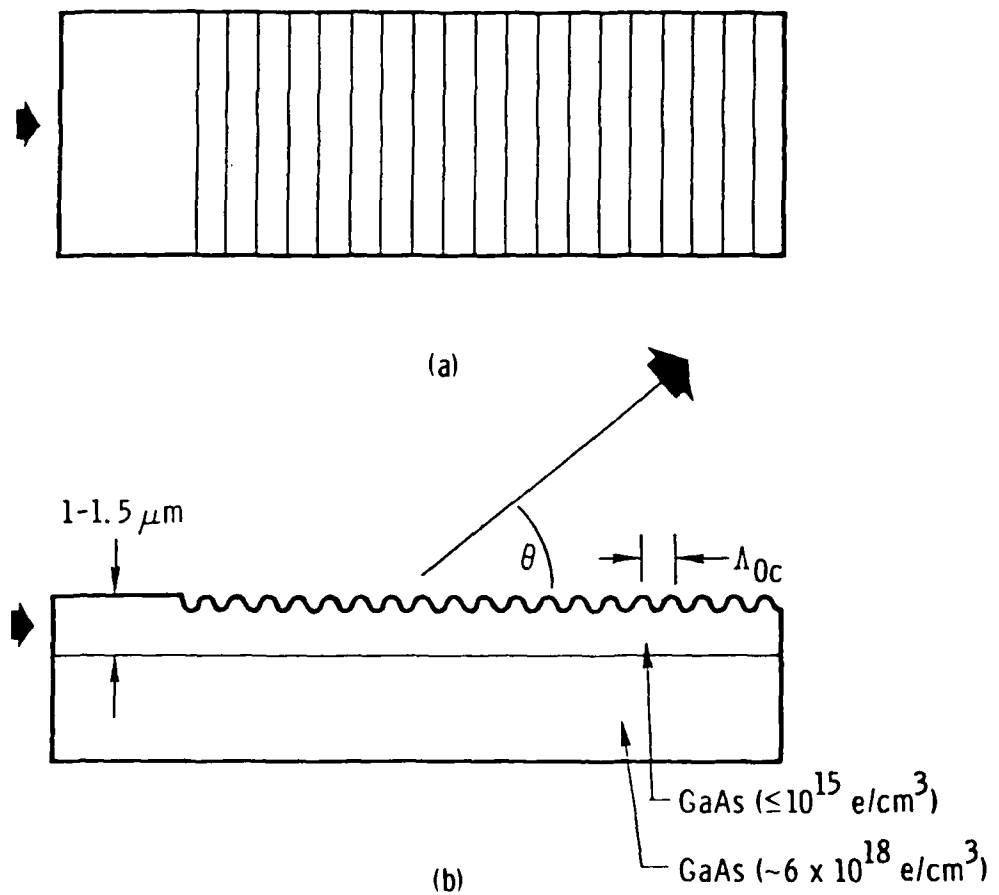


Fig. 4-34. Output Grating Coupler Used to Measure Waveguide Propagation Constant β . (a) Top view. (b) Side view.

Knowledge of the output coupler period to one part in 10^4 permitted determination of the guided-wave propagation constant β , to similar accuracy according to:

$$\beta = \frac{2\pi}{\Lambda_{oc}} + \frac{2\pi \cos \theta}{\lambda} \quad (4-22)$$

where Λ_{oc} is the output coupler period, λ is the free-space measurement wavelength, and θ is the output extraction angle. Once β is known, the requisite DBD grating period, Λ_{DBD} , for second order 90 deg deflection can be given by:

$$\Lambda_{DBD} = \frac{4\pi}{2\beta}$$

5. CONCLUSIONS AND SUMMARY

Although the goal of building a fractional watt laser array with low-beam divergence was not met, substantial progress was made. Distributed Bragg reflector (DBR) lasers were fabricated and tested. Distributed Bragg deflectors (DBD) were fabricated and proved to be useful for beam expanders and polarizer-analyzer elements in optical circuits. Output couplers and DBDs were integrated on the same chip, and experiments were performed on coupled-stripe geometry lasers to study the basic physics of injection locking.

Device integration, in the form of a high-brightness laser, requires the ability to routinely fabricate DBR lasers, DBD gratings, and output couplers, and to be able to place such devices on a single crystal with close tolerances. Current laboratory efforts are directed toward increasing the yield of our devices by refining our fabrication processes.

In addition, device integration requires suitable material free of irregularities with good optical and electrical qualities over large areas. Toward this end, in addition to refining our liquid phase epitaxy (LPE) capability, we are constructing a metal organic chemical vapor deposition (MOCVD) system with which to grow material.

We are hopeful that our current efforts will result in a high-brightness GaAlAs laser.

APPENDIX A

LPE CRYSTAL GROWTH PROCEDURE

A.1 MELT PREPARATION

A.1.1 Source Material

1. Sn. 5-9s pure 1/8-in.-diameter shot.
2. Ge. High-purity ingot, small broken pieces.
3. Al 5-9s pure wire, 0.020-in. diameter.
4. GaAs. (100) orientation, $7.5 \times 10^{15}/\text{cm}^3$ concentration, EPD = 1000-2000/ cm^2 ; 0.018-in. thick. Cleaved into small pieces.
5. Ga. 7-9s pure. Poured as a liquid from a plastic squeeze bottle.

A.1.2 Weighing

1. Cut or cleave dopants into pieces weighed on analytical balance to ± 0.0005 g. Al is weighed to ± 0.0001 g.
2. Ga is weighed in an HF-cleaned glass beaker as a liquid. With the use of an eyedropper, it can be weighed to ± 0.0010 g.

A.1.3 Cleaning

1. Dopants Sn and Ge and GaAs are placed in a clean beaker with hot isopropyl alcohol for approximately 1/2 hr. Dopants are then Ar-dried and placed in a covered petri dish.
2. Al is not put into isopropyl alcohol because it can react with any trace water to form a hydroxide.
3. Ga, weighed as a liquid in a glass beaker, has H_2O plus 5 to 10 drops of HCl added. It is heated for about 10 min. Then, the beaker is placed in an ultrasonic cleaner for cleaning in xylene and rinsing in isopropyl alcohol. After an Ar-dry, the thickness is measured.

4. Both the substrate and lead crystals are then cleaned in hot isopropyl alcohol held in a vertical position by a glass holder submerged in isopropyl alcohol. They soak for about 1 hr while the melt material is being weighed. They are rubbed with Q-tips wet with alcohol and rinsed in the hot isopropyl alcohol several times to rid the surface of any dirt. After argon drying, the samples are then inspected by microscope. Sometimes they are cleaned in isopropyl alcohol in the ultrasonic cleaner, but this is avoided if possible because the ultrasonic sometimes causes breakage. The crystals are Ar-dried and kept covered until loaded into the boat.

A.2

BOAT

1. A six-well graphite boat has been used with a sliding graphite plug top. This plug top can be pushed forward to force the Al, which is resting on the top edge of the melt hole, to fall into the molten melts at elevated temperatures (600°C).
2. The boat is shown in Figs. A-1 through A-4, and drawings are included at the end of this appendix.
3. The boat is kept under H_2 in the quartz furnace tube until it is loaded, to help keep excess O_2 from absorbing into the porous graphite.
4. The Sn and Ge are placed on the bottom of the melt hole, then the solid Ga is put on top, with the small cleaved pieces of GaAs source material placed on top of the solid Ga. The Al is put on the top edge of the graphite, so it is not in contact with melt, which has oxides that react with Al. To rid the boat of any water vapor, the melts are taken to 600°C for 10 to 15 min to dissociate Ga oxides. At this temperature, Al reacts with graphite to form Al_4C_3 , which is insoluble in Ga and also is a source of contamination to the substrate surface. Therefore, the soaking time is kept at 15 min or less before the Al is pushed into the oxide-free melts. The furnace temperature is then taken to 860°C and held for about 4 hr.
5. Cleaved small pieces of GaAs are used to float on top of Ga, because one large plate on top would prevent the Al from falling into the melt. On the other hand, very small powder-like material would allow pieces to be trapped on the substrate surface while the crystal is growing and would cause imperfections.
6. During the loading procedure, cotton gloves are worn to keep the graphite boat and quartz furnace from being contaminated.

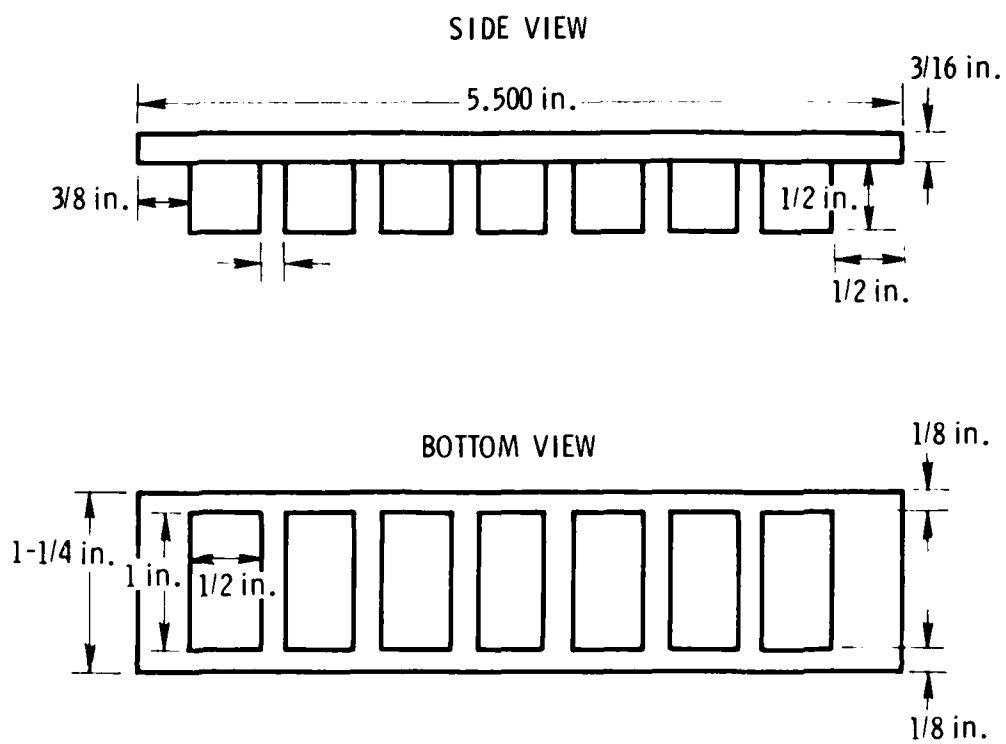


Fig. A-1. Plug

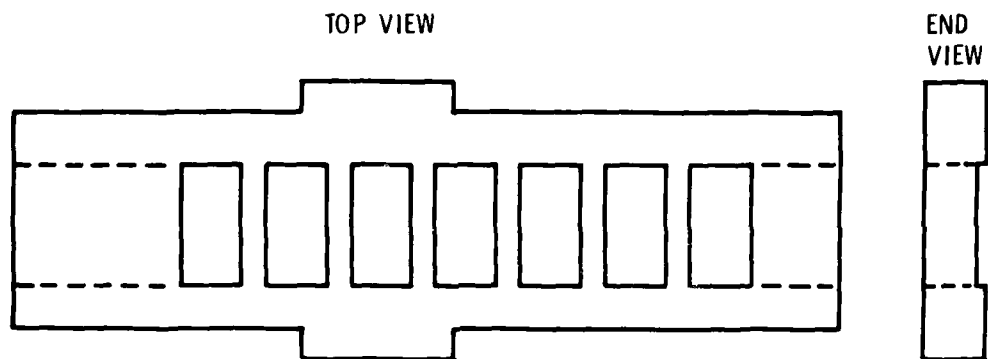


Fig. A-2. Melt Holder

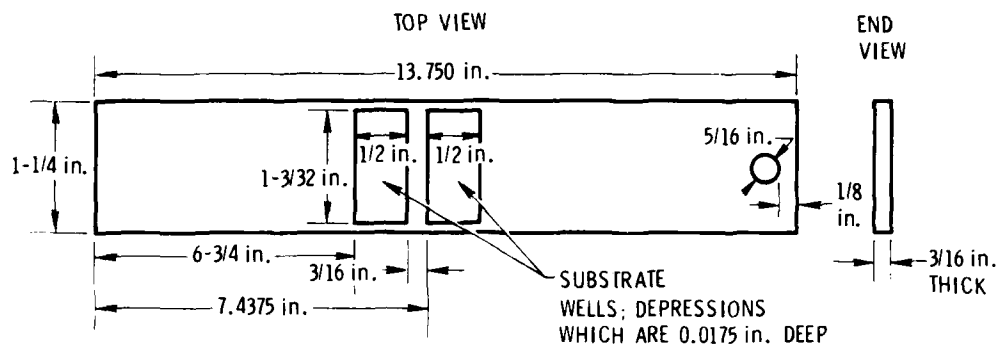


Fig. A-3. Slider

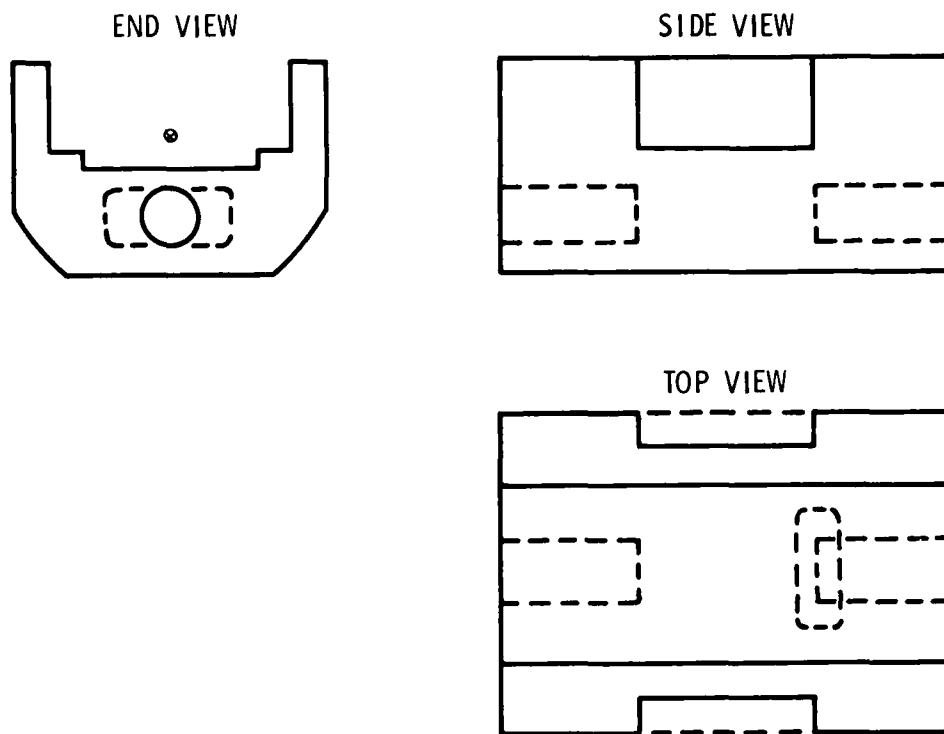


Fig. A-4. Boat Holder

A.3

FURNACE

1. The Thermco electric furnace, tube type, Kanthal element, 200 to 1200°C control, three-zone control has good temperature stability. It has a flat temperature zone of approximately 10-in. (center). An induced temperature increase of 1°C from the first melt to the last melt keeps etch-back from occurring. Little or no temperature gradient can be measured from top to bottom of the melt area.
2. A quartz tube approximately 2-1/2 in. in diameter and 5 ft long is used to hold the boat under a pure H₂ atmosphere while the melt is in the boat.
3. H₂ is put through a Pd purifier before entering the furnace. It has an oxygen-free purity of parts per billion.
4. The temperature programmer is a Eurotherm Type 125, which is solid state, permitting a very smooth temperature drop of 0.1 to 1°C/min.

A.4

PROGRAM

1. The furnace is evacuated after the boat is placed in its center and back-filled with N. It is evacuated the second time, then filled with pure hydrogen. The use of this vacuum permits leaks to be detected.
2. The furnace is turned on to 400°C with H₂ bubbling through at about 1/2 l/min. It is soaked overnight at 400°C to bake out any water vapor.
3. The next morning, the furnace is raised to 600°C for 1 hr. Then the Al is pushed into the melts, which are fairly free of oxides at this temperature. This greatly helps in limiting the very active Al from oxidizing, which, in turn, keeps the Al₂C₃ from falling on the growing surface.
4. The furnace temperature is then raised to 800 to 850°C and soaked for 3 to 4 hr.
5. The lead crystal, which precedes the substrate by one melt, is pulled under the first melt and left soaking for 10 to 30 min to ensure against melt back.
6. The programmer is turned on to a cooling rate of about 0.0004 mV/min, which is approximately 0.3°C/min. A 100% Pt-13% Rh-Pt thermocouple is used. The temperature is lowered 2 to 3°C to

supercool the melts, which may help smoothness and flatness at the substrate surface because of the rapid growth of GaAs on the surface.

7. The substrate is then pulled to the first melt. The temperature drop is from 0.004 to 0.002 mV/min or 0.3 to 0.15°C/min, depending on desired growth rate for each layer. The active laser layer usually grows for 5 to 20 sec at a rate of 0.3°C/min. This produces a layer thickness of 600 to 3000 Å.
8. After the last layer is grown, the substrate is pulled to the front of the boat, where it remains under the graphite melt holder until it is removed from the furnace.
9. After the furnace has reached room temperature, N₂ is used to purge it of H₂. The boat is removed from the furnace, and the substrate and lead crystals are placed in hot isopropyl alcohol to rid their surfaces of excess Ga melt. A Q-tip is used to rub off Ga.
10. The total time required for one LPE growth and a preliminary crystal analysis is 3 days.

A.5

SUMMARY

1. The substrate is not pre-etched in H₂SO₄ before growth.
2. Trichlorethylene is not used to clean the substrate.
3. Al is pushed into melts at 600°C to reduce oxidation.
4. Melts are supercooled from 0.5 to 5°C to help eliminate etch-back and to help grow smooth surface layers without meniscus lines.
5. Slow growing rate with smooth cooling curve helps eliminate dislocations.
6. Cleaning Ga in H₂O + HCl in the ultrasonic cleaner rids excess oxidation. Freezing Ga in H₂O + 1 to 2 drops of HCl reduces the oxidation rate of Ga while loading it in the boat in air.
7. Bellows valves and leak-tight fittings eliminate O₂ leaks.

APPENDIX B

OPTIMALLY COUPLED GaAs DBR LASERS

B.1 INTRODUCTION

Optimal designs are developed for large optical cavity (LOC) GaAs DBR lasers. Cavity and reflector lengths were determined that permit single-mode single-ended operation over a continuous-wave optical output power range of 5 to 50 mW. With an internal quantum efficiency of 90% assumed, external quantum efficiencies for the optimized structures are found to range from 14.1% (for 5-mW output) to 57.8% (for 50-mW output). Threshold current densities are found to remain less than 1000 amp/cm^2 over the entire optical output range considered.

Two types of periodic feedback lasers have been proposed for use as sources in monolithic semiconductor integrated optical circuits: the distributed feedback (DFB) laser¹ and the DBR laser.² While both configurations offer obvious advantages over the conventional Fabry-Perot semiconductor laser (e.g., freedom of orientation within the integrated optical circuit and lack of facet pitting at high continuous-wave output levels), the DBR laser appears to be superior to the DFB laser for a number of operational and fabricative reasons. First, because of the spectral selectivity of its mirrors, the DBR laser may be designed to lase in a single longitudinal mode instead of in the longitudinal mode pair characteristic of the index-periodic DFB laser.¹ Second, because the laser reflectors can be located away from the active (pumped) region of the device, nonradiative recombination centers introduced during fabrication of the DBR laser reflector gratings³ can be disregarded (the feedback grating of the DFB laser must be contiguous to or very near the active, p-n junction). Third, because the DBR laser reflectors are easily accessible, they can be individually tailored in order to achieve single-ended single-longitudinal-mode operation. Fourth, unlike the DFB laser, the semiconductor DBR laser can be fabricated by means of a single planar epitaxial growth sequence.⁴⁻⁶

Of the optically⁷ and electrically^{4-6,8-11} pumped DBR lasers fabricated to date, we choose to analyze the large optical cavity (LOC) design first proposed and demonstrated by Wang et al.^{2,8} This configuration is completely amenable to batch planar processing and may, as will be shown, be designed to operate at pump current thresholds of less than 1000 amp/cm². Within certain parameter constraints (e.g., minimum practical or "comfortable" active and waveguide epilayer thicknesses), an LOC DBR laser design is developed that simultaneously maximizes the external quantum efficiency of the device and provides for single transverse and longitudinal mode operation over a continuous-wave optical output power range of 5 to 50 mW.

B.2 BASIC DESIGN CONSIDERATIONS

A cross section through the DBR laser cavity to be analyzed is shown in Fig. B-1(a). The central portion of the device, the active region, is electrically pumped and experiences gain. The two end regions of the device, the passive waveguiding regions, accommodate the distributed Bragg reflectors (DBRs) and are designed to be transparent to the radiation emitted by the active region. In order to achieve efficient, single-longitudinal-mode operation, one DBR must bear low reflectivity for optimal output coupling and the other DBR must bear narrow bandwidth and high reflectivity for single-mode, single-ended emission. Hybrid Fabry-Perot/DBR laser configurations wherein one reflector is a crystal facet are not considered, either because of the difficulty involved in optimally adjusting the reflectivity of a cleaved facet (assuming the DBR served as the high-reflectivity narrow bandwidth reflector) or because of the lack of spectral selectivity associated with low-reflectivity DBRs (assuming the cleaved facet were coated for high reflectivity).

The DBR laser configuration shown in Fig. B-1(a) may be analyzed by considering the formally equivalent structure shown in Fig. B-1(b).⁷ Here, the DBRs are replaced by discrete narrow-bandwidth mirrors bearing frequency-dependent complex reflectivities

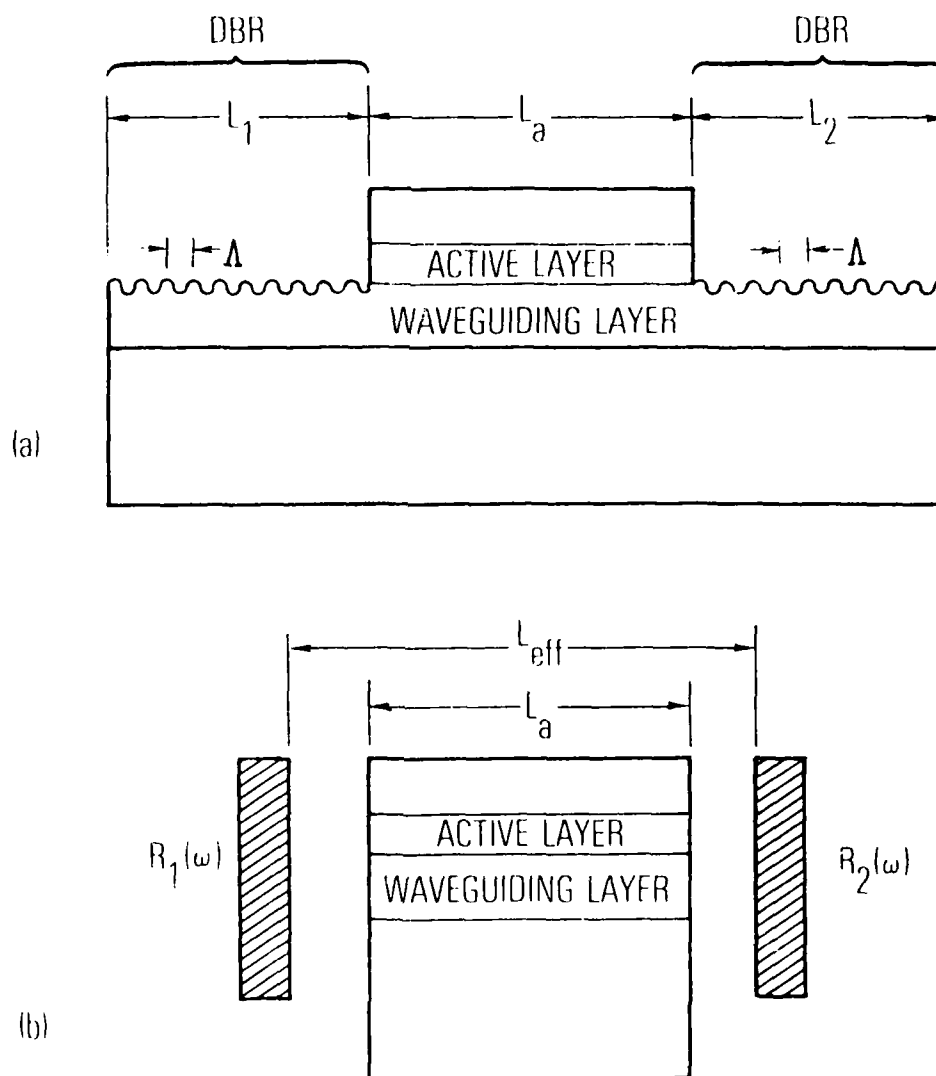


Fig. B-1. DBR Laser. (a) Cross section. (b) Discrete-component analog of DBR laser cavity.

$$R_{1,2}(\omega) = r_{1,2}(\omega) \exp [i\phi_{1,2}(\omega)] \quad (\text{B-1})$$

With Eq. (B-1) and accounting for active-to-passive region coupling losses by inclusion of the coupling factor $f(<1)$, the DBR laser mode spectra and threshold gains are found in the usual manner by setting the net round-trip cavity gain equal to unity or

$$f^4 r_1 r_2 \exp [i(\phi_1 + \phi_2 - 2\beta L_a)] \exp [2(g_{th} - \alpha_a) L_a] = 1 \quad (\text{B-2})$$

where g_{th} and α_a are the distributed amplitude gain and loss coefficients, respectively, of the active region, L_a is the length of the active region, and β is the propagation constant of an oscillation mode. The fourth power exponent of f in Eq. (B-2) is justified by noting that each encounter with a DBR by a wave circulating within the laser cavity results in a net coupling efficiency of f^2 : one factor of f for active-to-passive traversal and one factor of f , by reciprocity, for passive-to-active reentry. The meaning of L_{eff} , the effective cavity length in Fig. B-1(a), will be explained in Section B.5. From Eq. (B-2), it is evident that basic DBR laser design considerations involve both adjustment of the active-passive confinement structure in order to maximize f and minimize g_{th} and adjustment of $R_{1,2}$ to achieve optimally coupled single-mode emission.

B.3 DBR

The DBR consists of a periodically perturbed section of waveguide designed to effect, as a result of backward Bragg scattering, retroreflection of an incident wave.¹² In our analysis, we assumed the geometry of Fig. B-1(a), wherein the DBR consists of a periodically deformed (or corrugated) section of waveguiding medium. The amplitude transmittivity T and amplitude reflectivity R of such a structure may be found by means of the coupled mode theory.¹³ Accordingly,

$$T = \frac{\gamma \exp [-i(\beta - \Delta\beta)L]}{(\alpha_p + i\Delta\beta) \sinh(\gamma L) + \gamma \cosh(\gamma L)} \quad (\text{B-3})$$

and

$$R = \frac{-i \kappa \sinh(\gamma L)}{(\alpha_p + i\Delta\beta) \sinh(\gamma L) + \gamma \cosh(\gamma L)} \quad (B-4)$$

where α_p is the distributed loss coefficient in the waveguiding (passive) region, L is the DBR length, κ is the corrugation coupling coefficient, ^{12,14} $\gamma^2 = \kappa^2 + (\alpha_p + i\Delta\beta)^2$, and $\Delta\beta$ is the measure of deviation from exact satisfaction of the Bragg condition given by

$$\Delta\beta = \frac{\omega - \omega_0}{v} \equiv \beta - \frac{m\pi}{\Lambda} \quad (B-5)$$

where v is the phase velocity of light within the DBR, $m = 1, 2, 3, \dots$ is the Bragg scattering order, and Λ is the period of the surface corrugation.

The magnitude r and the phase ϕ of R are plotted as functions of $\Delta\beta L$ in Figs. B-2 and B-3 for several combinations of the attenuation and coupling parameters $\alpha_p L$ and κL . The principal effects of attenuation within the DBR are a reduction in the line center ($\Delta\beta L = 0$) reflectivity magnitude and less distinct reflectivity sidelobes. In addition, note that in all cases, the reflectivity phase varies almost linearly with $\Delta\beta L$ over the central reflectivity lobe. For small $\Delta\beta L$, the latter observation permits us to approximate ϕ by

$$\phi = -\frac{\pi}{2} - \left\{ \frac{1}{[\alpha_p + (\kappa^2 + \alpha_p^2)]^{1/2} L} \right\} \Delta\beta L \quad (B-6)$$

for $|\gamma L| \gtrsim 2$ or by

$$\phi = -\frac{\pi}{2} - \left(\frac{1}{\alpha_p L + 1} \right) \Delta\beta L \quad (B-7)$$

for $|\gamma L| \lesssim 0.5$.

Design optimization (Section B.5) requires knowledge of the DBR amplitude reflectivity bandwidth $B = \text{FWHM of } r(\Delta\beta L)$, line center power

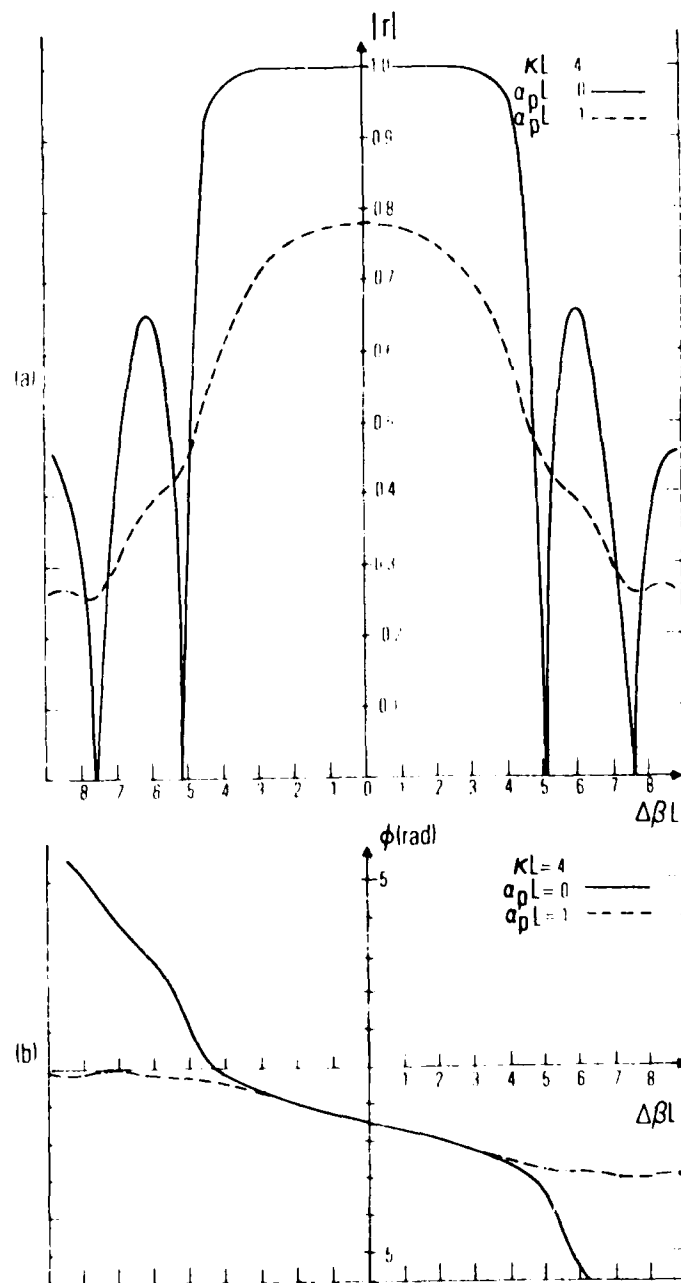


Fig. B-2. DBR. (a) Amplitude reflectivity r as function of deviation ($\Delta\beta L$) from Bragg scattering condition. (b) Reflectivity phase ϕ plotted as function of deviation from Bragg condition.

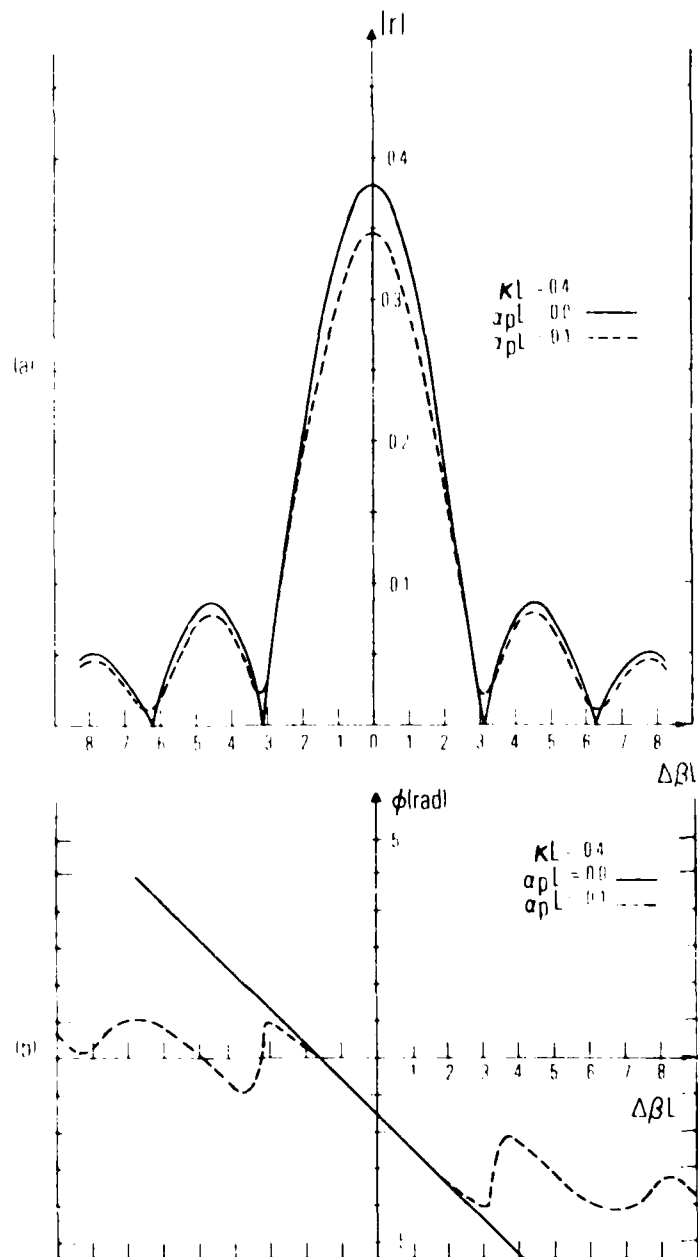


Fig. B-3. DBR. (a) Amplitude reflectivity r plotted as function of deviation ($\Delta\beta L$) from the Bragg scattering condition. (b) Reflectivity phase ϕ plotted as function of deviation from the Bragg condition.

reflectivity $\mathcal{R} = R^2(0)$, and line center power transmittivity $\mathcal{T} = T^2(0)$. Line center values for \mathcal{R} and \mathcal{T} are chosen for convenience; justification for their use is made in Section B.5. Figure B-4(a) is a parametric plot of \mathcal{B} as a function of both $\alpha_p L$ and κL . Figure B-4(b) is a composite plot of both \mathcal{R} and \mathcal{T} as functions of $\alpha_p L$ and κL . For arbitrary values of $\alpha_p L$ and κL , the latter plot can be used to calculate the total distributed loss within a given DBR = $1 - \mathcal{R} - \mathcal{T}$.

B.4 ACTIVE-PASSIVE COUPLING FACTOR

A cross section through the interface that separates the active region of a DBR laser from one of its DBRs is shown in Fig. B-5. The active region is comprised of five epitaxially grown GaAlAs layers, which together form a localized gain region (LGR) or large optical cavity (LOC) laser structure.¹⁵ The transverse field distribution of the active region mode is assumed to be defined by the upper cavity, active, waveguide, and isolation layers and to be concentrated primarily within the active and waveguiding epilayers. The passive region, within which the distributed Bragg reflectors reside, is formed by removing the cap, upper cavity, and (highly absorptive) active layers from the active region.⁸ The transverse field distribution within the passive region is determined by the superstrate (assumed to be air) and by the waveguide and isolation epilayers.

As accounted for by the f^4 factor in Eq. (B-1), different active and passive transverse field distributions result in incomplete optical coupling between active and passive regions of the DBR laser. The active passive coupling factor f can be found in a straightforward way by considering the field radiated into the passive region by the lowest order active region mode incident at the active passive interface (it is assumed that the active and passive regions each support only one confined mode). The lowest order active region mode $\epsilon_a^{(o)}(x)$ is first expressed as an expansion over the orthonormal passive region mode set as follows:

$$\epsilon_a^{(o)}(x) = f \epsilon_p^{(o)}(x) + \int_v D_v \epsilon_p^{(v)}(x) dv \quad (B-8)$$

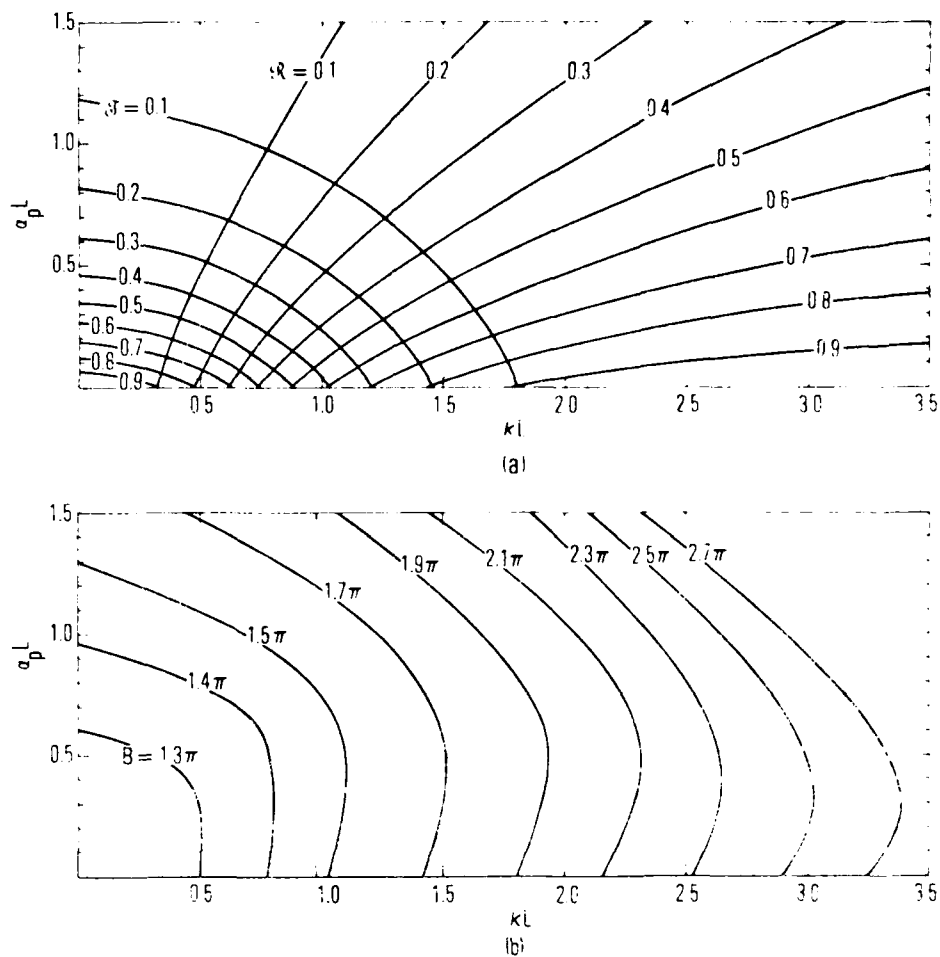


Fig. B-4. DBR Parametric Plots. (a) Power transmittivity T and power reflectivity R as functions of DBR loss αL and coupling κL parameters. (b) Amplitude reflectivity bandwidth B , FWHM of r ($\Delta\beta L$), as functions of DBR loss and coupling parameters.

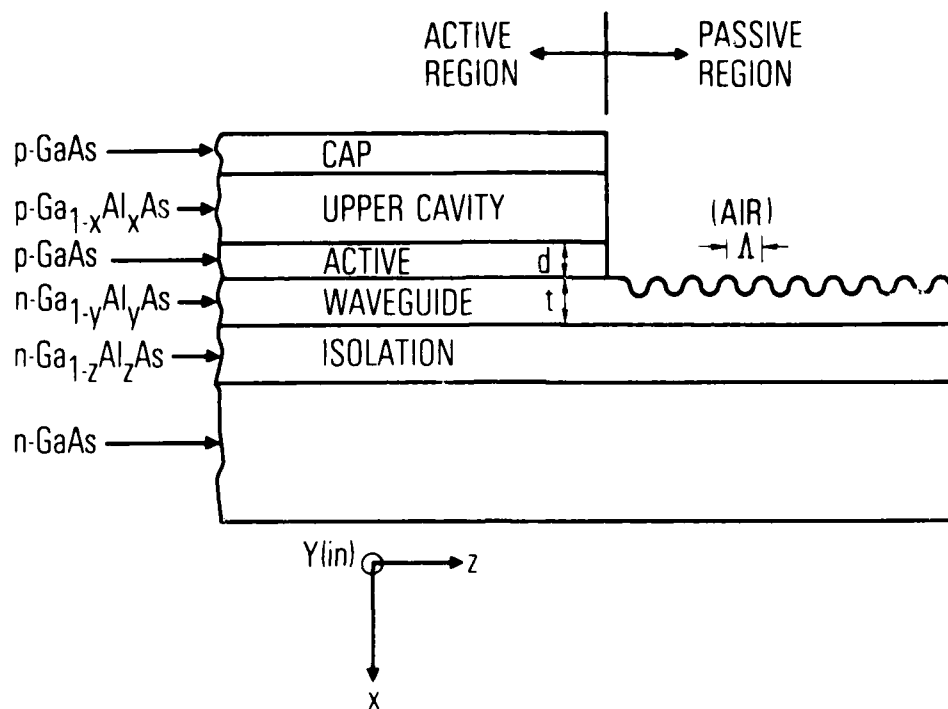


Fig. B-5. Cross Section Through LOC DBR Laser Active-Passive Region Interface

where $\epsilon_p^{(0)}(x)$ is the lowest-order passive region confined mode, $\epsilon_p^{(v)}(x)$ represents the continuum of passive region radiation modes, and f and D_v are expansion coefficients. With the use of the orthonormality of the passive region eigenmode set, Eq. (B-8) is then manipulated to yield for the coupling factor

$$f = \int_{-\infty}^{\infty} \epsilon_a^{(0)}(x) \epsilon_p^{(0)}(x) dx \quad (B-9)$$

In deriving Eq. (B-9), it has been assumed that all modes are transverse electric (TE) polarized (electric field vector aligned parallel to the y-direction); extension to the transverse magnetic (TM) case is obvious and will not be considered here.

The (TE) field distributions in the active and passive regions are found by solving the scalar wave equation and requiring continuity of the tangential electric and magnetic fields at the various epilayer interfaces (Fig. B-5). Taking the origin of the x-axis to be at the upper cavity active layer interface, the active region confined mode field distribution is given by

$$\epsilon_{(a)}^{(m)}(x) = \begin{cases} C_1 \left[\frac{h}{q} \exp(qx) \right] & (x \leq 0) \\ C_1 \left[\sin(hx) + \frac{h}{q} \cos(hx) \right] & (0 \leq x \leq a) \\ C_1 \left\{ \left[\sin(ha) + \frac{h}{q} \cos(ha) \right] \cos(x-a)\ell \right. \\ \quad \left. + \frac{h}{\ell} \left[\cos(ha) - \frac{h}{q} \sin(ha) \right] \sin(x-a)\ell \right\} & (a \leq x \leq a+t) \\ C_1 \left\{ \left[\sin(ha) + \frac{h}{q} \cos(ha) \right] \cos(t\ell) \right. \\ \quad \left. + \frac{h}{\ell} \left[\cos(ha) - \frac{h}{q} \sin(ha) \right] \sin(t\ell) \right\} \times \exp[-p(x-a-t)] & \end{cases} \quad (B-10)$$

where $m = 0, 1, 2, \dots$ is the mode index number and the transverse q, h, ℓ, p , longitudinal β , and free space $k_o = 2\pi/\lambda_o$ propagation constants are related to one another by

$$n_1^2 k_o^2 = \beta^2 - q^2 \quad (B-11a)$$

$$n_2^2 k_o^2 = \beta^2 + h^2 \quad (B-11b)$$

$$n_3^2 k_o^2 = \beta^2 + \ell^2 \quad (B-11c)$$

$$n_4^2 k_o^2 = \beta^2 - p^2 \quad (B-11d)$$

and

$$h \left[\frac{q - h \tan(ha)}{h + q \tan(ha)} \right] = -\ell \left[\frac{p - \ell \tan(\ell t)}{\ell + p \tan(\ell t)} \right] \quad (B-11e)$$

Similarly, for the three-layer passive region:

$$\epsilon_{(n)}^{(m)}(x) = \begin{cases} C_2 \exp[u(x-a)] & (x \leq a) \\ C_2 \left\{ \cos[r(x-a)] + \frac{u}{r} \sin[r(x-a)] \right\} & (a \leq x \leq a+t) \\ C_2 \left[\cos(rt) + \frac{1}{r} \sin(rt) \right] \exp[v(a+t-x)] & (a+t \leq x) \end{cases} \quad (B-12)$$

where

$$k_o^2 = \beta^2 - u^2 \quad (B-13a)$$

$$n_3^2 k_o^2 = \beta^2 + r^2 \quad (B-13b)$$

$$n_4^2 k_o^2 = \beta^2 - v^2 \quad (B-13c)$$

and

$$\tan (rt) = \frac{(u/r) + (v/R)}{1 - (u/r)(v/r)} \quad (B-13d)$$

Finally, the normalization constants, C_1 and C_2 are chosen so that

$$\int_{-\infty}^{\infty} \left[\varepsilon_{(a)}^{(m)}(x) \right]^2 dx = \int_{-\infty}^{\infty} \left[\varepsilon_{(p)}^{(m)}(x) \right]^2 dx \approx 1 \quad (B-14)$$

B.5 DESIGN OPTIMIZATION

The DBR laser operational characteristics are governed by Eq. (B-2). Solution of Eq. (B-2) yields for the propagation constants β_{ℓ} and threshold gains g^{th} of the DBR laser

$$\begin{aligned} \beta_{\ell} &= \Delta\beta_{\ell} + \frac{m\pi}{\Lambda} \\ &= \frac{1}{2L_a} (\phi_1 + \phi_2) + \frac{\ell\pi}{L_a} \end{aligned} \quad (B-15)$$

and

$$g_{\ell}^{\text{th}} = \alpha_a - \frac{1}{2L_a} \log \left[f^4 r_1 r_2 \right] \quad (B-16)$$

where $\ell = 0, \pm 1, \pm 2, \dots$ is the longitudinal mode index and $\Delta\beta_{\ell}$ the deviation from exact satisfaction of the Bragg condition for the ℓ th longitudinal mode. Moreover, from Eqs. (B-6), (B-7), and (B-10), the longitudinal mode spacing is given to good approximation by

$$\Delta \equiv \left| \beta_{\ell} - \beta_{\ell \pm 1} \right| = \frac{\pi}{L_{\text{eff}}} \quad (B-17)$$

where the effective laser cavity length L_{eff} is given by

$$L_{\text{eff}} = L_a \left\{ 1 + \frac{L_2}{2L_a(\alpha_p L_2 + 1)} + \frac{1}{2L_a \left[\alpha_p + (\kappa^2 + \alpha_p^2) \right]} \right\} \quad (B-18)$$

In Eq. (B-18), L_1 and L_2 are the lengths of the left-hand and right-hand, respectively, DBRs, and power extraction is assumed to occur from the right-hand low-reflectivity DBR.

Design optimization requires single transverse and longitudinal mode operation. Operation in a single transverse mode in the y-direction [refer to Fig. (B-5)] may be achieved by appropriate adjustment of the DBR laser lateral (stripe) dimension; lateral mode control in the x-direction (perpendicular to the junction plane) will be seen to result automatically from our attempts to maximize the external quantum efficiency of the device. Restriction to oscillation in a single longitudinal mode requires that the intermode spacing, defined by Eq. (B-12), be equal to or greater than the net reflectivity bandwidth of the laser cavity. While the latter quantity is accurately defined as being equal to the FWHM of $r_1 \cdot r_2$, out of convenience, we shall use the FWHM of r_1 instead. Our assumption that the cavity bandwidth is governed by the high-reflectivity DBR is justified by the fact that in all cases of interest the FWHM of r_2 is considerably greater than the FWHM of r_1 .

The DBR design parameters required for single longitudinal mode operation can be found graphically [Figs. B-4(a) and B-4(b)]. We assume that the Bragg condition has been exactly satisfied for the longitudinal mode of interest (this may be accomplished, for example, by thermally varying the laser cavity length L_a in such a way that $\Delta\beta = 0$). Certain line-center DBR reflectivities $r_1 = [\mathcal{R}_1(0)]^{1/2}$ and $r_2 = [\mathcal{R}_2(0)]^{1/2}$ are then assumed and their corresponding parametric curves in Fig. B-4(a) noted as representing the loci of all possible design solutions. Specific design solutions are found by examining the intersections of these curves with straight lines corresponding to fixed values of α_p and κ . The intersection points yield values of L_1 and L_2 that can then be used, with the aid of Fig. B-4(b) and Eqs. (B-17) and (B-18), to compute the longitudinal mode spacing Δ and the FWHM of r_1 . Once Δ has been found to be greater than or equal to the FWHM of r_1 , the design problem will have been solved.

As initial assumptions, we take for the high-reflectivity DBR, $r_1 = 0.95$ (or $\mathcal{R}_1 = 0.9$), and for the low-reflectivity DBR, $r_2 = 0.45$ (or $\mathcal{R}_2 = 0.2$). The (lower bound) value chosen for r_1 reflects our wish to induce efficient single-ended laser emission. The (upper bound) value chosen for r_2 anticipates the effects of a high active region gain on later attempts to maximize the external quantum efficiency of the laser. Parametric curves for $\mathcal{R}_1 = 0.9$ and $\mathcal{R}_2 = 0.2$ are shown, together with representative DBR bandwidth curves, in Fig. B-6 as functions of $\alpha_p L$ and κL . Solutions to the design problem are found by examining the common intersections of these two sets of curves with the straight lines that correspond to fixed values of α_p and κ . The straight lines, also shown in Fig. B-6, pass through the origin and to bear slopes of α_p / κ . Throughout our analysis, we shall assume that $\alpha_p = 1 \text{ cm}^{-1}$ and that κ is the same for both DBRs. The value chosen for α_p represents a lower bound for GaAlAs waveguide attenuation coefficients;¹⁶ the assumption that κ remains the same for both DBRs simplifies considerably the actual DBR laser fabrication process.

With $\alpha_p = 1 \text{ cm}^{-1}$, $L_a = 300 \text{ }\mu\text{m}$, and, as an initial estimate, $\kappa = 20 \text{ cm}^{-1}$, we find from Fig. B-6 and Eq. (B-18) that $L_1 = 1.47 \text{ mm}$, $L_2 = 240 \text{ }\mu\text{m}$, and $L_{\text{eff}} = 660 \text{ }\mu\text{m}$, thereby yielding for the longitudinal mode spacing, 48 cm^{-1} , and, for the high reflectivity DBR bandwidth, 54 cm^{-1} . Since in this case, the mode spacing is less than the high-reflectivity DBR bandwidth, either L_a or κ must be adjusted in order to achieve single longitudinal mode operation. Increasing κ worsens the situation, whereas a decrease in κ requires progressively longer (and more lossy) reflector lengths in order to achieve the same amplitude reflectivity (0.95). A satisfactory solution to the problem results from setting $\kappa = 20 \text{ cm}^{-1}$ and $L_a = 275 \text{ }\mu\text{m}$, in which case $L_1 = 1.47 \text{ mm}$, $L_2 = 240 \text{ }\mu\text{m}$, $L_{\text{eff}} = 501 \text{ }\mu\text{m}$, and the intermode spacing and DBR bandwidths both equal 54 cm^{-1} . Note that, in order to achieve single-mode single-ended laser operation, it has been necessary to adjust all previously free-cavity parameters.

Having determined the DBR coupling coefficient and cavity length parameters required in order to achieve efficient single longitudinal mode operation, we now concentrate on maximizing the DBR external quantum

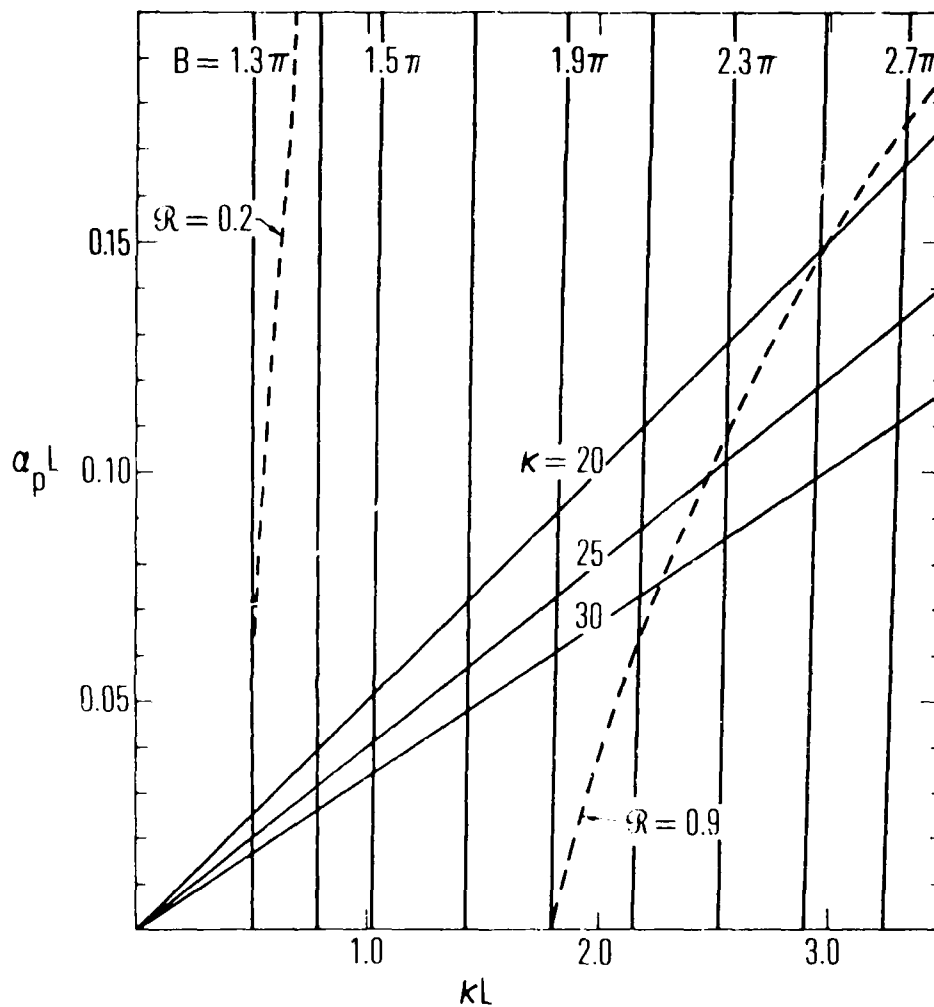


Fig. B-6. Composite of Figs. 4(a) and 4(b) with Constant κ Lines Overlaid

efficiency of the laser by appropriate adjustment of the epilayer thicknesses and compositions of the device. The external quantum efficiency is maximized by minimizing the pump current density required in order to achieve a given continuous-wave optical output power.

Thompson et al.¹⁷ derived an empirical expression (since derived theoretically by Casey¹⁸) for the threshold gain of lasers bearing active regions similar to those under consideration. Their expression is

$$g_{th} = \frac{\nu}{28} \left(\frac{J_{th}}{d} - 4000 \right) \quad (B-19)$$

where J_{th} is the threshold current density (amp/cm²), d is the thickness of the active region (μ m), and ν is a filling factor equal to the fraction of laser mode energy that occupies the active layer,

$$\nu = \int_0^d \left[\epsilon_a^{(o)}(x) \right]^2 dx \quad (B-20)$$

The threshold current density is found, by simultaneous solution of Eqs. (B-16) and (B-19), to be

$$J_{th} = 4000 d + \frac{28}{\nu} \left[\alpha_a - \frac{1}{2 L_a} \log (f^4 r_1 r_2) \right] \quad (B-21)$$

The pump current density J_p required in order to achieve a given optical power output P_o is related to J_{th} by

$$J_p = J_{th} + \frac{P_o}{A E_g \Gamma \eta_i} \quad (B-22)$$

where A (cm²) is the area pumped, η_i is the internal quantum efficiency, E_g (V) is the active region bandgap and Γ the ratio of useful to total loss suffered per round trip cavity pass, is

$$\Gamma = \left[\frac{\ln (r_1 r_2)}{\ln f^4 r_1 r_2 - 2 \alpha_a L_a} \right] \left(\frac{\mathcal{F}^2}{2 - \mathcal{R}_1 - \mathcal{R}_2} \right) \quad (B-23)$$

In deriving Eq. (B-22), small ohmic losses occasioned by electrical contacts and bulk resistivity have been ignored. In Eq. (B-23), the first term on the right-hand side accounts for useful power coupled outside the active region; the second term accounts for imperfect (i.e., <100%) reflectivity by the high-reflectivity DBR and for distributed losses suffered as a result of passage through both DBRs.

For a given optical output power P_o , the pump current density J_p was minimized by varying the following parameters: the active layer thickness d , the waveguide thickness t , the refractive index of the upper cavity layer n_1 , the refractive index of the active layer n_2 , the refractive index of the waveguide layer n_3 , the refractive index of the isolation layer n_4 , and the amplitude reflectivity of the output DBR r_2 . Throughout the analysis, it was assumed that λ_o (the oscillation wavelength) = $0.9 \mu\text{m}$, w (the laser stripe width) = $10 \mu\text{m}$, $E_g = 1.38 \text{ V}$, $\alpha_a = 9 \text{ cm}^{-1}$ (18), and $n_i = 0.9$.¹⁸ The refractive indices of various layers were obtained using the data of Casey et al.¹⁹ In addition, the following constraints were placed on the parameters varied: (1) that the active layer thickness be no less than $0.05 \mu\text{m}$, (2) that the active layer contain 0.05 mole fraction AlAs, (3) that the difference in AlAs mole fraction between the active and waveguiding layers be no less than 0.06, and (4) that the AlAs mole fractions of the upper cavity and isolation be no more than 0.5. In the first constraint the limitations of state-of-the-art liquid-phase epitaxy were recognized,²⁰ in the second constraint, the need for strain relief between the active and contiguous epilayers was recognized,²¹ the third constraint ensured reasonable transparency of the waveguide layer at $0.9 \mu\text{m}$,²² and the fourth constraint indirectly prevented the waveguide layer from becoming inconveniently thin.²³

The epilayer parameters referred to above were varied sequentially until J_p reached a minimum, either as a result of parameter tradeoffs or as a result of a particular parameter reaching one of the enumerated constraints. Remarkable design consistency was evidenced over the entire optical output range considered ($P_o = 5$ to 50 mW). In all cases, J_p reached a local minimum for a waveguide thickness of $0.225 \mu\text{m}$ and, simultaneously, was minimized as each of the other epilayer parameters reached their limiting values.

In Fig. B-7, both J_p and J_{th} are plotted as functions of t for $P_o = 50$ mW. The limiting (optimal) values of the remaining epilayer parameters, which were held constant as t was varied, are also listed. In addition, the values of r_2 required in order to minimize J_p for a given waveguide thickness are shown above the J_{th} curve. The minimum value of J_p , obtained just prior to waveguide cutoff (at $t = 0.15 \mu m$), is understood to occur as a result of tradeoffs between the filling factor v and the coupling factor f . The latter situation is illustrated in Fig. B-8 wherein v is seen to decrease monotonically with t , while f is seen to increase monotonically with t . Optimal values of v and f are noted, from Figs. B-7 and B-8, to be 0.113 and 0.814, respectively.

The fact that J_p is simultaneously minimized as the remaining epilayer parameters reach their limiting values is seen to result both from the strong dependence of J_{th} on the active layer thickness d , Eq. (B-16), and from enhancement of the active-to-passive coupling factor f . The latter effect occurs both because of improved mode confinement within the active and passive regions (induced by higher AlAs mole fractions in the upper cavity and isolation confinement layers) and because of improved mode matching between the active and passive regions (induced as a result of the waveguide AlAs mole fraction approaching that of the active layer).

In Fig. B-9, plots J_p , J_{th} , and r_2 are plotted as functions of P_o , and the results of our design analysis are summarized. A list of the optimal epilayer parameters is given in Fig. B-9; the coupling coefficient and cavity length parameters used were those derived in Section B.3. If bulk and electrical contact losses are ignored as before, the external quantum efficiency ranges from 14.1% for $P_o = 5$ mW to 57.8% for $P_o = 50$ mW. Also, note that $J_{th} < 1000$ amp/cm over the entire optical output range considered.

B.6 CONCLUSION

Within certain practical design constraints, optimal DBR laser designs have been developed that permit single-mode single-ended operation over a 5 to 50 mW continuous-wave optical output power range. It has been determined that only the reflectivity (or length) of the output DBR need be

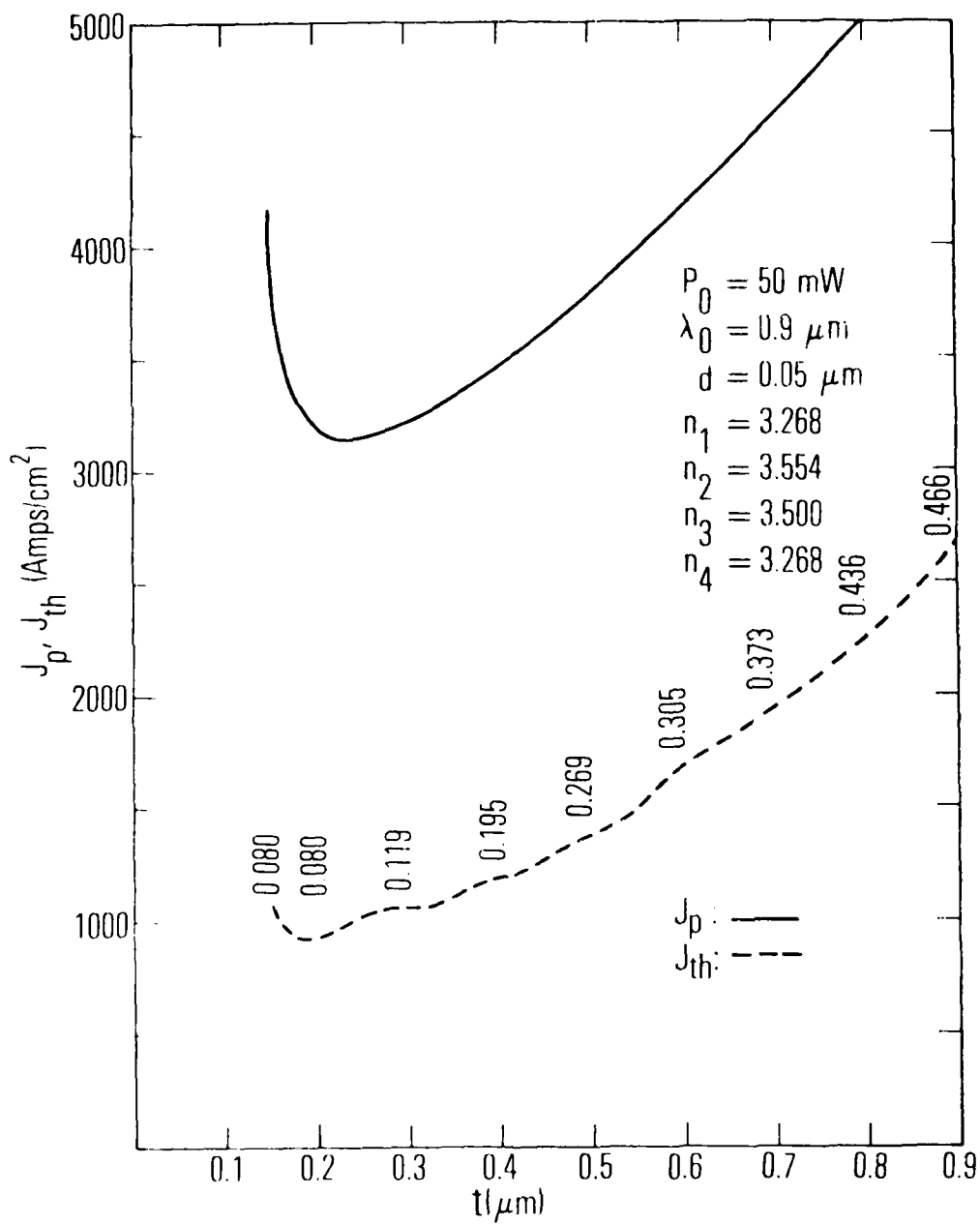


Fig. B-7. Threshold and Pump-Current Densities Plotted as Function of Waveguiding Layer Thickness for Optical Output Power of 50 mW

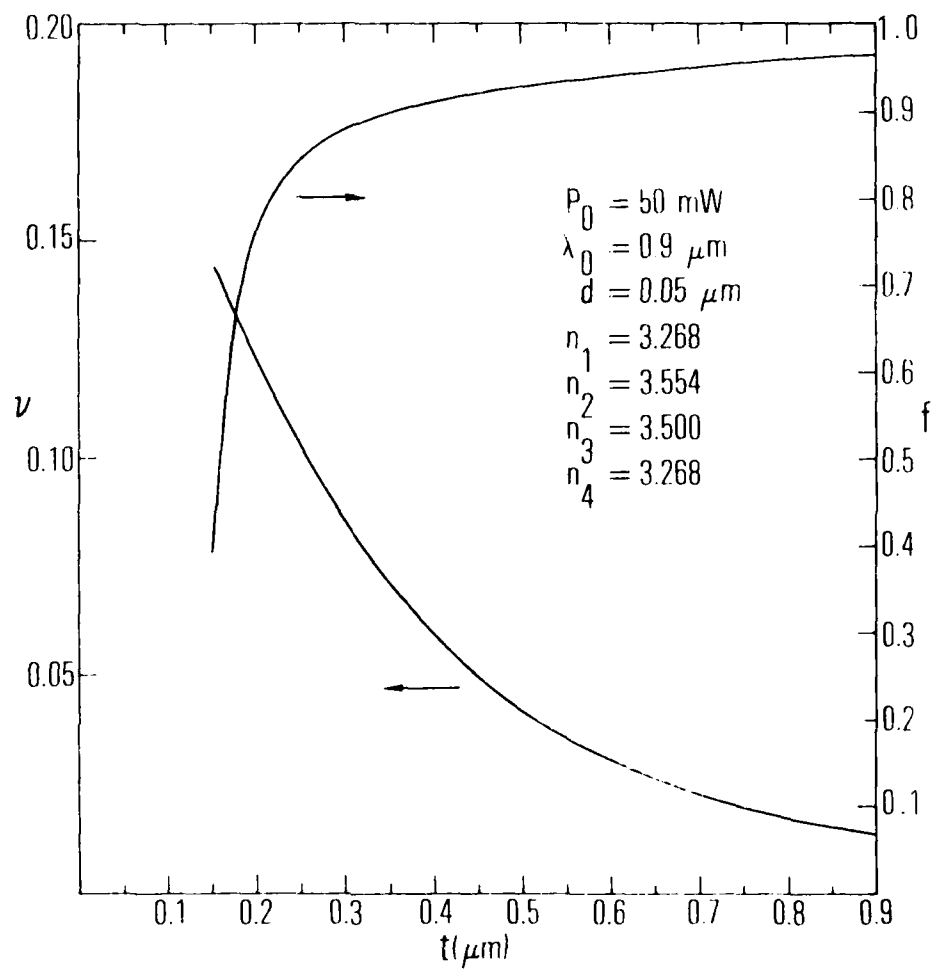


Fig. B-8. Active Region Filling Factor ν and Active-Passive Coupling Factor f Plotted as Functions of Waveguiding Layer Thickness for Optical Output Power of 50 mW

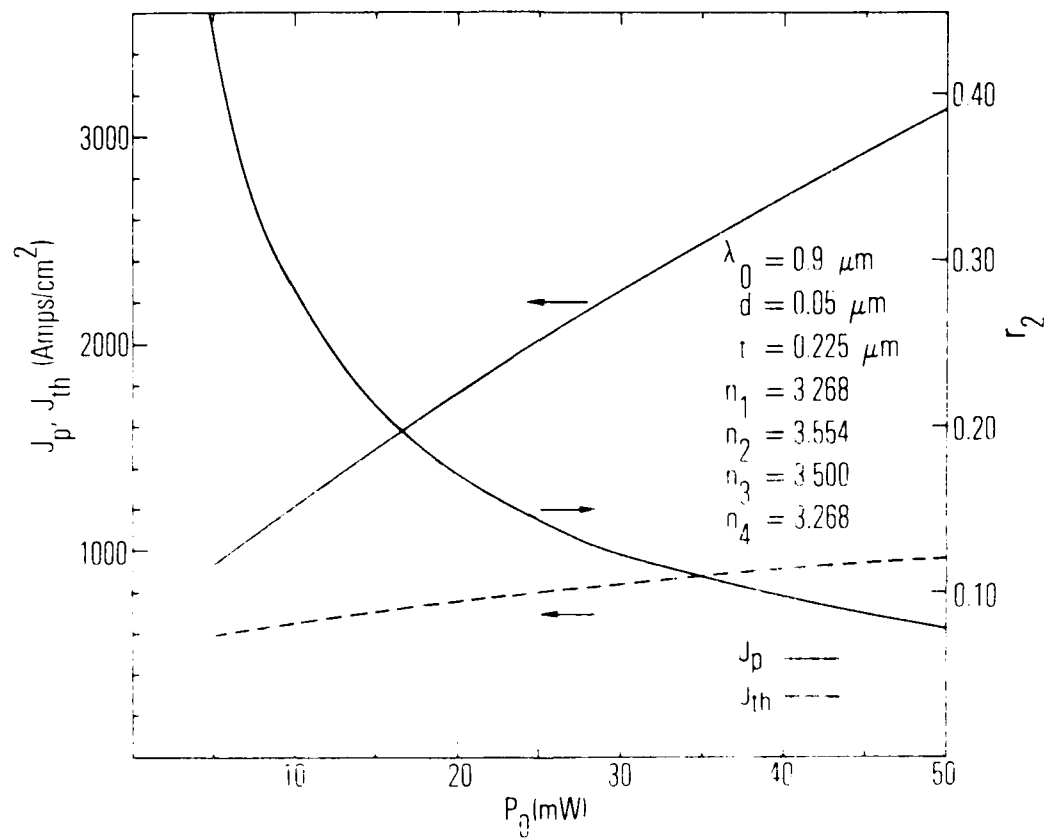


Fig. B-9. Threshold and Pump-Current Densities (left ordinate) and Output DBR Amplitude Reflectivity (right ordinate) Plotted as Functions of Optical Output Power for Optimized DBR Laser Structure

varied in order to achieve optimal output coupling over the optical power range of interest. With an internal quantum efficiency of 90% assumed, external quantum efficiencies have been found to range from 14.1% (5-mW output) to 57.8% (50-mW output), with threshold current densities never exceeding 1000 amp/cm².

APPENDIX B REFERENCES

1. H. Kogelnik and C. V. Shank, "Stimulated Emission in a Periodic Structure," Appl. Phys. Lett. 18 152-154 (1971).
2. S. Wang, "Principles of Distributed Feedback and Distributed Bragg-Reflector Lasers," IEEE J. Quantum Electron. QE-10, 413-427 (1974).
3. M. Nakamura, K. Aiki, J. Umeda, A. Katzir, A. Yariv, and H. W. Yen, "GaAs-(GaAl)As Double-Heterostructure Injection Lasers with Distributed Feedback," IEEE J. Quantum Electron. QE-11, 436-439 (1975).
4. F. K. Reinhart, R. A. Logan, and C. V. Shank, "GaAs-(AlGa)As Injection Lasers with Distributed Bragg Reflectors," Appl. Phys. Lett. 27, 45-48 (1975).
5. W. T. Tsang and S. Wang, "GaAs-(GaAl)As Double-Heterostructure Injection Lasers with Distributed Bragg Reflectors," Appl. Phys. Lett. 28, 596-598 (1976).
6. W. Ng, H. W. Yen, A. Katzir, I. Samid, and A. Yariv, "Room Temperature Operation of GaAs Bragg-Mirror Lasers," Appl. Phys. Lett. 29, 684-686 (1976).
7. H. W. Yen, W. Ng, I. Samid, and A. Yariv, "GaAs Distributed Bragg Reflector Lasers," Opt. Comm. 17, 213-218 (1977).
8. H. Namizaki, M. K. Shams, and S. Wang, "Large-Optical-Cavity GaAs-(GaAl)As Injection Laser with Low-Loss Distributed Bragg Reflectors," Appl. Phys. Lett. 31, 122-124 (1977).
9. W. Ng and A. Yariv, "Highly Collimated Broadside Emission from Room-Temperature GaAs Distributed Bragg Reflector Lasers," Appl. Phys. Lett. 31, 613-615 (1977).
10. Zh. I. Alferov, S. A. Gurevich, M. N. Misarov, and E. L. Portnoy, "CW (AlGa)As Injection Heterostructure Laser with Second-Order Distributed Bragg Reflectors," presented at Topical Meeting on Integrated and Guided Wave Optics, Salt Lake City, Utah, January 1978.
11. H. Kawanishi, Y. Suenatsu, Y. Itoya, and S. Arai, "(GaIn) (AsP)/InP Injection Laser with Distributed Bragg Reflector," presented at 1978 IEEE International Semiconductor Laser Conference, San Francisco, California, November 1978.

12. H. Stoll and A. Yariv, "Coupled Mode Analysis of Periodic Dielectric Waveguides," Opt. Comm., 8, 5-8 (1973).
13. A. Yariv and H. W. Yen, "Bragg Amplification and Oscillation in Periodic Optical Media," Opt. Comm., 10, 120-122 (1974).
14. W. Streifer, D. R. Scifres, and R. D. Burnham, "Coupling Coefficients for Distributed Feedback Single- and Double-Heterostructure Diode Lasers," IEEE J. Quantum Electron. QE-11, 867-873 (1975).
15. G. H. B. Thompson and P. A. Kirkby, "(GaAl)As Lasers with a Heterostructure for Optical Confinement and Additional Heterostructure for Extreme Carrier Confinement," IEEE J. Quantum Electron. QE-9, 311-318, (1973); H. C. Casey, M. B. Panish, W. O. Schlosser, and T. L. Paoli, "GaAs-(AlGa)As Heterostructure Laser with Separate Optical and Carrier Confinement," J. Appl. Phys. 45, 322-333 (1974).
16. F. A. Blum, D. W. Shaw, and W. C. Holton, "Optical Striplines for Integrated Optical Circuits in Epitaxial GaAs," Appl. Phys. Lett. 25, 116-228 (1974).
17. G. H. B. Thompson, G. D. Henshall, J. E. A. Whiteaway, and P. A. Kirkby, "Narrow-Beam Five-Layer (GaAl)As/GaAs Heterostructure Lasers with Low Threshold and High Peak Power," J. Appl. Phys., 47, 1501-1514 (1976).
18. H. C. Casey, Jr., "Room-Temperature Threshold-Current Dependence of GaAs-(AlGa)As Double-Heterostructure Lasers on X and Active-Layer Thickness," J. Appl. Phys. 7, 3684-3692 (1978).
19. H. C. Casey, Jr., D. D. Sell, and M. B. Panish, "Refractive Index of (AlGa)As Between 1.2 and 1.8 eV," Appl. Phys. Lett. 24, 63-65 (1974).
20. R. D. Dupuis, P. D. Dapkus, R. M. Kolbas, N. Holnyak, Jr., and H. Shichijo, "Photopumped Laser Operation of Mo-CVD (AlGa)As Near a GaAs Quantum Well (λ 6200 Å, 77°K)," Appl. Phys. Lett. 33, 596-598 (Oct. 1978).
21. Y. Nannichi, and I. Hayashi, "Degradation of (GaAl)As Double Heterostructure Diode Lasers," J. Cryst. Growth, 27, 125-132 (1974).
22. S. Wang, "Design Considerations of the DBR Injection Laser and the Waveguiding Structure for Integrated Optics," IEEE J. Quantum Electron. QE-13 (1977).

APPENDIX C

DBR AND ACTIVE-PASSIVE LASER FABRICATION PROCEDURE

C.1 SAMPLE EXAMINATION

1. Etch sample in 1:1:8 A-B etch (A:B:H₂O mp) for 5 sec.
2. Photograph all four corners of sample to determine cap thickness variations.

C.2 CAP LAYER REMOVAL

1. Soak clean sample in warm (>60°C) trichlorethylene for 2 to 5 min.
2. Rinse sample in dry isopropyl alcohol for 1 to 2 min.
3. Blow sample dry with nitrogen.
4. Dehydration bake sample at 170°C for 30 min.
5. Mount sample on glass microscope slide cover with Apiezon wax.
6. Cool and then whirl clean sample with a one to one mixture of HMDS and AZ thinner.
7. Apply unthinned filtered AZ 1375 to sample.
8. Spin sample at 4000 rpm for 30 sec (resultant photoresist thickness should be approximately 3 μ m).
9. Air dry sample for 15 min.
10. Oven bake sample at 90°C for 20 min. (pre-exposure bake).
11. Use mask GE-2 with mask alignment instrument and expose photoresist for 30 sec.
12. Develop photoresist for 1 min using equal parts Shipley MF 312 developer and deionized water. Rinse sample in deionized H₂O for 60 sec, and blow dry with N.
13. Oven bake sample at 90°C for 20 min (postexposure bake).

14. Remove sample from glass microscope slide cover by heating on hot plate. Rinse sample quickly in xylene at room temperature.
15. Ion beam etch sample to remove cap layer. Mount sample on rotary stage with heat conductive zinc oxide paste. Approximate system settings: 0.500-mA beam current, 500-V acceleration voltage, 7×10^{-5} Torr Ar, (resultant milling rate is approximately 455 Å/min or 22.2 min/μm). Sample should be rotated at 30 deg to the incident ion beam.
16. Check cap layer removal by observing the photoluminescence of the sample.

C.3 TOP BARRIER LAYER REMOVAL

1. Chemically etch sample with A-B etchant, 1:1:4 or 1:1:8 ratio of A, B, and H₂O (millipore), for approximately one min.
2. Check depth of etching with photoluminescence measurements. Repeat Step 1 until cap layer is removed. Check integrity of photoresist after etching.

C.4 ACTIVE LAYER REMOVAL

1. Ion mill sample to remove active layer. Use same parameters as in Section C.2, Step 15. Or, perform Step 2.
2. Chemically etch sample with A-B etchant as in Section C.3, Step 1.
3. Check depth of etching with photoluminescence measurements. Repeat Step 1 or Step 2 until active layer is removed.
4. Remove photoresist from mesas with the plasma line etcher. Use O₂ at maximum power for 20 min.

C.5 DBR GRATING APPLICATION*

1. Soak clean sample in warm (>60°C) trichlorethylene for 2 to 5 min.
2. Rinse sample in dry isopropyl alcohol for 1 to 2 min.

*Omit this section if active-passive devices are desired.

3. Blow dry sample with nitrogen.
4. Dehydration bake sample at 170°C for 30 min.
5. Spray deposit a 1500-Å-thick layer of photoresist (one part AZ 1350B diluted with four parts of AZ thinner) over entire sample. Typical system parameters are a spray duration of 0.125 sec and a spray distance of 11 cm from the sample.
6. Oven bake sample at 65°C for 25 min.
7. Expose the sample with interfering beams of the 4579 Å line of an argon laser. The typical exposure time is about 30 sec for a combined beam intensity of 10 mW/cm². 10 mW/cm² corresponds to an indicated voltage of 0.370 from the solar cell mounted on the stage. The sample is aligned by reflecting a He-Ne beam off of a cleaved face back to the He-Ne laser. Each of the interfering beams should be of equal intensity within 10%. A standing-wave pattern can be observed on the beam-splitting prism. By slightly adjusting both beam angles, the standing-wave pattern can be made symmetrical, indicating both beam angles are symmetric with respect to the normal to the sample.
8. Develop photoresist for 1 sec using equal parts Shipley MF 312 developer and deionized water. Rinse sample in deionized H₂O for 60 sec, and blow dry.
9. Measure the grating periodicity using the ellipsometer. Both first-order Littrow angles are measured to within 20 sec of arc and averaged. The grating orientation with respect to the crystal cleave is simultaneously measured using the rotatable stage mounted on the ellipsometer. The latter measurement is accurate to within 1 min of arc.

If either the grating period or grating orientation is wrong, the photoresist can be removed from the sample with acetone and steps 1 through 9 repeated.
10. Ion beam etch grating into the GaAs. Mount sample on rotary stage with heat conductive SiO₂ paste. Approximate settings are described in Section C.3, Step 15.

C.6

OXIDATION AND STRIPE CONTACT DEFINITION

1. Soak clean sample in warm (<60°C) trichloroethylene for 2 to 5 min.
2. Rinse sample in dry isopropyl alcohol for 1 to 2 min.

3. Blow dry sample with nitrogen.
4. Dehydration bake sample at 170°C for 30 min.
5. Deposit 3000 Å thick SiO₂ layer over entire sample surface.
6. Repeat Steps 1 through 4.
7. Mount sample on glass slide with Apiezon wax.
8. Cool and then whirl clean sample with a 1:1 mixture of HMDS and AZ thinner.
9. Apply unthinned filtered AZ 1350J to sample.
10. Spincoat sample at 5000 rpm for 30 sec.
11. Air dry sample for 15 min.
12. Oven bake sample at 90°C for 25 min.
13. Use mask GE-1 with mask alignment instrument and expose sample for 16 sec. Mask GE-1 consists of a five-row matrix of 25- by 450-µm windows.
14. Develop photoresist for 1 min using equal parts Shipley MF 312 developer and deionized water. Rinse sample in deionized water for 60 sec and blow dry with nitrogen.
15. Oven bake sample at 90°C for 20 min.
16. Etch windows (25 by 450 µm) through the SiO₂ using the plasmaline etcher at maximum power with CF₄ for about 20 min.

C.7.

METALIZATION AND MOUNTING OF INDIVIDUAL DEVICES

1. Clean sample in a boiling mixture of acetone and xylene (1:1) for 3 min. Rinse sample in three changes of hot xylene, and blow dry with nitrogen.
2. Mount sample face down on plating fixture with conductive (Dotite) paint. Coat all conducting areas of the fixture and the sides of the sample with Apiezon solution (Apiezon wax in xylene). Let the Apiezon solution dry.
3. Immerse sample in HCl:H₂O (1:1) for 3 min. Do not rinse. Transfer sample directly to the Pt plating solution. The Pt plating solution is a commercial halite solution.

A current density of $200 \mu\text{A}/\text{mil}^2$ has been established as being an optimum current density for platinum plating in this procedure. The desired thickness of platinum is between 0.2 and 0.3 μm , which takes approximately two min.

4. Overplate the Pt layer with Au using a standard cyanide solution. A current density of $2 \mu\text{amp}/\text{mil}^2$ typically gives a 0.5- μm -thick layer in about 1 min.
5. Repeat Steps 2 with the face of the sample up.
6. Repeat Step 3.
7. Use a Pt plating current of 166 μA per window for approximately 1 min to obtain a 0.2 to 0.3- μm -thick layer of Pt.
8. Overplate the Pt layer with a 0.5- μm layer of Au. A plating current of 16 μA per window for 2 min is required.
9. Demount sample, clean with hot xylene, and blow dry with nitrogen.
10. Cleave and scribe individual lasers from the sample.
11. Scrub bottom (n-side) of the laser to a 10 to 18 transistor header using a AuSi eutectic preform at 365°C .
12. A 1-mil Au wire is thermal compression ball bonded to the 25 by 450- μm Pt-Au window. The other end of the gold wire is thermal compression ball bonded to the header post.

C.8.

TEST LASERS

1. Check current-voltage characteristics on the Tektronix by 573 transistor curve tracer.
2. Check luminescence from diode.
3. Check spontaneous and lasing spectra.

APPENDIX D

ELECTROCHEMICAL DEPOSITION OF OHMIC CONTACTS FOR DIODE LASERS

The typical method used for making ohmic contacts on GaAs high-power devices was to resistively evaporate AuGe for the back (n) contact, and Cr and Au through a physical mask for the front (p) contact, followed by sintering (alloying) the contacts at an elevated temperature. These contacts were not reproducible and had a fairly high impedance. In addition, the metallization for the n-contact must be wet by the AuSi used to attach the device to the package, and the front p-contact must be suitable for thermocompression wire bonding.

The resistively evaporated contacts proved to be of limited usefulness for small geometries evaporated through the physical mask (for the p-contact) because of difficulties encountered in the alignment of the mask to the wafer and also the edge definition. Photolithography and chemical etching of the front p-contact was attempted but was found to be impractical because of the surface attachment of the GaAs by the etches.

At the suggestion of A. B. Chase, electroplated metallization of a Pt and Au ohmic contact was tried.

The electroplating procedure developed involves the application of a given contact geometry in photoresist (Shipley AZ1350) for the p-side contact. This photoresist mask has a two-fold purpose: (1) to provide a mask for the confinement of the surface area to be plated and (2) to provide sidewall confinement of the plated material. At this point, the wafer is attached to the Al strip with conductive paint (Dotite), and all surfaces except those to be plated are insulated with Apiezon wax and xylene solution.

A very critical consideration of successful electrochemical deposition is that the surface be free of any foreign or native oxides, which appears to be satisfied by a predeposition immersion of the wafer in a 1:2

solution of HCL:DiH₂O for 3 min at ambient temperature. The wafer is then transferred directly to the Pt plating solution (the Pt plating solution is a commercial Halite solution) without rinsing to avoid any possibility of oxidation.

A current density of 200 $\mu\text{A}/\text{mil}^2$ has been established as being an optimum current density for Pt plating in this procedure. Voltage should be applied prior to insertion of the wafer into the flowing plating solution, to avoid an alteration of the GaAs surface. A pH of 3.5 was chosen for the Pt plating solution to prevent both surface damage and undercutting of the masking material. Although Pt plating is typically performed at ambient temperatures, an elevated temperature plating solution produces superior-quality depositions, as well as an accelerated deposition rate. Routinely successful plating was accomplished at a constant temperature of $\approx 60^\circ\text{C}$ for approximately 2 min. The thickness of the deposited film was between 0.2 and 0.3 μm . Films thicker than this lifted and pulled GaAs from the bulk crystal because of differences in the thermoexpansions of the materials.

At this time, the wafer is ready for the Au overplating (plating solution being a standard cyanide solution), which is conducted the same as the Pt deposition except for the current density of 2 $\mu\text{A}/\text{mil}^2$, ambient temperature plating solution, a film thickness of 0.6 to 0.7 μm , and an exclusion of the HCl surface preparation.

The n-side plating is changed only by a reduction in the Au thickness to 0.2 to 0.3 μm . The mounting, surface preparation, current density, and temperatures are the same as the p-side.

The results we have obtained both physically and electrically from this plating procedure have been excellent. Physical adhesion to both p- and n-sides has been far superior to any other contact previously used, thus greatly increasing contact integrity between p-contact and the thermocompression bonded wire contact, as well as the n-contact and the package.

The results obtained electrically indicate that the contacts are able to withstand repeated current pulses greater than 100,000 amp/cm^2 without

noticeable degradation. The contacts are also of very low resistance, on the order of approximately $6 \times 10^{-8} \Omega/\text{cm}^2$.

The areas of further study should include the establishment of current-time values and thickness parameters to obtain a given thickness of film on a given geometry and also to increase our knowledge of the ohmic contact itself.

APPENDIX E

COUPLED LASER THEORY

The interaction of two lasers was investigated for optical coupling and phase locking. Previously, Adler¹ examined phase locking for two oscillators in tandem and Basov et al.,² examined phase locking for two oscillators in parallel or side by side. In the analysis described here, the two cases are combined into a more general theory and the work of Basov et al. is extended. For the case when the lasers are placed in parallel, experimental results are given and compared to the theory.

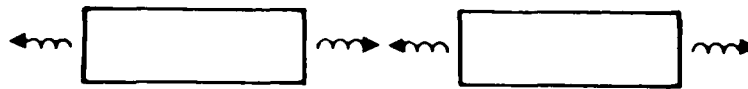
E.1. DESCRIPTION OF PHASE LOCKING

Lasers have a characteristic or natural frequency when they are free, not coupled to any other lasers. When two lasers are coupled, their output changes. Some possible ways of coupling are by end coupling (when two lasers are placed in tandem), diffraction or directional coupling in lasers placed side-by-side, and backscattering in ring lasers (Fig. E-1). The case for lasers placed side by side in parallel is treated here.

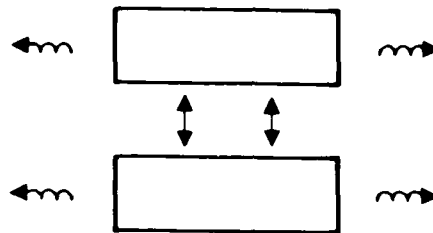
Very weak coupling between lasers introduces no change in the fields from that of free lasers. In this case, the lasers can be considered free. For stronger coupling, changes are seen in the output spectrum (Fig. E-2). A new frequency appears along with the characteristic frequency. This new frequency is the same as that of the coupled laser. We shall call this regime of weak coupling "optical coupling." The fields of the lasers are incoherent with respect to each other because the relative phase shift varies with time. Thus, the fields will not produce interference fringes in a diffraction pattern.

¹R. Adler, Proc. IEEE 61, 1380 (1973).

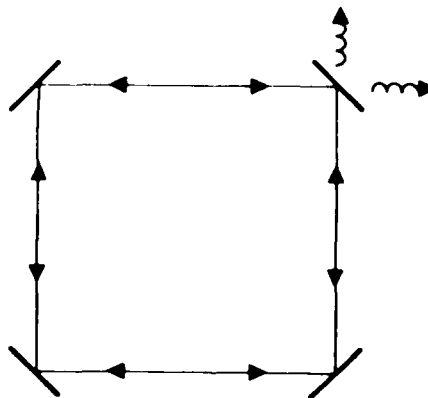
²N. G. Basov, E. M. Belenov, and V. S. Letokhov, "Diffraction Synchronization of Lasers," Sov. Phys. - Tech. Phys. 10, 845 (1965).



(a)



(b)



(c)

Fig. E-1. Geometries for Coupled Laser. (a) Tandem, end coupling. (b) Parallel, diffractive or directional coupling. (c) Ring, scattering.

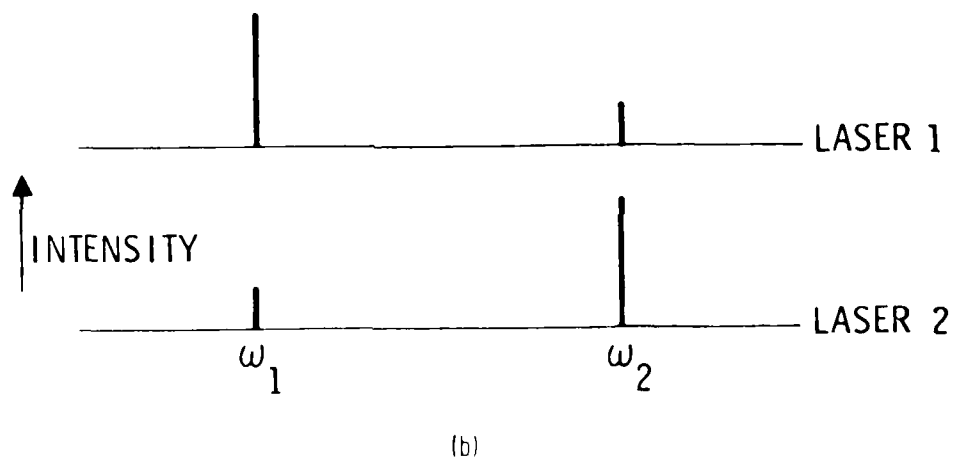
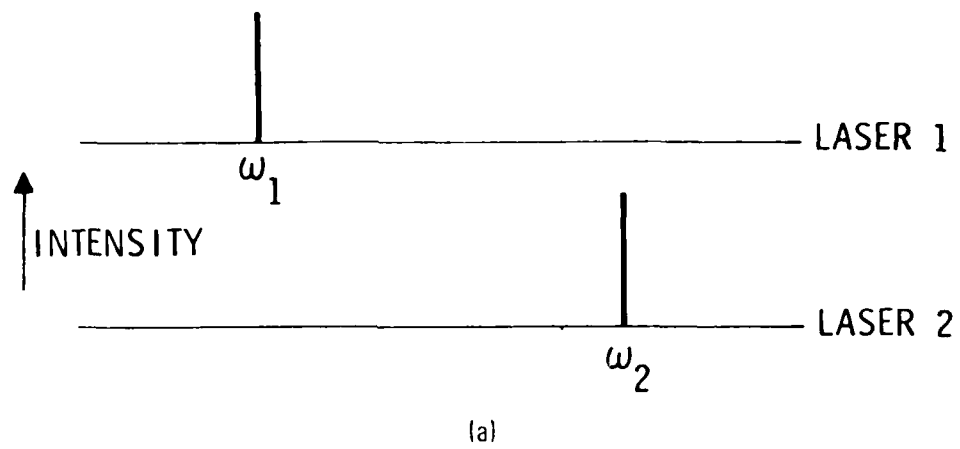


Fig. E-2. Laser Spectra. (a) Free uncoupled.
(b) Weakly coupled.

The intermediate coupling region covers the range of coupling strengths between the weak coupling regime and the threshold for locking. Sideband frequencies appear, with the intensity and spacing determined by the coupled fields and the initial frequency shift. In general, two free lasers will not oscillate exactly at the same frequency so there is an initial frequency difference. If this frequency shift is small and the coupled field is large, many sideband frequencies appear with a small spacing in frequency (Fig. E-3). Ultimately, for large coupling, the frequency spacing is zero, and the lasers are locked. The opposite is true for large frequency shifts and small coupled fields. The overall effect is a pulling of the characteristic frequency toward a frequency that is between the characteristic frequencies of the lasers and is called the locking frequency. The locking frequency is determined by the relative strengths of the laser fields. As the coupling strength approaches the threshold for locking, the coherence length of the lasers becomes greater. Interference patterns appear in diffraction patterns and become more distinct as the locking threshold is approached.

The strong coupling region covers locked lasers. As in the case for intermediate coupling, the degree of locking is also determined by the initial frequency difference. Locked lasers oscillate at a common frequency, the locking frequency (Fig. E-4). Because they have a common frequency, the relative phase shift between the lasers is constant in time. The lasers are thus coherent with each other and exhibit interference fringes in their diffraction pattern. Note that, although the relative phase shift between the lasers is constant, it is not zero.

These coupling regions are not rigidly defined, and the transitions between the regions are gradual. However, from this discussion, the determination of whether or not lasers are locked can be made by looking at the spectrum of the lasers, or at their diffraction pattern.

E-2. THEORY OF OPTICAL COUPLING

Optical coupling is the weak coupling limit of the more general problem of phase locking. Optical coupling occurs when the field from Laser 1 is coupled, by some means, to Laser 2. The output frequencies of Laser 2 is

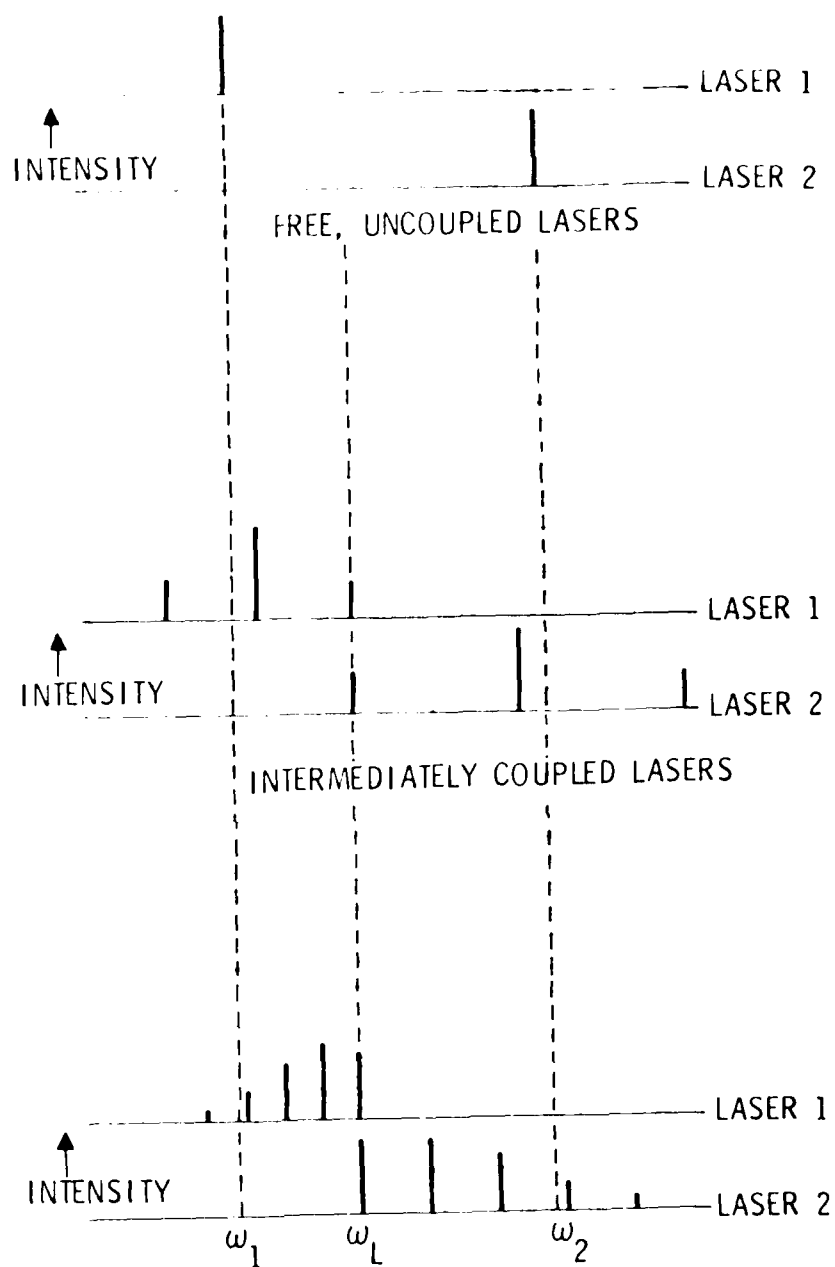


Fig. E-3. Intermediately Coupled Lasers with Stronger Coupling

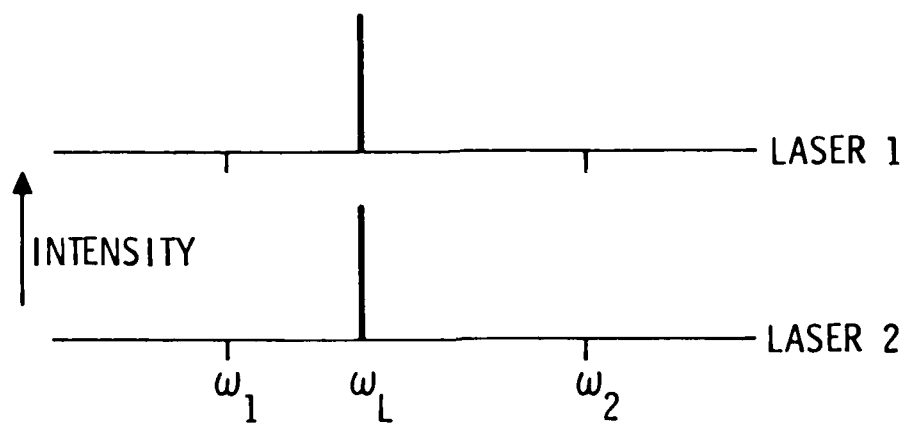


Fig. E-4. Locked Laser Spectra

that of the coupled field of Laser 1 and the characteristic frequencies of a free and uncoupled Laser 2. In general, optical coupling is a mutual effect so that the outputs of both lasers are different from the outputs of a free, uncoupled laser. However, the field of one laser may be much greater than the field of the other laser, in which case only one-way coupling need be considered.

Optical coupling can be described by the regenerative amplifier model. A laser below the lasing threshold is a regenerative amplifier. In this case, although a laser may be lasing at its characteristic frequency, it does not lase, but only amplifies the coupled field frequency.

In developing the regenerative amplifier model, the equations for an amplifier are derived. It can be shown that a simple amplifier model is not sufficient to describe the experimental data. However, when feedback is included in the model to form a regenerative amplifier, the model compares favorably with the data.

The two-laser geometry is shown in Fig. E-5. For clarity, one-way coupling only is shown. It is assumed that the coupled frequency is within the gain envelope of the laser.

If the net gain of Laser 2 at frequency ω_1 is small and the feedback minimal, it is an amplifier at that frequency. The differential equation for an amplifier with distributed coupling and gain is

$$\frac{dE_2}{dx} = g E_2 + K E_1 \quad (E-1)$$

where

E_2 = field of the amplifier (Laser 2)

E_1 = coupled field of the laser (Laser 1)

g = gain-loss coefficient

K = field coupling coefficient between the laser and the amplifier

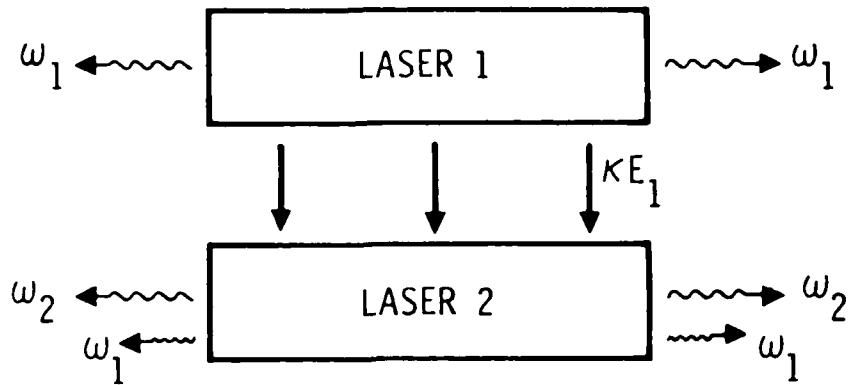


Fig. E-5. Tandem-Coupling Laser

The change in the field of the amplifier is the result of the net gain of the amplifying material plus the coupled field from Laser 1.

If no light was injected initially (by end coupling), then

$$E_2(x = 0) = 0 \quad (E-2)$$

The field in the amplifier as a function of propagation distance is then

$$E_2(x) = k [(\exp (gL) - ig)] E_1 \quad (E-3)$$

$$= \gamma E_1 \quad (E-4)$$

where L = amplifier length.

During one pass through an amplifier with no end coupling, the coupled field is amplified by a factor of γ . For an initially injected field of E_{in} ,

$$E_2(x) = E_{in} \exp (gL + i\theta) + \gamma E_1 \quad (E-5)$$

where θ is the phase shift incurred while propagating through the amplifier.

An amplifier with feedback is a regenerative amplifier. From Eq. (E-5) and Fig. E-6

$$E_{out} = E_{in} \exp (gL + i\theta) + \gamma E_1 \quad (E-6)$$

The feedback equation is

$$E_{in} = [r E_{out} \exp (gL + i\theta) + \gamma E_1] r \quad (E-7)$$

The output of the amplifier, E_2 , is

$$E_2 = 1 - r^2 E_{out} \quad (E-8)$$

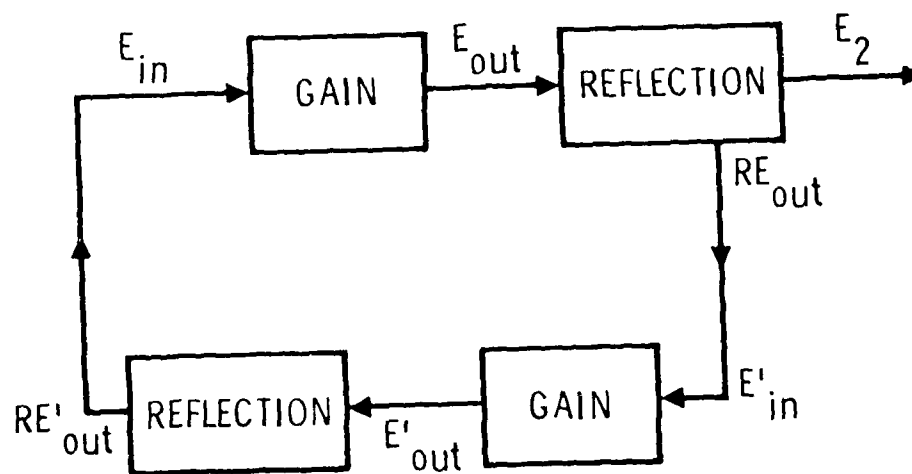


Fig. E-6. Regenerative Amplifier Circuit

where r is the field reflection coefficient. By solving Eqs. (E-6), (E-7), and (E-8), the equation for the intensity ratio is obtained.

$$\frac{I_2(w)}{I_1(w)} = \frac{E_2^2}{E_1^2} = |K L|^2 \frac{(1 - r^2) e^{2gL}}{1 + r^4 e^{4gL} - 2r^2 e^{2gL} \cos 2\theta} \left(\frac{e^{gL} - 1}{gL} \right)^2 \quad (E-9)$$

where

I_1 = intensity of the laser

I_2 = intensity of the amplifier

L = length of the amplifier

R = field reflection coefficient

g = gain-loss per unit length

K = coupling coefficient per unit length

θ = phase shift resulting from propagation through the amplifier

The intensity ratio is proportional to the coupling coefficient squared. The frequency dependence of the intensity ratio is contained in the gain g . The gain distribution is given in the following section. Equation (E-9) is valid for gains less than the threshold for lasing. As the threshold is approached, the gain starts to saturate and at threshold the intensity ratio is actually finite instead of blowing up as predicted by Eq. (E-9). For the data presented in the following section, all gains are below threshold.

The threshold gain can be found from the condition for lasing

$$1 = r e^{gL} \quad (E-10)$$

Hence, the threshold gain is

$$g_t = \frac{1}{L} \ln \frac{1}{r} \quad (E-11)$$

This gain is the net gain, the gain produced by pumping minus any losses resulting from scattering or absorption. A typical threshold gain is $g_t = 14 \text{ cm}^{-1}$.

E.2.1 Gain

The gain for a given pumping level j can be approximated by a Boltzmann-Lorentzian distribution

$$g_j(\nu) = g_o \exp(-\beta h \nu) \left[\left(1 + \frac{\nu - \nu_o}{\delta \nu_j} \right)^2 \right]^{-1} \quad (\text{E-12})$$

where

ν_o = frequency of the peak gain

$\delta \nu$ = half-width of the gain profile at half maximum

$\beta = 1/kT = 1/38 \text{ eV}$ at room temperature

The gain coefficient g_o can be determined by finding a longitudinal mode at threshold and comparing it with the mode exhibiting the peak gain. Rewriting $g_j(\nu)$ in terms of wavelength,

$$g_j(\lambda) = g_t \exp \left\{ 12400\beta \frac{\Delta \lambda}{\lambda_o^2} \frac{\left[1 + (\Delta \lambda_t / \delta \lambda_j) \right]^2}{\left[1 + (\Delta \lambda / \delta \lambda_j)^2 \right]} \right\} \quad (\text{E-13})$$

where

λ_t = threshold wavelength

λ_o = wavelength of peak gain

$\Delta \lambda = \lambda - \lambda_o$

$\Delta \lambda_t = \lambda_t - \lambda_o$

$\delta\lambda$ = half-width of gain profile

g_t = threshold gain

Experimental data are given in Section E.3 and compared with this theory.

E.3

OPTICAL COUPLING DATA

Two double-heterostructure GaAlAs lasers were placed side by side as shown in Fig. E-5. The lasers were defined by SiO₂ stripes laid on the wafer. A cross section of the laser geometry is shown in Fig. E-7. The top GaAs layer provided an ohmic contact between the p-type GaAlAs and the metal contact. Because the metal contact was common to all lasers, all of the lasers were simultaneously pumped in parallel.

The injected current pulse amplitude was slowly increased until one of the diodes started lasing (Diode 1). Measurements of the light outputs from the lasing diode and the nonlasing diode (Diode 2) were made at various currents between the thresholds of Diode 1 and Diode 2. Spectra of each of the diodes were monitored with a resolution of 0.3 Å. In addition, the image of the diodes could be translated across the monochromator slit to obtain spatial near or far-field profiles at a given frequency.

Typical spectra are shown in Fig. E-8. The periodicity was 40 μm, with a stripe width of 15 μm. The longitudinal mode envelope of Diode 1 ranged from 0.8700 μm to beyond 0.8725 μm peaking at $\lambda = 0.8723 \mu\text{m}$. Diode 2 had two sets of mode envelopes oscillating. The shorter wavelength modes peaked at 0.8707 μm and died out at 0.8711 μm. These modes were the natural modes of Diode 2. The other set of modes at the longer wavelength ($\lambda \sim 0.8720 \mu\text{m}$) was beyond the natural mode envelope of Diode 2. These modes were the result of amplified optical coupling from Diode 1. Matching the spectrum of Diode 1 with the spectrum of Diode 2 indicates that the coupled modes of Diode 2 are at the same frequency as that of Diode 1. Note that the optical coupling efficiency without amplification is about 1%. This would make coupled light unobservable. But with amplification by a gain medium, optical coupling can be observed.

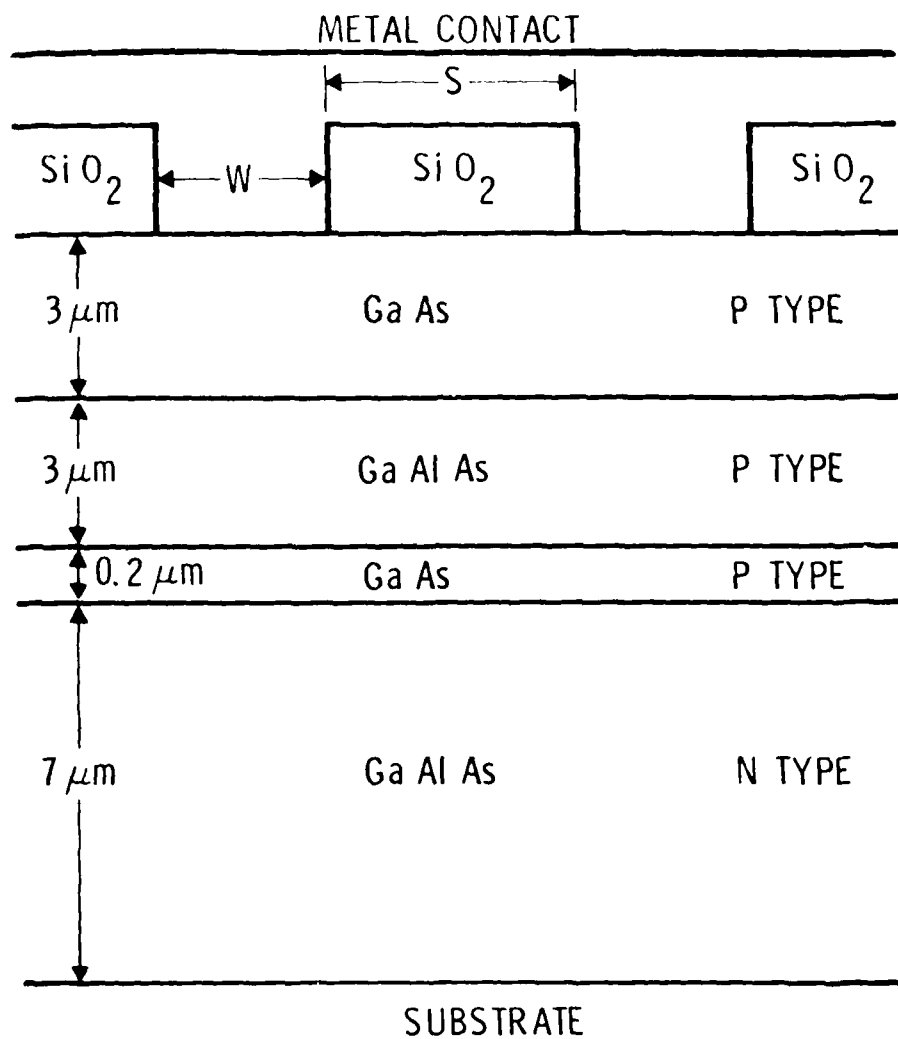


Fig. E-7. Coupled Laser Stripes Cross-Sectional Geometry

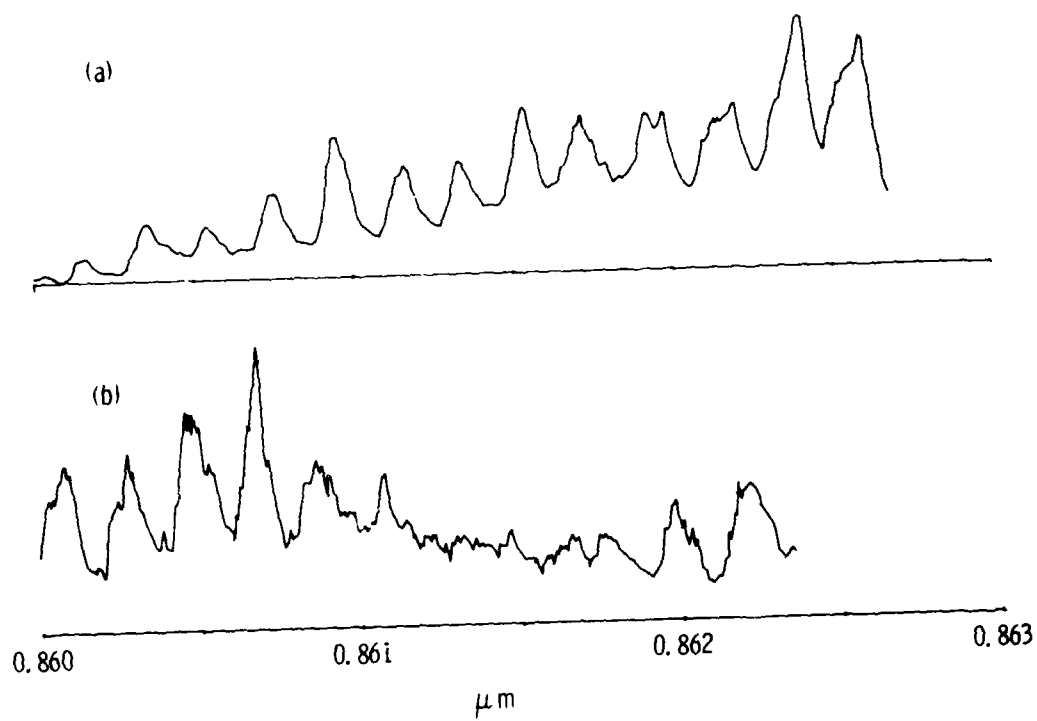


Fig. E-8. Unlocked Coupled Laser Spectra

These experimental results for optical coupling are compared with the theory in Section E.2. The gain of the amplifier is given by Eq. (E-13). With $n = 3.6$, $R = (n - 1/n + 1)^2$, $l = 400 \text{ } \mu\text{m}$, $\beta = 1/38 \text{ eV}$, $\lambda_t = 8611 \text{ } \text{\AA}$, $\lambda_o = 8607 \text{ } \text{\AA}$, $\Delta\lambda_t = 4 \text{ } \text{\AA}$, and $\delta\lambda = 6 \text{ } \text{\AA}$, Eq. (E-13) becomes

$$g_j(\lambda) = g_t \frac{1.44}{1 + (\Delta\lambda)^2/36} \quad (\text{E-14})$$

At the coupled wavelength $\lambda = 8618 \text{ } \text{\AA}$, the gain threshold for lasing [from Eq. (E-11)] is $g_t = 14.3 \text{ cm}^{-1}$. In this case, Eq. (E-14) is

$$g_j(\lambda) = 4.7 \text{ cm}^{-1} \quad (\text{E-15})$$

Working backwards from the measured intensity ratio, $I_2/I_1 = 0.2$, to predict the coupling coefficient for a gain of 4.7 cm^{-1} , and Eq. (E-9) predicts

$$|KL|^2 = 0.025 \quad (\text{E-16})$$

Two and a half percent of the intensity of Diode 1 was coupled to the amplifier.

A theoretical expression for the coupling coefficient of the fields in the strong coupling limit is

$$|K| = \frac{(\Delta\epsilon w)^2 k_o^3}{Ln} \exp\left[-(\Delta\epsilon w) k_o^2 s\right]^{1/2} \quad (\text{E-17})$$

where

$\Delta\epsilon$ = dielectric constant step between the diodes and the intervening areas

w = width of the laser stripes

s = separation between the near edges of the diode stripes
Fig. E-7

$k_o = 2/\lambda_o$

n = refractive index in the diodes

K = coupling coefficient between fields in the two diodes

Maximizing K with respect to $(\Delta\epsilon w)$, the maximum value of K is

$$(K)_{\max} = \frac{2}{e} \frac{\lambda}{2\pi n s^2 L} \quad (E-18)$$

at

$$(\Delta\epsilon w) = \frac{2}{k_o^2 s} \quad (E-19)$$

For a typical diode laser, $\lambda = 0.862 \mu\text{m}$, $s = 25 \mu\text{m}$, $n = 3.6$, $L = 400 \mu\text{m}$, and $(KL) = 0.33 \text{ cm}^{-1}$. These values permit the calculation of the fraction of laser light that is coupled per pass:

$$(KL)^2 = 1.3\%$$

which compares with the value determined from the measurements of 2.5%.

Optical coupling has been observed, and the measured coupling coefficient compares favorably with the theoretical value when the regenerative amplifier model is used. In this model, it is assumed that the coupled field is within the gain envelope of the diode to which it is coupled,

and that secondary effects such as coupling of the coupled field back into the original diode are negligible.

E.4 THEORY OF INJECTION LOCKING

The theory of injection locking has been discussed in E.2 for the case when one oscillator is weakly coupled to the other. The behavior of coupled oscillators near and above the threshold for phase-locking are described here. While the model of the regenerative amplifier works well for weakly coupled oscillators, it does not explain the phenomena of strongly coupled oscillators. The regenerative amplifier model does not permit the pulling of frequencies, the locking of lasers at a common frequency, or any of the other locking characteristics such as locking times.

Three models have been proposed to describe phase locking. The first was the phasor model of Adler.¹ Adler's model dealt with the relative phase difference between two oscillators. His model assumes a master-slave arrangement, that coupling occurs in only one direction. This model is good when there is an optical isolator between lasers or when one laser is much more intense than the other. However, when the laser fields are of comparable magnitude, Adler's model breaks down, since the model does not allow for mutual coupling.

The second model is that of Statz and Tang.³ Their model, again a master-slave, is based on oscillator equations at two frequencies; the free, uncoupled frequency of the slave and the coupled frequency of the master. This model breaks down when the master-slave relationship does not hold, and does not demonstrate frequency pulling and the dynamic effects of locking.

The third model was developed by Basov, Belenov, and Letokhov² and is the one used here. This model is based on an oscillator equation for each oscillator, with additional terms and equations to describe the coupling.

³H. Statz and C. L. Tang, "Phase-Locking of Laser Oscillators by Injected Signal," J. Appl. Phys. 38, 323 (1967).

In Basov's model, diffraction coupling is assumed, instead of the end coupling of Adler and Statz and Tang.³ The described theory here includes both forms of coupling. Whereas Basov only gave the conditions for locking, other locking phenomena such as frequency pulling, locking frequency, and locking times are derived.

E.4.1 Locking Conditions

The oscillator equations for the lasers are

$$\epsilon_1 + \frac{\omega_1}{Q} \dot{\epsilon}_1 - \omega_o \alpha \dot{\epsilon}_2 + \omega_1^2 \epsilon_1 = 0 \quad (\text{E-20})$$

$$\ddot{\epsilon}_2 + \frac{\omega_2}{Q} \dot{\epsilon}_2 - \omega_o \alpha \dot{\epsilon}_1 + \omega_2^2 \epsilon_2 = 0 \quad (\text{E-21})$$

where

- ϵ_j = field of oscillator j
- Q = cold cavity Q of the oscillators
- ω_j = natural frequency of j
- ω_o = locking frequency of the oscillators
- α = coupling efficiency

It is assumed that the cavity Q s for both oscillators are equal. The second term represents the losses in the oscillator, and the third term represents the coupled radiation. This may be provided by end coupling or side coupling (directional coupling and diffractive coupling). If these oscillators were uncoupled, they would oscillate at their natural frequency ω_1 and ω_2 , respectively (the fourth term).

Since, in general, the fields have different phase shifts, ϵ_j can be rewritten,

$$\epsilon_j = E_j \exp i\omega_o(t + \phi_j) \quad (E-22)$$

where E_j is slowly varying over an optical cycle time period, $1/2\pi\omega_o$. The change in the phase shift ϕ_j is also small over a time period. Cold cavity Qs of lasers, such as GaAs, are of the order of 10^4 so that $1/Q \ll 1$. The coupling efficiency α is of the order of a few percent. By substituting Eqs.(E-22) and (E-23) into Eqs. (E-20) and (E-21), and regrouping terms according to their order of magnitude, an equation for the change in the electric field phase shift is obtained.

$$\phi_j = - \frac{\omega_j^2 - \omega_o^2}{2\omega_j^2} + \frac{\omega_i \omega_o}{\omega_j^2} \frac{\pi}{2} \frac{E_i}{E_j} \sin (\phi_i - \phi_j) \omega_o \quad (E-23)$$

where $j \neq i$.

For the frequencies of interest,

$$\omega_1 \approx \omega_2 \approx \omega_o \quad (E-24)$$

Then

$$\phi_j = - \frac{\omega_j - \omega_o}{\omega_o} + \frac{\alpha}{2} \frac{E_i}{E_j} \sin \omega_o (\phi_i - \phi_j) \quad (E-25)$$

The conditions for locking are obtained by examining Eq. (E-25) in the steady state when $\phi_j = 0$

$$\frac{\omega_j - \omega_o}{\omega_o} < \frac{\alpha}{2} \frac{E_i}{E_j} \quad (\text{E-26})$$

Equation (E-26) provides the frequency range over which locking can occur for a given coupling efficiency and oscillator fields.

The coupling can be provided by side coupling or end coupling. For side coupling, the coupling process can be directional or diffractive coupling. Basov² assumed diffractive coupling to derive his results, which agree with Eq. (E-26). For directional coupling $K = \lambda_o/2\pi n$. For end coupling, the coupling is dependent upon the reflectivity of the end mirrors or the cavity Q. Thus, Eq. (E-26), in terms of the cavity Q, is

$$\frac{\omega_j - \omega_o}{\omega_o} < \frac{1}{2Q} \frac{E_i}{E_j} \quad (\text{E-27})$$

where

$$Q = \frac{2}{\lambda_o} \frac{n}{\alpha_o - 1/L \ln R}$$

n = refractive index

L = oscillator length

R = mirror reflectivity

α_o = distributive loss coefficient

Equation (E-27) is identical to the results of Adler¹ and Statz and Tang.³

Phase locking has been observed in a pair of lasers with a 25- μm separation distance and verified by two different methods: (1) comparing the longitudinal mode spectrum of each laser and (2) observing interference fringes in the far-field diffraction pattern. The spectra of two locked lasers are shown in Fig. E-9. As can be seen, the longitudinal modes of both lasers peak at a common wavelength.

Two lasers, when phase locked, are coherent with respect to each other and, hence, exhibit interference fringes in the far-field diffraction pattern. The far-field diffraction pattern for phase-locked lasers is shown in Fig. E-10. Interference between the two lasers is clearly evident. From the interference pattern, it was inferred that the lasers were 10 μm apart, using the double slit model for plane waves, which is in reasonable agreement with the stripe separation of 13 μm .

The individual free laser characteristics were not measured because the lasers were not individually pulsed. However, the range of wavelengths over which phase locking occurs can be calculated. The coupling coefficient can be determined from the equation for the directional coupling coefficient per unit length. For $\lambda = 0.86 \mu\text{m}$, $L = 400 \mu\text{m}$, and $n = 3.6$;

$$\alpha \approx \frac{K}{k_0} = 2.82 \times 10^{-5}$$

From Eq. (E-26), the locking range for $E_1/E_2 = 1$ is

$$\Delta\lambda = 0.12 \text{ \AA}$$

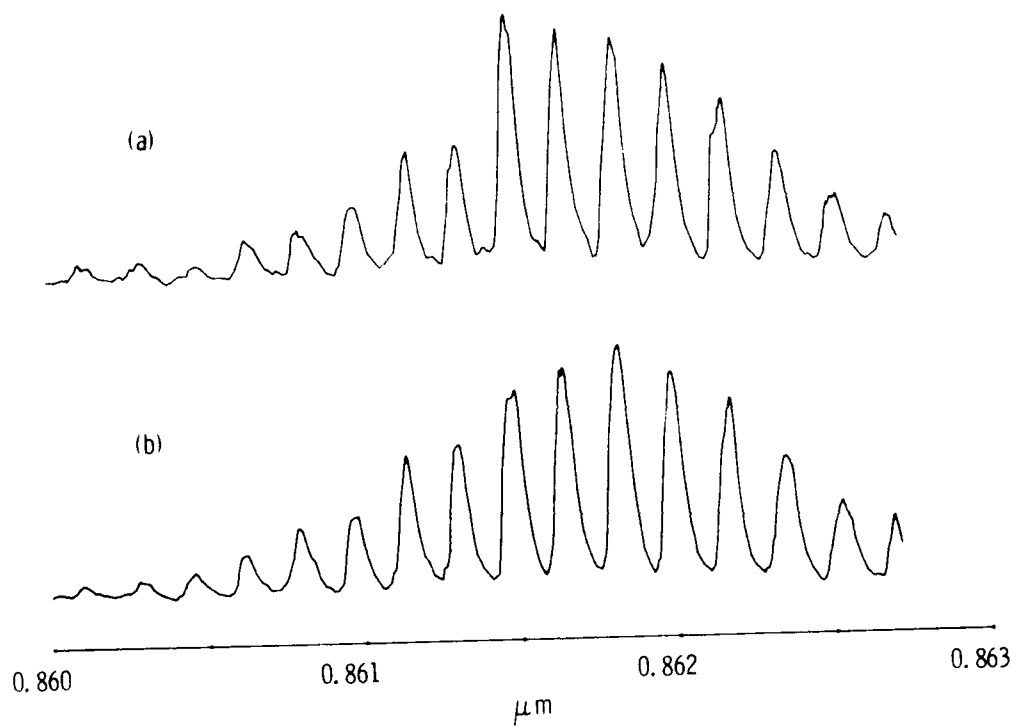
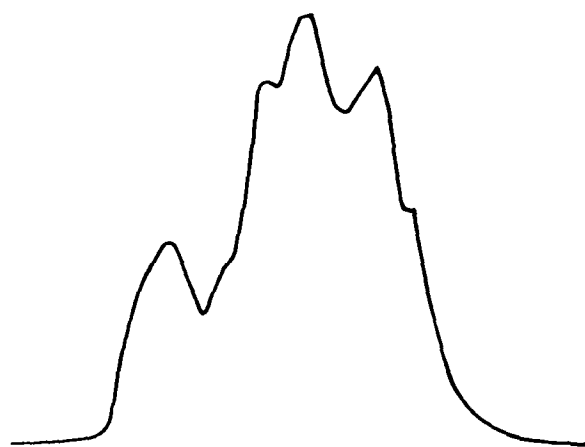
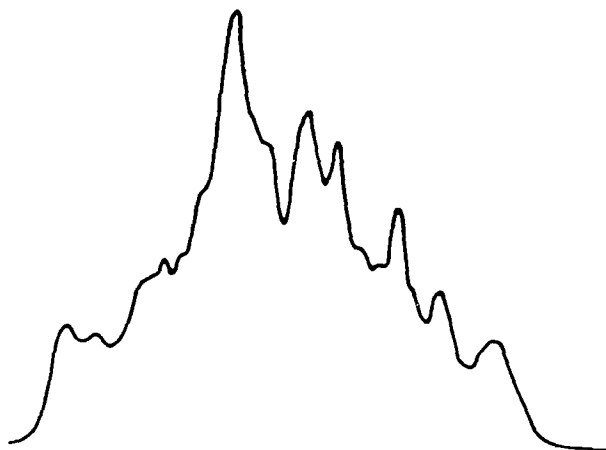


Fig. E-9. Locked Laser Spectra



(a)



(b)

Fig. E-10. Locked Lasers. (a) Near-field profile. (b) Far-field profile.

Thus, for a pair of mutually coupled lasers, twice this range, i.e., 0.24 Å, is the maximum wavelength difference between the free and uncoupled wavelengths for which phase locking can occur.

Experiments are currently under way in which individually pulsed lasers are being used. This should provide more information about the individual lasers both above and below the threshold for locking since the power of each laser can be independently controlled.

APPENDIX F

DBR: A MULTIFUNCTION INTEGRATED OPTICAL DEVICE

F.1 INTRODUCTION

The properties of wide-angle, integrated optical Bragg deflectors in which slab-coupled optical waveguides are used are analyzed. Specifically considered is the interaction which occurs, through the intermediary of a periodic waveguide perturbation, between an incident waveguide within the core region of the structure and a Bragg-deflected beam guided within the slab region of the structure. The deflection efficiencies and far-field deflected-beam intensity patterns characteristic of this distributed Bragg deflector (DBD), are derived for both transverse electric (TE) and transverse magnetic (TM)-polarized incident waves and for deflection angles between $\pi/4$ and $3\pi/4$ rad.

A large number of passive and active integrated optical devices may be developed by exploiting the phenomenon of wide-angle intrawaveguide Bragg scattering off fixed or tunable periodic waveguide perturbations. The principal advantages of such devices, compared to their shallow-scattering-angle counterparts,^{1,2,3,4} include compactness, good incident- and deflected-beam separation and accessibility, and considerable device versatility and design flexibility. Several wide-angle intrawaveguide deflection devices have been demonstrated, which have relied upon optical waveguides overmoded in either or both dimensions transverse to the direction of propagation. Multimode devices that have depended upon fixed periodic waveguide perturbations as the scattering intermediary have included thin-film modulators,^{5,6} deflectors,⁷ and beam splitters.⁷ Tunable periodic waveguide deflectors formed by magnetic stripe domains have been used as multi-mode waveguide modulators and suggested as promising wide-angle intrawaveguide beam scanners.⁸ It is the purpose here to describe the operational characteristics and potential applications of wide-angle intrawaveguide Bragg deflection devices that utilize single-mode

two-dimensional optical waveguides of the type one would expect to be used in future integrated optical circuits.

The single-mode waveguiding structure has been generically termed a slab-coupled waveguide by Marcatili.⁹ In the present context, the usefulness is that it may support both one and two dimensional guided waves, the former within the slab region of the structure, and the latter within its core. By locating a periodic waveguide perturbation of appropriate period and orientation within or adjacent to the core region, a two dimensionally confined wave initially propagating within the core region may be gradually converted by means of coherent Bragg scattering into a one dimensionally confined mode that propagates within the slab region. The resultant periodically perturbed slab-coupled waveguiding structure is a distributed Bragg deflector (DBD).

Passive integrated optical applications of the DBD structure include guided-wave beam deflection, division, and, for 90 deg Bragg scattering, polarization analysis. In addition, because of the gradual or distributed nature of the Bragg scattering process, a properly configured DBD may be used to effect lensless, intrawaveguide beam expansion. When combined with a suitably oriented output grating coupler, the latter application indicates that the utility of the DBD as a device for reducing the beam divergence of fully integrated lasing sources (provided with DBR or distributed feedback cavities and mated with a passive waveguiding region in which the beam expansion could be accomplished), or as a means by which two-dimensional slab-coupled waveguides could be accessed by large-diameter beams externally incident on the waveguiding structure. With regard to active integrated optical devices, the relative insensitivity of the Bragg scattering condition within the DBD, appears to limit its active applications to those that may be realized through the direct manipulation of its spatial (i.e., period or perturbation orientation) properties. As a consequence, wide-angle DBD beam scanners or switches based upon, for example, tunable magnetic stripe domains appear feasible,⁸ whereas wide-angle DBD devices dependent upon a modification or violation of the Bragg condition do not.⁷

Top, side cross-sectional, and end cross-sectional views of the prototypical DBD structure to be analyzed are shown in Fig. F-1. With reference to the core region, in which two-dimensional guiding takes place, mode confinement in the z -direction is assumed to occur as a result of step discontinuities in refractive index at the superstrate guide and guide substrate interfaces. Mode confinement within the core region in the y -direction is assumed to result from the dispersive effects associated with either a height variation in the vicinity of the core region or superstrate loading over the core region (Fig. F-2). Figure F-2(a) is a cross-sectional view through an imbedded ridge¹⁰ DBD structure (lateral confinement caused by height variation), and Fig. F-2(b) is a cross-sectional view through a strip-loaded¹¹ DBD structure (lateral confinement caused by superstrate loading). For analysis, the lateral confinement effect, induced either by a height variation or by superstrate loading, is accounted for by the geometry of Fig. F-1(c) in which the core region has been assigned an effective refractive index, n_2 and a height (in the z -direction) equal to that of the slab. n_2 is, of course, taken to be greater than n_s , the effective refractive index of a one-dimensionally guided mode propagating in the slab region of the structure.

Coupling between the core-propagating and slab-propagating modes is assumed to occur as a result of a suitably located and oriented periodic waveguide perturbation. Although this analysis is applicable to any type of perturbation geometry, only one specific case will be considered: the square-wave type surface corrugation shown in Figs. F-1(b) and F-1(c). The extent of this perturbation in the z -direction will be governed by the depth of the surface corrugations; its extent in the y -direction will, for convenience, be taken equal to the equivalent width¹² (in the y -direction) of the core-propagating mode. This approximation, illustrated by the mode profile shown in Fig. F-1(c), may be expected to change the results of the analysis only slightly.

The Bragg deflection process to be analyzed is schematically portrayed in Fig. F-1(d). The incident wave is shown by the solid arrows. A core-propagating wave

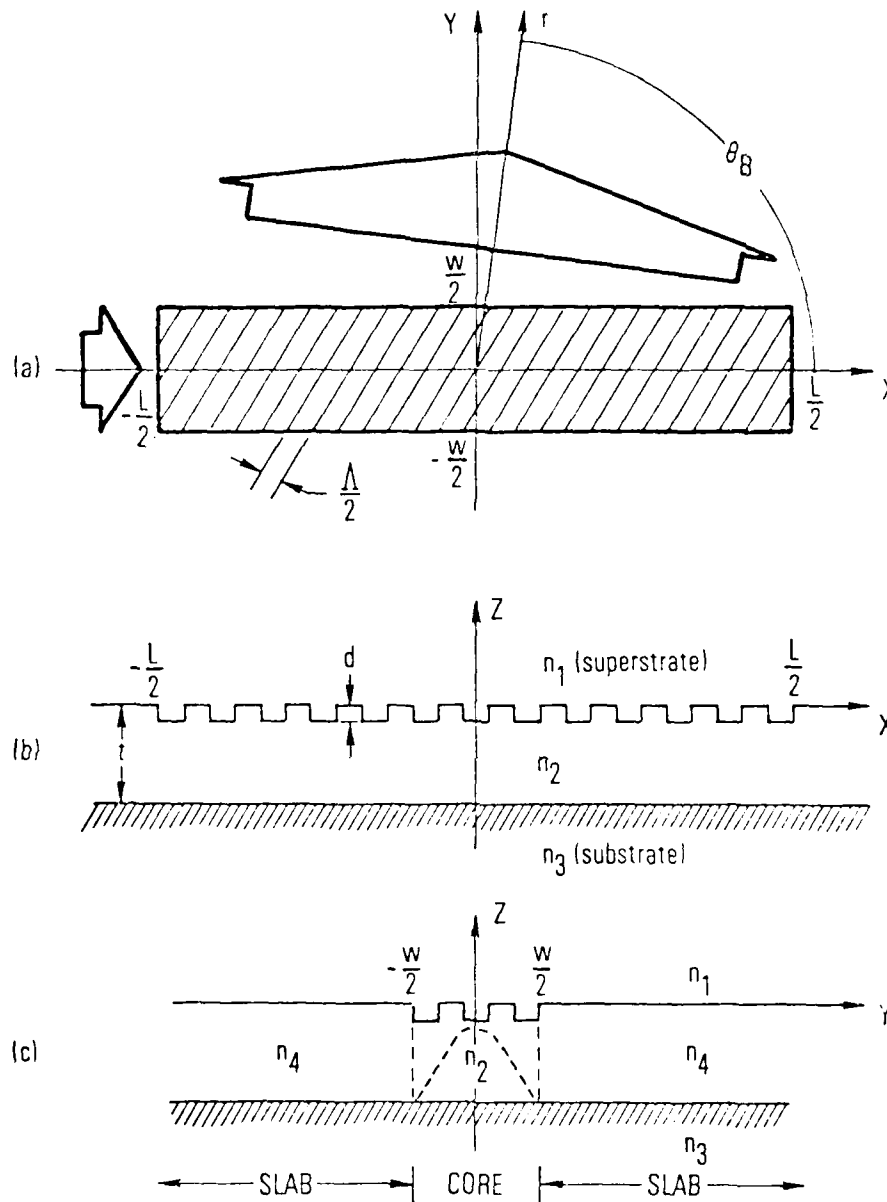


Fig. F-1. DBD. (a) Top view. (b) Side cross-sectional view. (c) End cross-sectional view. Small and large (solid) arrows in (a) represent incident and deflected beams, respectively. Dashed sinusoid in (c) represents "equivalent" core field distribution in y -direction.

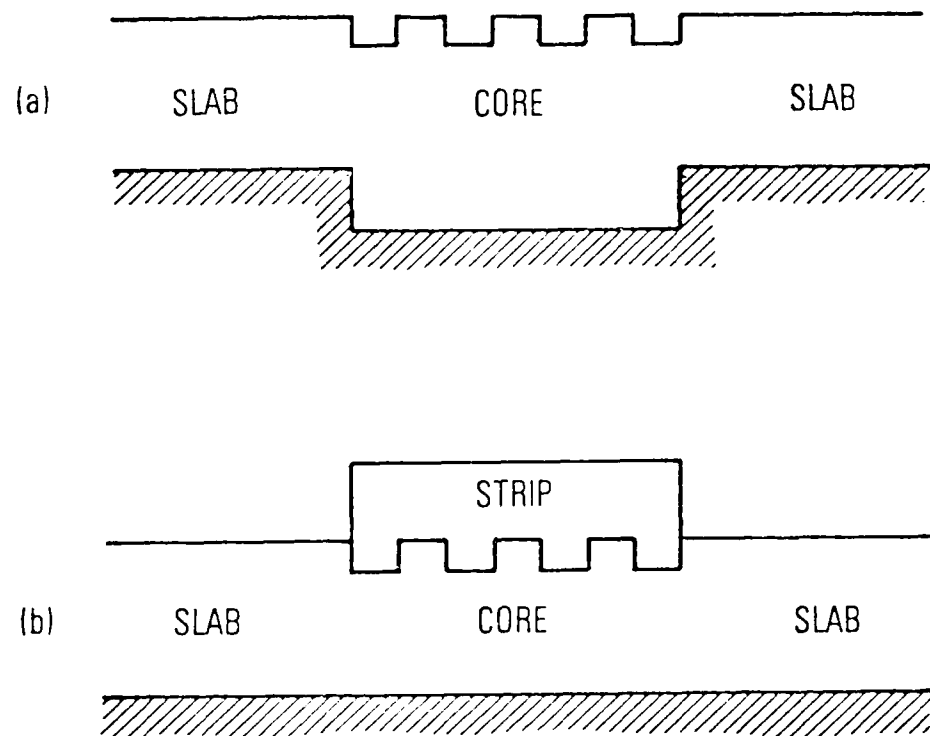


Fig. F-2. DBD. (a) End cross-sectional view of imbedded ridge. (b) End cross-sectional view of strip-loaded DBD.

incident on the distributed Bragg deflector from the negative x-direction is converted, by a periodic waveguide perturbation, into a slab-propagating wave that is deflected through an angle θ_B with respect to the x-axis. The problem addressed is that of finding the field distribution of the deflected wave. Coherent waveguide scattering or mode conversion problems such as this may be treated with either the coupled-mode formalism^{13,14} or a Green's function technique.¹⁵ Given the interaction geometry shown in Fig. F-1, wherein an insignificant amount of the deflected wave is expected to be fed back into the incident wave and for which the incident wave field distribution within the interaction region may be well approximated, the Green's function technique is preferred and will, as a consequence, be the one used. Accordingly, the analytical approach to be followed will be to: (1) define an appropriate Green's function, (2) assume a form for the core-propagating wave that accounts for the Bragg scattering process through the inclusion of an attenuation factor $\exp(-\alpha x)$, (3) calculate the deflected wave field distribution by convolving the incident wave field distribution with the Green's function, (4) determine the power carried away by the deflected wave, and (5) derive an expression for α by invoking conservation of power for the incident, transmitted (within the core, past the DBD), and deflected waves. Once α is known, the deflector efficiency and deflected wave far-field patterns can be found. The analysis will be carried out for the both TE (electric fields polarized parallel to the x-y plane) modes and TM (magnetic fields polarized parallel to the x-y plane). The angular deflection range to be considered will be that for which $\pi/4 \leq \theta_B \leq 3\pi/4$.

F.3 DEFLECTED WAVE-FIELD CALCULATIONS

The TE and TM vector Helmholtz equations describing wave propagation within the DBD structure are for TE

$$\left(\nabla^2 + n_1^2 k_o^2 \right) \vec{E} = \begin{cases} \vec{Q}_{TE} & -d \leq z \leq 0 \\ 0 & \text{otherwise} \end{cases} \quad (F-1)$$

and for TM

$$\left(\nabla^2 + n_1^2 k_o^2\right) \vec{H} = \begin{cases} \vec{Q}_{TM} & -d \leq z \leq 0 \\ 0 & \text{otherwise} \end{cases} \quad (F-2)$$

where

$$\vec{Q}_{TE} + -k_o^2 \Delta n^2(\vec{r}) \vec{E} - \nabla \left\{ \vec{E} \cdot \nabla \log \left[\epsilon_o n_2^2 + \epsilon_o \Delta n^2(\vec{r}) \right] \right\} \quad (F-3)$$

and

$$\vec{Q}_{TM} = -k_o^2 \nabla n^2(\vec{r}) \vec{H} - \nabla \log \left[\epsilon_o n_2^2 + \epsilon_o \Delta n^2(\vec{r}) \right] \times \nabla \times \vec{H} \quad (F-4)$$

In Eqs. (F-1) through (F-4), k_o is the magnitude of the free space wave-vector, ϵ_o is the permittivity of free space, n_i refers to the refractive index of medium "i" ($i = 1, 2, 3, 4$), " ∇ " is the del operator, and $\Delta n^2(\vec{r})$ the periodic waveguide perturbation. For the square-wave surface corrugation under consideration,

$$\Delta n^2(\vec{r}) = \left(n_1^2 - n_2^2 \right) \left\{ \frac{1}{2} - \frac{2}{\pi} \sum_{\ell=1}^{\infty} \frac{(-1)^{\ell-1}}{(2\ell-1)} \cos [(2\ell-1)\vec{K} \cdot \vec{r}] \right\} \quad (F-5)$$

where \vec{r} is the position vector ($|\vec{r}|^2 = x^2 + y^2 + z^2$), and \vec{K} is the fundamental mechanical phase vector of the perturbation ($|\vec{K}| = 2\pi/\Lambda$; Λ = perturbation period).

The electric and magnetic fields that satisfy Eqs. (F-1) and (F-2) are composed of core- and slab-propagating modes that, in accordance with the procedure outlined in Section F.2, can be written

$$\vec{E} = \vec{E}^C + \vec{E}^S = E^C(y, z) \exp \left[-i \left(k_{TE}^C x \right) \right] \hat{a}_y + \vec{E}^S \quad (F-6a)$$

and

$$\vec{H} = \vec{H}^C + \vec{H}^S = H^C(y, z) \exp \left[-i \left(\tilde{k}_{TM}^C \right) x \right] \hat{a}_y + \vec{H}^S \quad (F-6b)$$

where \hat{a}_y is a unit vector in the y-direction, \vec{E}^C (or \vec{H}^C) is the assumed field distribution of the core-propagating mode, \vec{E}^S (or \vec{H}^S) is the unknown field distribution of the Bragg deflected slab-propagating mode, and the core-propagating phase-vectors \tilde{k}_{TE}^C and \tilde{k}_{TM}^C have been taken to be complex in order to account for the attenuation that results from the Bragg scattering process. The core-propagating modes E^C and H^C (following Marcatili's analysis)¹⁶ are assumed to be well enough confined so that, to a good approximation, their field distributions can be separated in the y and z coordinates as follows:

$$E^C(y, z) = \sqrt{\frac{2\omega\mu_0}{k_{TE}^C}} W(y) \epsilon(z) \quad (F-7a)$$

$$H^C(y, z) = \sqrt{\frac{2\ell\epsilon_0}{k_{TM}^C}} W(y) \mathcal{H}(z) \quad (F-7b)$$

In Eqs. (F-7a) and (F-7b), E^C and H^C have been normalized to reflect the assumption that, prior to entering the DBD structure, each mode carried 1 W of power in the positive x-direction. Also, k_{TE}^C and k_{TM}^C $\left[= \text{Re}(\tilde{k}_{TE}^C) \text{ and } \text{Re}(\tilde{k}_{TM}^C), \text{ respectively} \right]$ have been taken to be the magnitudes of the phase vectors of core-propagating modes in the absence of any mode conversion.

$W(y)$, the transverse field variation in the y-direction for either TE- or TM-polarized core-propagating modes, is approximated as

$$W(y) = \sqrt{\frac{2}{w}} \cos\left(\frac{\pi y}{w}\right) \quad (F-8)$$

where w equals both the equivalent width¹² of the actual field distribution and the physical extent of the periodic DBD perturbation in the y-direction.

(Errors in later field calculations arising from this approximation are expected to be small for modes that are reasonably well confined in the y-direction.) $\epsilon(z)$ and $\mathcal{K}(z)$, the TE- and TM-mode field variations, respectively, in the z-direction, are found by applying the appropriate boundary conditions to the solutions of¹⁷

$$\left\{ \frac{d^2}{dz^2} + \left[n_i^2 k_o^2 - \left(\frac{\pi}{w} \right)^2 - \left(k_{TE}^c \right)^2 \right] \right\} \epsilon(z) = 0; \quad i = 1, 2, 3 \quad (F-9a)$$

and

$$\left\{ \frac{d^2}{dz^2} + \left[n_i^2 k_o^2 - \left(\frac{\pi}{w} \right)^2 - \left(k_{TM}^c \right)^2 \right] \right\} \mathcal{K}(z) = 0; \quad i = 1, 2, 3 \quad (F-9b)$$

which result from substituting Eqs. (F-7a), (F-7b), and (F-8) into the scalar Helmholtz equation. Because of the form chosen for $W(y)$ and the normalization imposed by (F-7a) and (F-7b), $\epsilon(z)$ and $\mathcal{K}(z)$ are themselves normalized as follows

$$\int_{-\infty}^{\infty} \epsilon^2(z) dz = \int_{-\infty}^{\infty} \frac{\mathcal{K}^2(z)}{n_i^2} dz = 1; \quad i = 1, 2, 3 \quad (F-10)$$

With Eqs. (F-5), (F-6a) and (F-6b) used, the TE and TM driving terms of Eqs. (F-1) and (F-2) are now calculated to be

$$\begin{aligned} \vec{Q}_{TE} &= \vec{Q}_{TE}(\vec{E}^c) + \vec{Q}_{TE}(\vec{E}^s) \\ &= (A_x \hat{a}_x + A_y \hat{a}_y) E^c(y, z) \exp \left\{ -i \left[\tilde{k}_{TE}^c x + (2\ell - 1) \vec{k} \cdot \vec{r} \right] \right\} + \vec{Q}_{TE}(\vec{E}^s) \end{aligned} \quad (F-11a)$$

and

$$\begin{aligned}\vec{Q}_{TM} &= \vec{Q}_{TM}(\vec{H}^c) + \vec{Q}_{TM}(\vec{H}^s) \\ &= (B_x \hat{a}_x + B_y \hat{a}_y) H^c(y, z) \exp \left\{ \left[-i \tilde{k}_{TM}^c x + (2\ell - 1) \vec{k}_r^+ \right] \right\} + \vec{Q}_{TM}(\vec{H}^s)\end{aligned}\quad (F-11b)$$

where

$$A_x = \frac{2(-1)^\ell}{\pi} \log \left(\frac{n_1}{n_2} \right) \left[(2\ell - 1) K_x K_y + k_{TE}^c K_y \right] \quad (F-12a)$$

$$A_y = \frac{(-1)^\ell}{\pi} \cdot \left[\frac{k_o^2 (n_1^2 - n_2^2)}{(2\ell - 1)} + 2(2\ell - 1) K_y^2 \log \left(\frac{n_1}{n_2} \right) \right] \quad (F-12b)$$

$$B_x = \frac{2(-1)^\ell}{\pi} K_y k_{TM}^c \log \left(\frac{n_1}{n_2} \right) \quad (F-12c)$$

and

$$B_y = - \frac{(-1)^\ell}{\pi} \left[\frac{k_o^2 (n_1^2 - n_2^2)}{(2\ell - 1)} + 2 k_{TM}^c K_x \log \left(\frac{n_1}{n_2} \right) \right] \quad (F-12d)$$

In deriving Eqs. (F-11a) through (F-12d), it has been assumed that $|\tilde{k}_{TE, TM}^c| \approx k_{TF, TM}^c$ and that, for those wavelengths, waveguide dimensions and deflection angles of interest

$$\frac{\partial}{\partial y} E^c(y, z) \frac{\partial}{\partial z} E^c(y, z) \ll K_{x, y} \quad (F-13)$$

The condition for Eq. (F-13) is most seriously violated in the case of long wavelengths, very small transverse waveguide dimensions (comparable to or smaller than a wavelength), and either very shallow or very large deflection angles.

Given analytical expressions for \vec{Q}_{TE} and \vec{Q}_{TM} , we now seek suitable TE- and TM-mode dyadic Green's functions that are solutions of the following inhomogeneous wave equations:

$$\left(\nabla^2 + n_i^2 k_o^2\right) \underline{G}_{TE}(\vec{r}|\vec{r}') = \underline{I} \delta(\vec{r}-\vec{r}'); \quad i = 1, 2, 3, 4 \quad (F-14a)$$

and

$$\left(\nabla^2 + n_i^2 k_o^2\right) \underline{G}_{TM}(\vec{r}|\vec{r}') = \underline{I} \delta(\vec{r}-\vec{r}'); \quad i = 1, 2, 3, 4 \quad (F-14b)$$

where \underline{I} is the idem factor and $\delta(\vec{r} - \vec{r}')$ is the three-dimensional delta function.

The dyadic Green's function, \underline{G} , is a solution of

$$\nabla^2 \underline{G} + n_i^2 k_o^2 \underline{G} = \underline{I} \delta(\vec{r} - \vec{r}'); \quad i = 1, 2, 3 \quad (F-15)$$

Given the simple boundary conditions that \underline{G} must satisfy (for either TE- or TM-polarized waves), \underline{G} can be written

$$\underline{G} = \sum_{m=1}^3 \hat{e}_m \hat{e}_m G \quad (F-16)$$

where \hat{e}_m is any set of curvilinear coordinate system unit vectors, and G is the scalar Green's function. Expressing Eq. (F-15) in terms of circular cylindrical coordinates and making the following coordinate transformation

$$\vec{R} = \vec{r} - \vec{r}'; \quad \theta_o = \theta - \theta'$$

the wave equation satisfied by G becomes

$$\frac{1}{R} \frac{\partial}{\partial R} \left(R \frac{\partial G}{\partial R} + \frac{\partial^2 G}{\partial z^2} \right) + n_i^2 k_o^2 G + \frac{\delta(R) \delta(\theta_o) \delta(z-z')}{R} \quad (F-17)$$

Since G is now recognized as being a function only of R and z , solutions of Eq. (F-17) within the source-free region may be found by writing $G(R,z) = f(R)h(z)$ and using separation of variables, which yields

$$\frac{1}{R} \frac{d}{dR} \left(R \frac{df}{dR} \right) + k^2 f = 0 \quad (F-18)$$

and

$$\frac{d^2 h}{dz^2} + (n_i^2 k_o^2 - k^2) h = 0 \quad (F-19)$$

where k^2 is the separation constant and the solutions of Eq. (F-19) are recognized as being either $\epsilon_{o,v}(z)$ (for the TE-polarized waves) or $o_v(z)$ (for the TM-polarized waves).

The admixture of h and f required to construct G can be found by integrating Eq. (F-17) over the cylindrical volume depicted in Fig. F-3. By ignoring contributions from the cylinder ends (valid for long, slender cylinders), this integration yields

$$2\pi\epsilon \int_{z=z'-}^{z=z'+} \frac{\partial G}{\partial R} \Big|_{R=\epsilon} dz = 1 \quad (F-20)$$

where use has been made of the divergence theorem, and ϵ is the radius of the cylinder. From Eq. (F-20), it is implied that

$$2\pi\epsilon \frac{\partial G}{\partial R} \Big|_{R=\epsilon} = \delta(z - z') \quad (F-21)$$

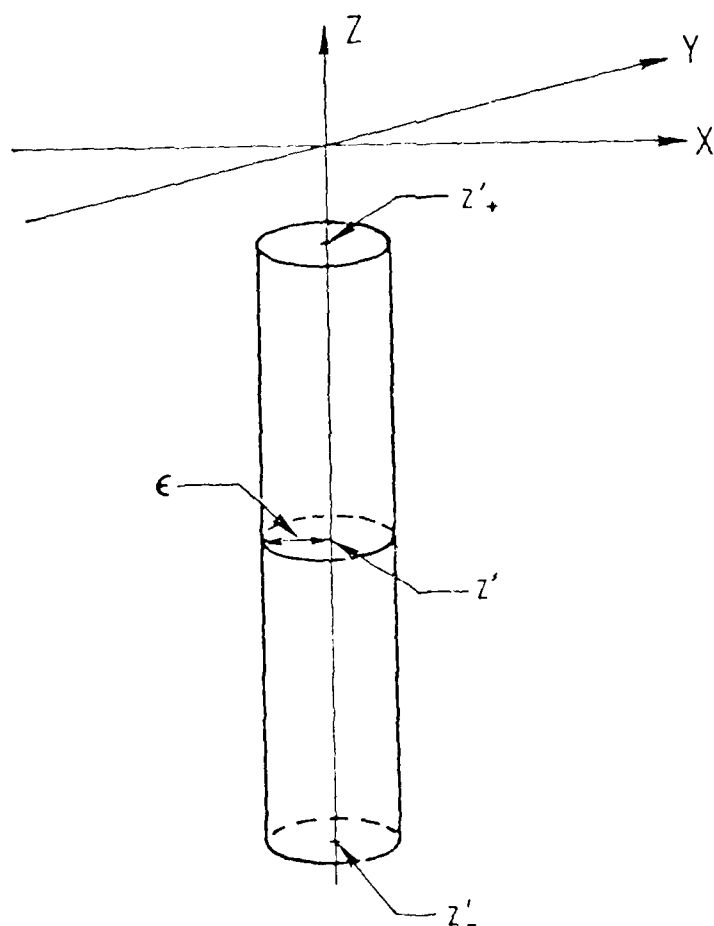


Fig. F-3. DBD. (a) Deflected beam far-field pattern factors. (b) Corresponding phase-vector or momentum matching diagram for exact satisfaction of Bragg condition.

AD-A097 899

AEROSPACE CORP EL SEGUNDO CA ELECTRONICS RESEARCH LAB F/G 20/5
PROGRESS TOWARD A MONOLITHICALLY INTEGRATED COHERENT DIODE LASE--ETC(U)
FEB 81 G A EVANS, E M GARMIRE, H M STOLL F04701-80-C-0081
TR-0081(6930-04)-2 SD-TR-81-7 NL

UNCLASSIFIED

3 OF 3
AD A
067889



END
DATE
FILMED
6-81
DTIC

or, expressing $\delta(z - z')$ in terms of the complete, orthonormal sets, $\epsilon_{o,v}(z)$ and $\mathcal{H}_{o,v}(z)$, that

$$2\pi\epsilon \left. \frac{\partial G_{TE}}{\partial R} \right|_{R=\epsilon} = \epsilon_o(z) \epsilon_o(z') + \int_v \epsilon_v(z) \epsilon_v(z') dv \quad (F-22)$$

for TE-polarized modes and

$$2\pi\epsilon \left. \frac{\partial G_{TM}}{\partial R} \right|_{R=\epsilon} + \frac{\mathcal{H}_o(z) \mathcal{H}_o(z')}{n_i^2} + \int_v \frac{\mathcal{H}_v(z) \mathcal{H}_v(z')}{n_i^2} dv \quad (F-23)$$

for TM-polarized modes.

Finally, integrating Eqs. (F-22) and (F-23) over R and imposing the necessary discontinuities on G_{TE} and G_{TM} as $\epsilon \rightarrow R \rightarrow 0$ yields G_{TE} and G_{TM} as given in Eqs. (F-24a) and (F-24b).

$$\begin{aligned} G_{TE}(\vec{r}|\vec{r}') &= \frac{1}{4} \left[H_o^{(2)} \left(k_{TE}^c R \right) \epsilon_o(z) \epsilon_o(z') \right. \\ &\quad \left. + \int_v H_o^{(2)} \left(k_{TE}^v R \right) \epsilon_v(z) \epsilon_v(z') dv \right] (\hat{a}_x \hat{a}_x + \hat{a}_y \hat{a}_y) \end{aligned} \quad (F-24a)$$

and

$$\begin{aligned} G_{TM}(\vec{r}|\vec{r}') &= \frac{1}{4} \left[H_o^{(2)} \left(k_{TM}^c R \right) \frac{\mathcal{H}_o(z) \mathcal{H}_o(z')}{n_j^2} \right. \\ &\quad \left. + \int_v H_o^{(2)} \left(k_{TM}^v R \right) \frac{\mathcal{H}_v(z) \mathcal{H}_v(z')}{n_j^2} dv \right] (\hat{a}_x \hat{a}_x + \hat{a}_y \hat{a}_y) \end{aligned} \quad (F-24b)$$

where $R = |\vec{r} - \vec{r}'|$, $H_0^{(2)}(x)$ is the zeroth order Hankel function of the second kind; $\epsilon_0(z)$ and $\mathcal{K}_0(z)$ are the lowest-order solutions of Eqs. (F-9a) and (F-9b) (we shall be concerned with guides that confine only the lowest order core-propagating modes); $\epsilon_v(z)$ and $\mathcal{K}_v(z)$ are the continuum mode solutions of Eqs. (F-9a) and (F-9b)¹⁸; k_{TE}^v and k_{TM}^v are the magnitudes of the corresponding continuum mode phase vectors; and $j = 1, 2, 3$. \underline{G}_{TE} and \underline{G}_{TM} (which lend themselves naturally to the interaction geometry of Fig. F-1 are, as noted, approximate in the sense that Bragg-scattered wave components reflected at the core-slab interface have been ignored. This approximation, which requires that $n_4 \approx n_2$ and, hence, that $\epsilon_0(z)$, $\epsilon_v(z)$, $\mathcal{K}_0(z)$, and $\mathcal{K}_v(z)$ retain essentially the same shape throughout the slab-coupled structure, remains valid for all but very shallow or very wide deflection angles.

Knowledge of the dyadic Green's functions \underline{G}_{TE} and \underline{G}_{TM} and of the driving terms \vec{Q}_{TE} and \vec{Q}_{TM} finally permits calculation of the various field quantities by evaluation of

$$\vec{E} = \vec{E}^C + \vec{E}^S = \iiint \underline{G}_{TE}(\vec{r}|\vec{r}') \vec{Q}_{TE}(\vec{E}^C + \vec{E}^S) dx' dy' dz' \quad (F-25a)$$

and

$$\vec{H} = \vec{H}^C + \vec{H}^S = \iiint \underline{G}_{TM}(\vec{r}|\vec{r}') \vec{Q}_{TM}(\vec{H}^C + \vec{H}^S) dx' dy' dz' \quad (F-25b)$$

Equations (F-25a) and (F-25b) are simplified considerably because the DBD perturbation induces coupling only between confined modes (core- and slab-propagating modes) and rescattering from the slab-propagating modes back to the core-propagating mode can be ignored. Accordingly, Eqs. (F-25a) and (F-25b) become

$$\vec{E}^S = \iiint \underline{G}_{TE}^P(\vec{r}|\vec{r}') \vec{Q}_{TE}(\vec{E}^C) dx' dy' dz' \quad (F-26a)$$

and

$$\vec{H}^s = \iiint \underline{G}_{TM}^P(\vec{r}|\vec{r}') \vec{Q}_{TM}(\vec{H}^c) dx' dy' dz' \quad (F-26b)$$

Where the only terms retained from the right-hand sides of Eqs. (F-25a) and (F-25b) have been those which contribute synchronously (or nearly synchronously) to the slab-propagating fields, \vec{E}^s and \vec{H}^s , and where \underline{G}_{TE}^P and \underline{G}_{TM}^P represent partial dyadic Green's functions obtained by dropping all but the first (confined mode) terms on the right-hand sides of Eqs. (F-24a) and (F-24b).

Evaluation of the right-hand sides of Eqs. (F-26a) and (F-26b) yields for the slab-propagating field distributions

$$\begin{aligned} \vec{E}^s = & \frac{1}{2k} \sqrt{\frac{\omega\mu_0}{\pi}} \exp + \left(i \frac{\pi}{4} - \alpha \frac{L}{2} \right) \left[\int_{-d}^0 \epsilon_0^2(z') dz' \right] \epsilon_0(z) \exp \left(\frac{-ik \cdot \vec{r}}{r} \right) f(\theta) \\ & \times [\hat{u}_r (A_x \cos \theta + A_y \sin \theta) + \hat{u}_\theta (-A_x \sin \theta + A_y \cos \theta)]; \quad j = 1, 2, 3 \end{aligned} \quad (F-27a)$$

and

$$\begin{aligned} \vec{H}^s = & \frac{1}{2k} \sqrt{\frac{\omega\epsilon_0}{\pi}} \exp \left(+ \frac{\pi}{4} - \alpha \frac{L}{2} \right) \left(\int_{-d}^0 \frac{o^2(z')}{n_j^2(z')} dz' \right) o(z) \frac{\exp(-ik \cdot \vec{r})}{\sqrt{r}} f(\theta) \\ & \times [\hat{u}_r (B_x \cos \theta + B_y \sin \theta) + \hat{u}_\theta (-B_x \sin \theta + B_y \cos \theta)]; \quad j = 1, 2, 3 \end{aligned} \quad (F-27b)$$

where \vec{E}^s and \vec{H}^s have been expressed in terms of the circular cylindrical coordinate system indicated in Fig. F-1 (\hat{u}_r and \hat{u}_θ are the radial and polar

unit vectors for this coordinate system); the large-argument, asymptotic form for $H_0^{(2)}(x)$ has been used

$$H_0^{(2)}(x) \sim \left(\frac{2}{\pi x}\right)^{1/2} \exp \frac{-i(x-\pi)}{4} \quad (\text{F-28})$$

the complex, core-propagating phase vector \tilde{k}^c has been taken to be $\tilde{k}^c = k - i\alpha$, and

$$f(\theta) = \iint W(y') \exp [-iu(\theta)y'] \exp [-\alpha x' - iv(\theta)x'] dx' dy' \quad (\text{F-29})$$

For clarity, all TE and TM subscripts have been omitted in Eqs. (F-27a) through (F-29) (the identities of all TE- and TM-related quantities are evident from context) and the angle-dependent factors, $u(\theta)$ and $v(\theta)$, which appear in Eq. (F-29), are given by

$$u(\theta) = (2\ell - 1) K_y - k \sin \theta \quad (\text{F-30})$$

and

$$v(\theta) = k (1 - \cos \theta) + (2\ell - 1) K_x \quad (\text{F-31})$$

where K_x and K_y are the Cartesian components of the DBD corrugation mechanical phase vector.

In order to calculate the core-propagating attenuation coefficients α_{TE} and α_{TM} of Eqs. (F-27a) and (F-27b), respectively, we now invoke the principle of power conservation among the incident and transmitted, core-propagating modes and the spectrum of Bragg-deflected slab-propagating modes. Specifically, we first integrate Poynting's vector for the deflected field distribution over a cylindrical surface whose axis of symmetry corresponds to that of the cylindrical coordinate system indicated in Fig. F-1 and whose radius is large compared with L , the length of the DBD. We then set the result of this integration equal to one watt (the assumed power content of the incident core-propagating mode) less the power transmitted down the core past

the DBD structure. The resultant equations yield explicit expressions for both α_{TE} and α_{TM} . Accordingly, the power conservation equation,

$$\frac{1}{2} \iint \operatorname{Re} [\vec{E} \times \vec{H}^*] \cdot d\vec{r} = 1 - \exp(-2\alpha L) \quad (F-32)$$

becomes, for the TE- and TM-polarized, deflected fields:

$$\frac{\Gamma_{TE}^2}{8\pi k_{TE}} \int [-A_x \sin \theta + A_y \cos \theta]^2 |f(\theta)|^2 d\theta = 1 - \exp(-2\alpha_{TE} L) \quad (F-33a)$$

and

$$\frac{\Gamma_{TM}^2}{8\pi k_{TM}} \int (-B_x \sin \theta + B_y \cos \theta)^2 |f(\theta)|^2 d\theta = 1 - \exp(-2\alpha_{TM} L) \quad (F-33b)$$

where

$$\begin{aligned} \Gamma_{TE} &\equiv \int_{-d}^0 \epsilon_o^2(z') dz' \\ \Gamma_{TM} &\equiv \int_{-d}^0 \frac{\epsilon_o^2(z')}{n_j^2} dz' \quad (j = 1, 2, 3) \\ |f(\theta)|^2 &= \frac{8w}{\pi^2} g_{x'}(\theta) g_{y'}(\theta) \end{aligned} \quad (F-34)$$

$$g_{x'}(\theta) = \frac{2 e^{-\alpha L}}{\alpha^2 + v^2(\theta)} \{ \cosh(\alpha L) - \cos[v(\theta) \cdot L] \} \quad (F-35)$$

and

$$g_{y'}(\theta) = \left\{ \frac{\cos[u(\theta) w/2]}{1 - [u(\theta) w/\pi]^2} \right\}^2 \quad (F-36)$$

As before the specific definition of α (i.e., either α_{TE} or α_{TM}) in Eqs. (F-32) and Eqs. (F-24) through (F-36), is understood from context.

The integrals on the left-hand sides of Eqs. (F-33a) and (F-33b) are easily evaluated once the relative variations with respect to θ of the integrand terms $g_x(\theta)$, $g_y(\theta)$, $(-A_x \sin \theta + A_y \cos \theta)^2$, and $(-B_x \sin \theta + B_y \cos \theta)^2$ have been examined. The full widths at half maxima of $g_x(\theta)$ and $g_y(\theta)$ (which are plotted in Fig. F-4 for the case of exact satisfaction of the Bragg condition) are given by

$$\Delta\theta_x \approx \frac{2\alpha}{k \varepsilon' n(\theta_B)} \quad (F-37)$$

and

$$\Delta\theta_y \approx \begin{cases} \left[\frac{2\pi}{w k \sin(\theta_B)} \right]^{1/2} : \theta_B \text{ near } \pi/2 \\ 2 \\ \frac{2\pi}{w k \cos(\theta_B)} : \text{otherwise} \end{cases} \quad (F-38)$$

where θ_B , the Bragg scattering angle, is recognized as being the deflection angle for which $u(\theta_B) = v(\theta_B) = 0$ and, hence, the angle for which g_x and g_y are simultaneously maxima (the latter conclusion requires that $k \gg \alpha$, a condition that will always be met for those geometries under consideration). From Eqs. (F-37) and (F-38), we now note that, for θ_B within the angular range of interest (i.e., $3\pi/4 > \theta_B > \pi/4$) and for weak deflectors (i.e., $k \gg \alpha$), both $(-A_x \sin \theta + A_y \cos \theta)^2$ and $(-B_x \sin \theta + B_y \cos \theta)^2$ vary slowly with respect to both $g_x(\theta)$ and $g_y(\theta)$ and can, as a consequence, be drawn outside the integrals of Eqs. (F-33a) and (F-33b). Similarly, for $\alpha^{-1} \gg w$, $\Delta\theta_x \ll \Delta\theta_y$ and $g_y(\theta_B)$ can be withdrawn from the integrals, leaving $g_x(\theta)$ as the only term that must be integrated in Eqs. (F-33a) and (F-33b) and the term which, because of its origin Eq. (F-32), determines the far-field pattern of the deflected wave.

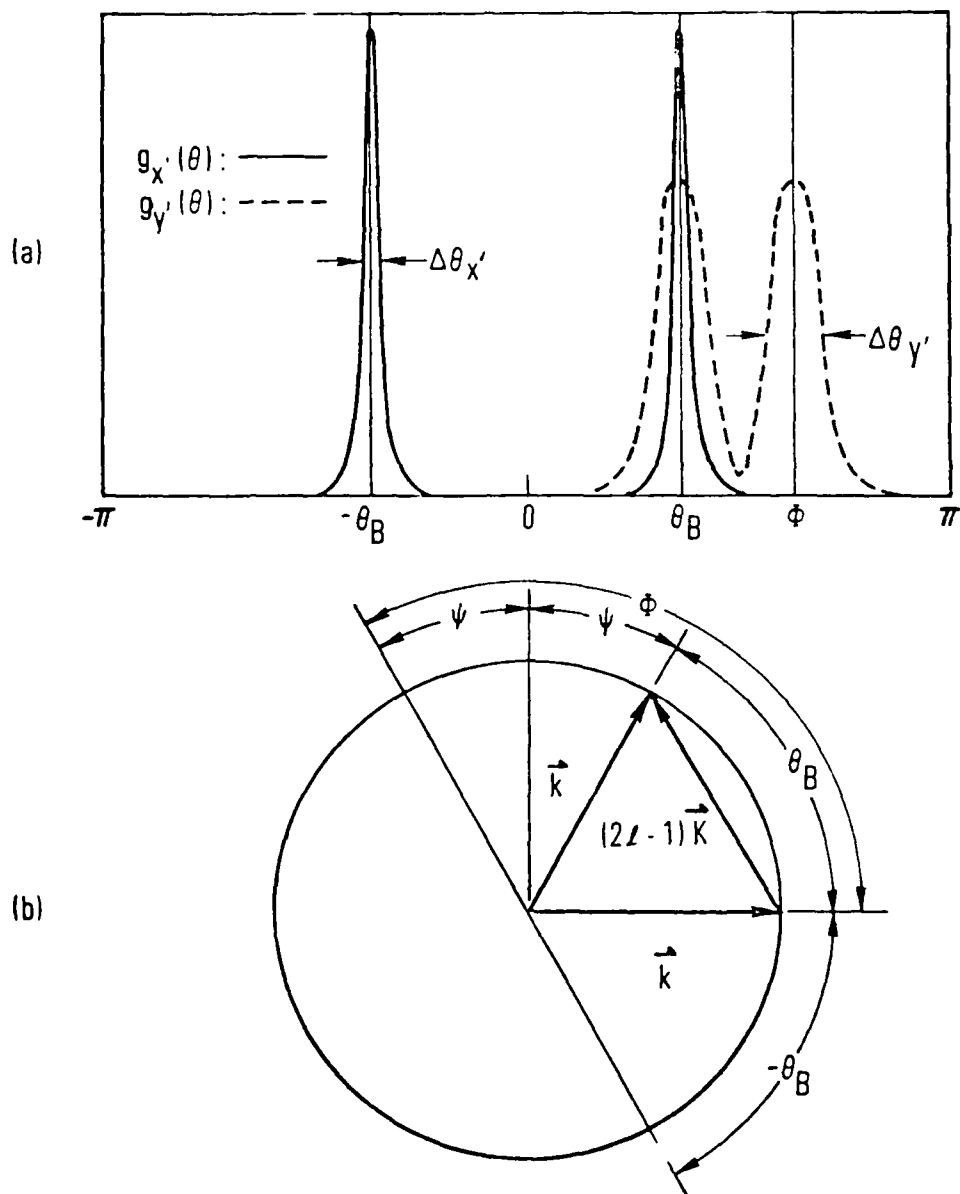


Fig. F-4. Normalized TE and TM Core-Propagating Attenuation Coefficients for Exact Satisfaction of Bragg Condition

Before performing the integrations in Eqs. (F-33a) and (F-33b) in order to obtain α_{TE} and α_{TM} , a comment should be made regarding the angular behavior of $g_{x-}(\theta)$ which, as noted earlier, determines the far-field radiation pattern of the DBD. Accordingly, note that $g_{x-}(\theta)$ [as well as $g_{y-}(\theta)$] is double valued over the angular range for which $2\pi > \theta > 0$ (Fig. A-3), reflecting the possibility that more than one deflected beam may emerge from the DBD. By referring to Eq. (F-36), this possibility is eliminated by requiring that

$$u(-\theta_B) \frac{w}{2} > \frac{3\pi}{2}$$

or that

$$w > \frac{3\pi}{2k \sin(\theta_B)} \quad (F-39)$$

The physical basis for Eq. (F-39) is the requirement that the DBD be made wide enough to permit the core-propagating mode to "sense" the transverse component of the perturbation phase vector K_y , and to prevent, thereby, energy from being deflected away from the structure at an angle $-\theta_B$. The condition in Eq. (F-39) together with the requirement that $w \ll \alpha^{-1}$, are seen to constrain w to lie within a well defined, but large and useful range. For example, $\theta_B = \pi/4$, $\alpha^{-1} = 1$ mm, and $k = 20 \mu\text{m}^{-1}$ (for $\sim 0.8 \mu\text{m}$ light propagating in a GaAs waveguide) requires that $1000 \mu\text{m} \gg w > 0.3 \mu\text{m}$.

With the use of the techniques and approximations discussed earlier and of the well-confined mode approximation,^{19,20} which implies that $k \approx n_2 k_0$ and that

$$\Gamma_{TE} \approx \Gamma_{TM} \approx \frac{2\pi^2}{3} \left(\frac{d}{t}\right)^3$$

Equations (F-33a) and (F-33b) finally yield for the TE and TM core-propagating attenuation coefficients

$$\alpha_{TE} = w \left[\frac{k_o (n_1^2 - n_2^2)}{\pi^2 (2\ell - 1) n_2} r_{TE} \right]^2 \cos^2 (\theta_B) \quad (F-40)$$

and

$$\alpha_{TM} = w \left[\frac{k_o n_1^2 - n_2^2}{\pi^2 (2\ell - 1) n_2} r_{TM} \right]^2 \times \left\{ - \frac{2n_2^2}{(n_1^2 - n_2^2)} \log \left(\frac{n_1}{n_2} \right) [\cos (\theta_B) - 1] - \cos (\theta_B) \right\}^2 \quad (F-41)$$

which, normalized by the factor

$$v = \frac{(2\ell - 1)^2}{w} \left(\frac{t}{d} \right)^6 \quad (F-42)$$

(where t and d are the waveguide thickness and perturbation groove depth, respectively) have been plotted in Fig. A-5 for a GaAlAs DBD with $n_1 = 1$, $n_2 = 3.6$, and $\lambda_o = 0.85 \mu\text{m}$. Equations (F-40) and (F-41) and, hence, the methods used in their derivations have been checked by allowing the DBD width to approach infinity and considering the limiting case of 180-deg deflection. Under these circumstances, $\Delta\theta_y \ll \Delta\theta_x$, $g_x(\pi)$ can be withdrawn from the integrals of Eqs. (F-33a) and (F-33b); and the resultant $\alpha_{TE} (\theta_B = \pi)$ and $\alpha_{TM} (\theta_B = \pi)$ reduce to the familiar contradirectional coupling coefficients of the DBR.²⁰

As discussed in Section F.2, knowledge of α_{TE} and α_{TM} permits calculation of the DBD deflection efficiencies, far-field deflected beam patterns and far-field beam widths. Accordingly, the DBD deflection efficiencies, for the TE- or TM-polarized waves, are given in a straightforward manner by

$$\eta_{TE, TM} = 1 - \exp (-2 L \alpha_{TE, TM}) \quad (F-43)$$

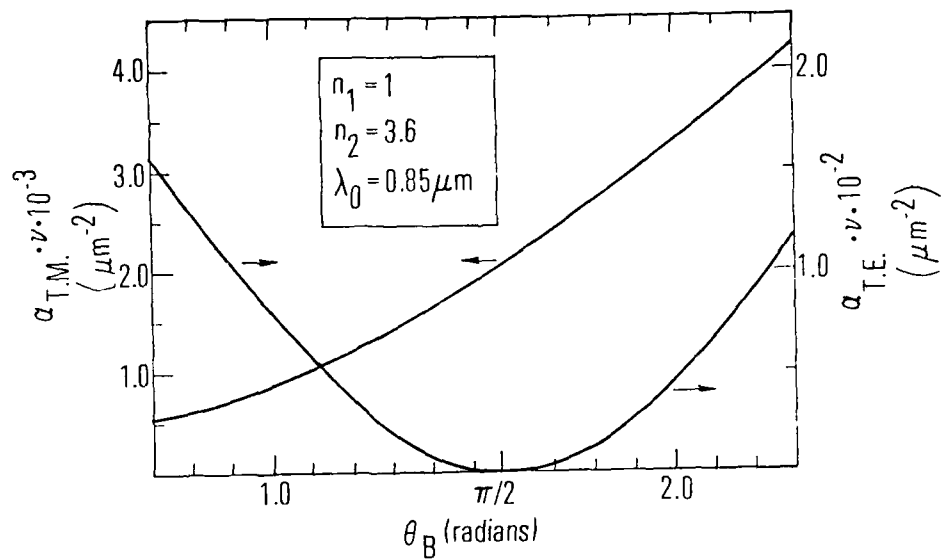


Fig. F-5. Plot of Factor by Which $\alpha_{TE, TM}$ Must Be Reduced When Bragg Condition is Not Satisfied.

Moreover, for $\alpha L \lesssim 2$ and, as discussed earlier, $\Delta\theta_{x'} \ll \Delta\theta_{y'}$, the TE- and TM-mode far-field patterns and far-field beam widths are given by $g_{x'}(\theta)$ and $\Delta\theta_{x'}$, respectively, or

$$I_{TE, TM} = g_{x'}(\theta) = \frac{1}{(\alpha_{TE, TM})^2 + v^2(\theta)} \quad (F-44)$$

and

$$\Delta\theta_{TE, TM} = \Delta\theta_{x'} = \frac{2\alpha_{TE, TM}}{2k \sin(\theta_B)} \quad (F-45)$$

where $I_{TE, TM}$ has a Lorentzian shape with a full-width at half maximum $\Delta\theta_{TE, TM}$ approximately equal to a wavelength within the guiding medium divided by the e-folding length of the DBD ($\sim 1/\alpha_{TE, TM}$). The latter observation is not surprising since the Fourier transform (Fraunhofer diffraction pattern) of a decaying exponential (the near-field pattern of the deflected wave must bear the same exponential dependence in the x-direction as the incident wave by conservation of power) is a Lorentzian.

We conclude by considering the effects on α of small departures from exact satisfaction of the Bragg condition. Specifically, given that

$$K = 2k \sin\left(\frac{\theta_B}{2}\right) \equiv 2k \cos(\phi) \quad (F-46)$$

for exact satisfaction of the Bragg condition, we consider the reductions in α_{TE} and α_{TM} that occur as a result of small errors in: (1) the magnitude of the DBD grating phase vector Δk , (2) the angular alignment of the DBD grating phase vector $\Delta\phi$, and (3) the magnitude of the core-propagating phase vector Δk . With it assumed, as before, that $\Delta\theta_{x'} \ll \Delta\theta_{y'}$, it is easily shown that the reduced attenuation coefficients α'_{TE} and α'_{TM} are given by

$$\alpha'_{TE, TM} \cong \alpha_{TE, TM} g_{y'}(u, w) \quad (F-47)$$

where

$$u \cong \left[(2\ell - 1) \frac{\sin (3\theta_B/2)}{\sin (\theta_B)} \right] \Delta K - k \Delta \phi + \left[\frac{\cos (\theta_B) - 1}{\sin (\theta_B)} \right] \Delta k \quad (F-48)$$

The reduction factor, $g_y(u, w)$, which equals one when condition (F-46) is satisfied, is plotted in Fig. F-6.

F.4 DEVICE APPLICATIONS

The operational characteristics of the basic DBD structure suggest that a number of active and passive integrated optical device applications are possible. Passive applications include intrawaveguide beam expansion, division, deflection, and, for 90-deg deflection, polarization analysis. Possible active applications include modulation and wide-angle, intrawaveguide beam steering.

Used as a lens-less intrawaveguide beam expander-collimator, the DBD appears particularly well suited for reducing the beam divergence of fully integrated DFB or DBR lasing sources (wherein the expansion-collimation would take place in a passive waveguiding region lying adjacent to the active, lasing region).²¹ Integrated optical device applications of such a laser-DBD configuration might include real-time spectrum analyzers,²² which require high-resolution acousto-optic beam scanning and high-radiance (or low beam divergence) semiconductor laser sources. As an example, taking the case of a GaAlAs DBD for which $n_1 = 1$, $n_2 = 3.6$, $\lambda_o = 0.85 \mu\text{m}$, $\theta_B = \pi/2$, $\ell = 1$ ($\Lambda = 0.167 \mu\text{m}$), $w = 10 \mu\text{m}$, $t = 2.0 \mu\text{m}$, $d = 0.136 \mu\text{m}$, $L = 2 \text{ mm}$, and assuming the well-confined mode approximation is valid, Fig. F-4 and Eqs. (F-43) and (F-45) yield a deflected wave beam width of $\Delta\theta_x = 1.5 \times 10^{-4} \text{ rad}$ or an intrawaveguide beam expansion factor of $M = 157$, where M is defined by

$$M \equiv \frac{(\lambda_o/n_2 w)}{\Delta\theta_x} \quad (F-49)$$

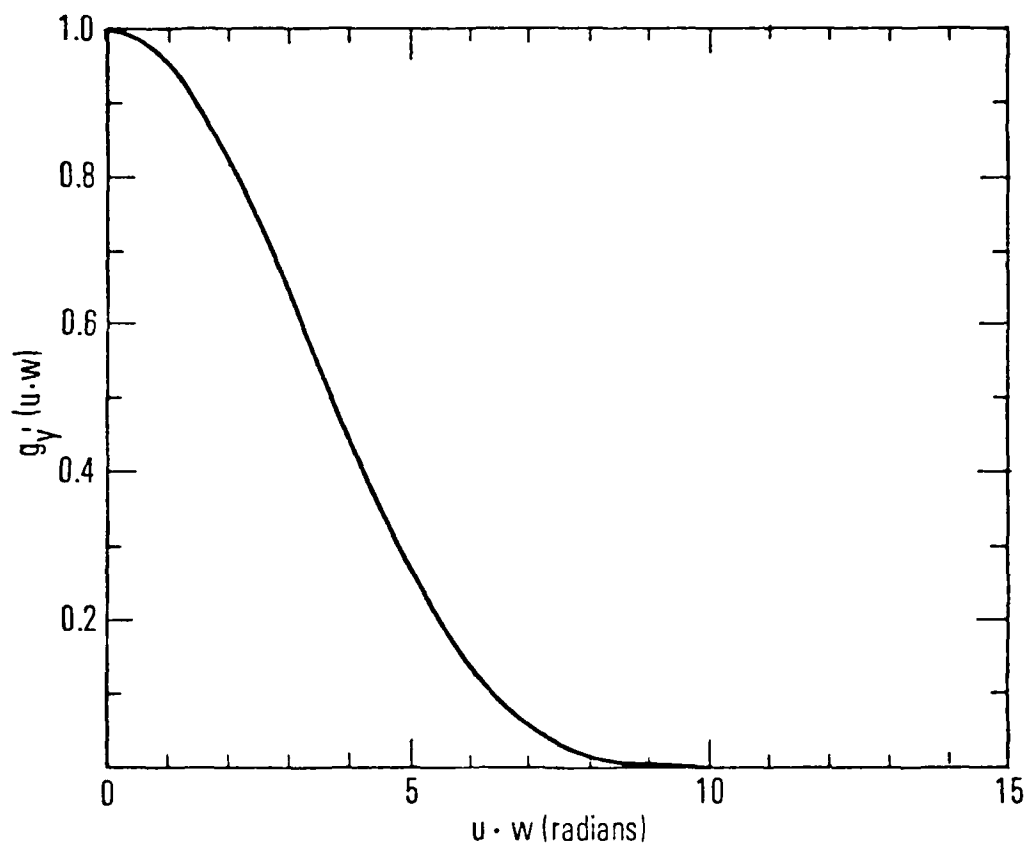


Fig. F-6. Cylindrical Volume Over Which Eq. (F-3) is Integrated to Determine Form of G

As an efficient intrawaveguide polarizer-analyzer, the DBD's potential utility is immediately suggested by the plots of $\alpha_{TE}(\theta_B)$ and $\alpha_{TM}(\theta_B)$ shown in Fig. F-4. Operation of a DBD near $\theta_B = \pi/2$ rad ensures both good polarization discrimination (α_{TE} is roughly a factor of 5 smaller than α_{TM} near $\theta_B = \pi/2$ and, indeed, equals zero for $\theta_B = \pi/2$) and considerable insensitivity to small errors in θ_B (α_{TE} goes through a broad null near $\theta_B = \pi/2$). The DBD may be used as a simple intrawaveguide beam deflector or beam divider. For example, with $L = 0.2$ mm and all other device parameters as before (for the beam expander) yields a TM deflection or beam division efficiency of $\eta_{TM} = 0.55$.

With regard to use of the DBD as a modulator, Fig. F-6 and Eqs. (F-47) and (F-48) indicate that (with modulation assumed to be accomplished through an external manipulation of either α'_{TE} or α'_{TM}) only relatively large changes in ΔK and $\Delta\phi$ are effective. From this observation, it is implied that a DBD modulator based upon electronically alterable magnetic stripe domains,⁸ as an example, is feasible whereas one that relies upon a relatively small electro-optic variation in Δk is not. Similar reasoning, of course, applies to the case of wide-angle, intrawaveguide beam scanners that require large simultaneous changes in both ΔK and $\Delta\phi$.

F.5 CONCLUSIONS

A Green's function technique has been used to find the deflection efficiencies and far-field deflected-beam patterns of an integrated optical wide-angle deflection device, a distributed Bragg deflector (DBD). Intrawaveguide interactions involving deflection angles between $\pi/4$ and $3\pi/4$ rad and both TE- and TM-polarized waves have been considered.

Because of the gradual or distributed nature of the Bragg deflection process for those geometries of interest, the DBD may be employed as an efficient compact intrawaveguide beam expander. Moreover, because of its polarization-dependent deflection efficiencies, the 90-deg DBD is promising as a simple integrated optical polarizer-analyzer. Other potential passive integrated optical embodiments of the basic DBD structure include intrawaveguide beam deflectors and beam splitters. With regard to active device applications, the relative insensitivity of the DBD's deflection efficiency to small

changes in phase vector magnitude appears to preclude use of the DBD as an electro-optic Bragg modulator. Integrated-optical modulators and intrawaveguide beam scanners based upon an external manipulation of either the magnitude or the orientation of the DBD k -vector do, however, appear feasible.

APPENDIX F REFERENCES

1. J. M. Hammer, Appl. Phys. Lett. 18, 147 (1971).
2. J. N. Polky and J. H. Harris, Appl. Phys. Lett. 21, 307 (1972).
3. J. M. Hammer, D. J. Channin, and M. T. Duffy, Appl. Phys. Lett. 23, 176 (1973).
4. L. Kuhn, M. L. Dakss, P. F. Heidrich, and B. A. Scott, Appl. Phys. Lett. 17, 265 (1970).
5. C. M. Verber, V. E. Wood, R. P. Kenan, and N. F. Hartman, Ferroelectrics 10, 253 (1976).
6. O. Mikami, Opt. Commun. 19, 42 (1976).
7. R. P. Kenan, D. W. Vahey, N. F. Hartman, V. E. Wood, and C. M. Verber, Opt. Engr. 15, 12 (1976).
8. G. F. Sauter, M. M. Hanson, and D. L. Fleming, Appl. Phys. Lett. 30, 11 (1977).
9. E. A. J. Marcatili, Bell Syst. Tech. J. 53, 645 (1973).
10. J. E. Goell, J. Appl. Opt. 12, 2797 (1973).
11. H. Furuta, H. Noda, and A. Ihaya, Appl. Opt. 13, 322 (1974).
12. E. A. J. Marcatili, Bell Syst. Tech. J. 53, 650 (1973).
13. H. Kogelnik, Bell Syst. Tech. J. 48, 2909 (1969).
14. R. P. Kenan, J. Appl. Phys. 46, 4545 (1975).
15. T. G. Giallorenzi, J. Appl. Phys. 44, 242 (1973).
16. E. A. J. Marcatili, Bell Syst. Tech. J. 48, 2071 (1969).
17. H. F. Taylor and A. Yariv, Proc. IEEE 62, 1044 (1974).
18. D. Marcuse, Light Transmission Optics, Van Nostrand Reinhold Company, 1972.
19. A. Yariv, IEEE J. Quantum Electron. QE-9, 919 (1973).

20. H. Stoll and A. Yariv, Opt. Commun. 8, 5 (1973).
21. S. Wang, IEEE J. Quantum Electron. QE-13, 176 (1977).
22. D. B. Anderson, J. T. Boyd, M. C. Hamilton, and R. R. August, IEEE J. Quantum Electron. QE-13, 268 (1977).

LABORATORY OPERATIONS

The Laboratory Operations of The Aerospace Corporation is conducting experimental and theoretical investigations necessary for the evaluation and application of scientific advances to new military concepts and systems. Versatility and flexibility have been developed to a high degree by the laboratory personnel in dealing with the many problems encountered in the Nation's rapidly developing space systems. Expertise in the latest scientific developments is vital to the accomplishment of tasks related to these problems. The laboratories that contribute to this research are:

Aerophysics Laboratory: Aerodynamics; fluid dynamics; plasmadynamics; chemical kinetics; engineering mechanics; flight dynamics; heat transfer; high-power gas lasers, continuous and pulsed, IR, visible, UV; laser physics, laser resonator optics; laser effects and countermeasures.

Chemistry and Physics Laboratory: Atmospheric reactions and optical backgrounds; radiative transfer and atmospheric transmission; thermal and state-specific reaction rates in rocket plumes; chemical thermodynamics and propulsion chemistry; laser isotope separation; chemistry and physics of particles; space environmental and contamination effects on spacecraft materials; lubrication; surface chemistry of insulators and conductors; cathode materials; sensor materials and sensor optics; applied laser spectroscopy; atomic frequency standards; pollution and toxic materials monitoring.

Electronics Research Laboratory: Electromagnetic theory and propagation phenomena; microwave and semiconductor devices and integrated circuits; quantum electronics, lasers, and electro-optics; communication sciences, applied electronics, superconducting and electronic device physics; millimeter-wave and far-infrared technology.

Materials Sciences Laboratory: Development of new materials; composite materials; graphite and ceramics; polymeric materials; weapons effects and hardened materials; materials for electronic devices; dimensionally stable materials; chemical and structural analyses; stress corrosion; fatigue of metals.

Space Sciences Laboratory: Atmospheric and ionospheric physics, radiation from the atmosphere, density and composition of the atmosphere, aurorae and airglow; magnetospheric physics, cosmic rays, generation and propagation of plasma waves in the magnetosphere; solar physics, x-ray astronomy; the effects of nuclear explosions, magnetic storms, and solar activity on the earth's atmosphere, ionosphere, and magnetosphere; the effects of optical, electromagnetic, and particulate radiations in space on space systems.

DATE
FILMED
-8